

Higgs Boson Precision Analysis of the Full LHC Run 1 and Run 2 Data

Yongtae Heo,^{1,2a} Dong-Won Jung,^{1,3,4b} and Jae Sik Lee^{1,2c}

¹ *Department of Physics, Chonnam National University, Gwangju 61186, Korea*

² *IUEP, Chonnam National University, Gwangju 61186, Korea*

³ *Department of Physics, Yonsei University, Seoul 03722, Korea*

⁴ *Cosmology, Gravity, and Astroparticle Physics Group,*

Center for Theoretical Physics of the Universe, Institute for Basic Science, Daejeon 34126, Korea

(Dated: May 31, 2024)

We perform global fits of the Higgs boson couplings to the full Higgs datasets collected at the LHC with the integrated luminosities per experiment of approximately 5/fb at 7 TeV, 20/fb at 8 TeV, and up to 139/fb at 13 TeV. Our combined analysis based on the experimental signal strengths used in this work and the theoretical ones elaborated for our analysis reliably reproduce the results in the literature. We reveal that the LHC Higgs precision data are no longer best described by the SM Higgs boson taking account of extensive and comprehensive CP-conserving and CP-violating scenarios found in several well-motivated models beyond the SM. Especially, in most of the fits considered in this work, we observe that the best-fitted values of the normalized Yukawa couplings are about 2σ below the corresponding SM ones with the 1σ errors of 3%-5%. On the other hand, the gauge-Higgs couplings are consistent with the SM with the 1σ errors of 2%-3%. Incidentally, the reduced Yukawa couplings help to explain the excess of the $H \rightarrow Z\gamma$ signal strength of 2.2 ± 0.7 recently reported by the ATLAS and CMS collaborations.

arXiv:2402.02822v3 [hep-ph] 16 Jul 2024

^a yongtae1heo@gmail.com

^b dongwon.jung@ibs.re.kr

^c jslee@jnu.ac.kr

I. INTRODUCTION

Since the ATLAS and CMS collaborations have independently reported the observation of a new scalar particle in the search for the Standard Model (SM) Higgs boson in 2012 [1, 2],¹ more than 30 times larger number of Higgs bosons have been recorded by the both collaborations at the CERN Large Hadron Collider (LHC). Recently, ten years after the discovery, the two collaborations have presented the two legacy papers portraying the Higgs boson and revealing a detailed map of its interactions based on the precision Higgs data collected during the Run 2 data-taking period between 2015 and 2018 [3, 4]. During the Run 2 period at a center-of-mass energy of 13 TeV, the ATLAS and CMS collaborations have accumulated the integrated luminosities of 139/fb and 138/fb, respectively, which exceed those accumulated during the full Run 1 period by the factor of more than 5.²

Though there was a quite room for the new scalar boson weighing 125 GeV³ to be different from the SM Higgs boson around the discovery stage [6] but the increasing Higgs datasets soon revealed that they were best described by the SM Higgs boson [7]. Around the end of the Run 2 period before the Run 2 Higgs data are fully analyzed, the five productions modes of gluon-gluon fusion (ggF), vector-boson fusion (VBF), the associated production with a $V = W/Z$ boson (WH/ZH), and the associated production with a top-quark pair (ttH) had been extensively investigated and, impressively, the Higgs decays into a pair of b quarks [8, 9] and a pair of τ leptons [10, 11] were observed in single measurements leading to the firm establishment of third-generation Yukawa couplings together with the top-quark Yukawa coupling constrained by the ggF and ttH productions and the Higgs decay to two photons [12]. Now, with the Run 2 Higgs data fully analyzed [3, 4], the sixth Higgs production process associated with a single top quark (tH) starts to be involved and the Higgs boson decays into a pair of muons and $Z\gamma$ are emerging. The *direct* searches for so-called invisible Higgs boson decays into non-SM particles have been also carried out.

In Refs. [3, 4], the ATLAS and CMS collaborations scrutinize the interactions of the 125 GeV Higgs boson using the Higgs precision data recorded by their own experiments during the Run 2 period and independently yield the following Run 2 global signal strengths assuming that all the production and decay processes scale with the overall single signal strength:

$$\mu_{\text{Run 2 ATLAS}}^{\text{Global}} = 1.05 \pm 0.06 ; \quad \mu_{\text{Run 2 CMS}}^{\text{Global}} = 1.002 \pm 0.057, \quad (1)$$

in remarkable agreement with the SM expectation. In this work, by combining the ATLAS and CMS Run 2 data on the signal strengths as well as including, though statistically less important, the Run 1 LHC [13] and Tevatron global signal strengths,⁴ we find the following global signal strength:

$$\mu_{76 \text{ signal strengths}}^{\text{Global}} = 1.012 \pm 0.034. \quad (2)$$

Upon the previous model-independent analyses [6, 7, 12], we have improved our analysis by including the tH production process to accommodate the LHC Run 2 data and by treating the ggF production signal strength beyond leading order in QCD to match the precision of the ever-increasing Higgs data now and after.

We demonstrate that our combined analysis based on the experimental signal strengths used in this work and the theoretical ones elaborated for our analysis reliably reproduce the fitting results presented in Ref. [13] (Run 1) and Refs. [3, 4] (Run 2) within 0.5 standard deviations. Our extensive and comprehensive CP-conserving and CP-violating fits taking account of various scenarios found in several well-motivated models beyond the SM (BSM) reveal that the LHC Higgs precision data are no longer best described by the SM Higgs boson. Especially, in most of the fits, we observe that the best-fitted values of the Yukawa couplings are about 2σ below the corresponding SM ones with the 1σ errors of 3-5%. The reduced Yukawa couplings help to explain the combined $H \rightarrow Z\gamma$ signal strength of 2.2 ± 0.7 recently reported by the ATLAS and CMS collaborations [14]. Accordingly, the SM points locate outside the 68% confidence level (CL) region mostly and even the 95% CL region sometimes in many of the two-parameter planes involved Yukawa couplings. We further note that the BSM models predicting the same scaling behavior of the Yukawa couplings to the up- and down-type quarks and charged leptons are preferred. On the other hand, the gauge-Higgs couplings are consistent with the SM with the 1σ errors of 2%-3%. Incidentally, we note that CP violation is largely unconstrained by the LHC Higgs data with the CL regions appearing as a circle or an ellipse or some overlapping of them in the CP-violating two-parameter planes.

This paper is organized as follows. Section II is devoted to reviewing the ATLAS and CMS Run 2 data on the signal strengths as well as the Run 1 LHC and Tevatron ones used in this work. We compare our results on the global signal strengths and the signal strengths for the individual Higgs production processes and decay modes with those in

¹ The ATLAS discovery was based on approximately 4.8/fb collected at $\sqrt{s} = 7$ TeV and 5.8/fb at $\sqrt{s} = 8$ TeV while the CMS discovery on up to 5.1/fb at 7 TeV and 5.3/fb at 8 TeV.

² During the full Run 1 period, each of the collaborations accumulated approximately 5/fb at 7 TeV and 20/fb at 8 TeV.

³ Recently, exploiting the decay channels of $H \rightarrow ZZ^* \rightarrow 4\ell$ and $H \rightarrow \gamma\gamma$, the ATLAS collaboration reports the result of a Higgs mass measurement of 125.11 ± 0.11 GeV with a 0.09% precision which is based on 140/fb at 13 TeV combined with the Run 1 measurement, see Ref. [5].

⁴ See Tables I,II, III, and IV.

TABLE I. (**Tevatron: 1.96 TeV**) *The signal strengths data from Tevatron (10.0/fb at 1.96 TeV).*

Channel	Signal strength	M_H (GeV)	Production mode		
			ggF	VBF	WH \oplus ZH
Combined $H \rightarrow \gamma\gamma$ [15]	$6.14^{+3.25}_{-3.19}$	125	78%	5%	17%
Combined $H \rightarrow WW^{(*)}$ [15]	$0.85^{+0.88}_{-0.81}$	125	78%	5%	17%
VH-tagged $H \rightarrow bb$ [16]	$1.59^{+0.69}_{-0.72}$	125	–	–	100%

TABLE II. (**LHC: 7 \oplus 8 TeV**) *Combined ATLAS and CMS Run 1 data on signal strengths [13] used in this work (Approximately 5/fb at 7 TeV and 20/fb at 8 TeV per experiment). $M_H = 125.09$ GeV is taken.*

Production mode	Decay mode				
	$\gamma\gamma$	ZZ^*	WW^*	bb	$\tau\tau$
ggF	$1.10^{+0.23}_{-0.22}$	$1.13^{+0.34}_{-0.31}$	$0.84^{+0.17}_{-0.17}$	–	$1.0^{+0.6}_{-0.6}$
VBF	$1.3^{+0.5}_{-0.5}$	$0.1^{+1.1}_{-0.6}$	$1.2^{+0.4}_{-0.4}$	–	$1.3^{+0.4}_{-0.4}$
WH	$0.5^{+1.3}_{-1.2}$	–	$1.6^{+1.2}_{-1.0}$	$1.0^{+0.5}_{-0.5}$	$-1.4^{+1.4}_{-1.4}$
ZH	$0.5^{+3.0}_{-2.5}$	–	$5.9^{+2.6}_{-2.2}$	$0.4^{+0.4}_{-0.4}$	$2.2^{+2.2}_{-1.8}$
ttH	$2.2^{+1.6}_{-1.3}$	–	$5.0^{+1.8}_{-1.7}$	$1.1^{+1.0}_{-1.0}$	$-1.9^{+3.7}_{-3.3}$

Refs. [3, 4, 13]. In Section III, we fix the conventions and notations of the model-independent couplings of the 125 GeV Higgs-boson H to the SM particles assuming that H is a CP-mixed scalar. And we elaborate on the parametric dependence of the theoretical signal strengths for the relevant Higgs production processes and decay modes. In Section IV, we perform global fits of the Higgs boson couplings to the full Higgs datasets collected at the LHC and Tevatron considering various CP-conserving and CP-violating scenarios extensively. Conclusions are made in Section V. In Appendix A, we provide the details of how we work out the ggF production signal strength beyond leading order in QCD. Appendix B is devoted to the chi-square behavior when only a single fitting parameter is varied while all the other ones are fixed at their SM values of either 0 or 1. In Appendix C, we figure out the dependence of the $H \rightarrow \gamma\gamma$ signal strength on the gauge-Higgs and Yukawa couplings in the two-parameter fit frequently referred in the literature. We present correlations among the fitting parameters in some CP-conserving fits in Appendix D. Finally, for global fits including the $H \rightarrow Z\gamma$ data recently reported, see Appendix E.

II. HIGGS SIGNAL STRENGTH: DATA AND OVERALL RESULTS

For our global fits, we use all the available *direct* Higgs data collected at the Tevatron and the LHC. We use 3 signal strengths measured at the Tevatron [15, 16] as shown in Table I. For the Run 1 LHC data at center-of-mass energies of $\sqrt{s} = 7$ and 8 TeV, abbreviated as 7 \oplus 8 TeV for the later use, we use 20 signal strengths and the correlation matrix obtained in the combined ATLAS and CMS analysis [13], see Table II.⁵

The Run 2 data on signal strengths are given separately by the ATLAS and CMS collaborations. The ATLAS input for the Run 2 data on signal strengths includes the latest results from the Higgs decays into $ZZ \rightarrow 4\ell$ [17], $W^\pm W^\mp \rightarrow \ell\nu\ell\nu$ [18, 19], $\gamma\gamma$ [20], $Z\gamma \rightarrow \ell^+\ell^-\gamma$ [21], $b\bar{b}$ [22–26], $\tau^+\tau^-$ [27], multiple leptons ($\tau^+\tau^-$, $W^\pm W^\mp$, ZZ) [28], $\mu^+\mu^-$ [29], $c\bar{c}$ [30], and invisible particles [31, 32]. For our analysis, dropping the results from the Higgs decays into $Z\gamma$, $c\bar{c}$, and invisible particles which have not been evidenced at the current stage giving constraints rather than measurements, we use 25 signal strengths shown in Table III and the correlation matrix of the production cross sections times branching fractions.⁶ On the other hand, the CMS input for the Run 2 data on signal strengths includes the decay channels into

⁵ Specifically, see Table 8 of Ref. [13] for the combined signal strengths and Fig. 27 therein for the correlation matrix. The more detailed information could be found in the website <https://doi.org/10.17182/hepdata.78403>.

⁶ For the ATLAS Run 2 signal strengths, see Fig. 3 in Ref. [3] together with detailed information on them provided in the website <https://doi.org/10.17182/hepdata.130266>. For the correlation matrix, see Auxiliary Fig. 14 presented in the website.

TABLE III. (LHC: 13 TeV) ATLAS Run 2 data on signal strengths [3] used in this work (139/fb at 13 TeV). We refer to the website <https://doi.org/10.17182/hepdata.130266> for specific information. $M_H = 125.09$ GeV is taken.

Production mode	Decay mode					
	$\gamma\gamma$	ZZ^*	WW^*	bb	$\tau\tau$	$\mu\mu$
ggF+bbH	$1.04^{+0.10}_{-0.10}$	$0.95^{+0.11}_{-0.10}$	$1.14^{+0.13}_{-0.13}$	—	$0.90^{+0.29}_{-0.26}$	—
VBF	$1.36^{+0.30}_{-0.26}$	$1.33^{+0.52}_{-0.43}$	$1.13^{+0.19}_{-0.18}$	—	$1.00^{+0.21}_{-0.18}$	—
WH	$1.53^{+0.56}_{-0.51}$	—	$2.26^{+1.21}_{-1.02}$	$1.06^{+0.28}_{-0.26}$	—	—
ZH	$-0.22^{+0.61}_{-0.54}$	—	$2.86^{+1.84}_{-1.33}$	$1.00^{+0.25}_{-0.23}$	—	—
ttH	$0.90^{+0.33}_{-0.31}$	—	—	—	—	—
tH	$2.61^{+4.23}_{-3.38}$	—	—	—	—	—
ggF+bbH \oplus VBF	—	—	—	$0.98^{+0.38}_{-0.36}$	—	—
WH \oplus ZH	—	$1.50^{+1.17}_{-0.94}$	—	—	$1.00^{+0.62}_{-0.59}$	—
ttH \oplus tH	—	$1.68^{+1.68}_{-1.11}$	$1.64^{+0.65}_{-0.61}$	$0.35^{+0.34}_{-0.33}$	$1.37^{+0.86}_{-0.75}$	—
ggF+bbH \oplus ttH \oplus tH	—	—	—	—	—	$0.54^{+0.89}_{-0.88}$
VBF \oplus WH \oplus ZH	—	—	—	—	—	$2.31^{+1.33}_{-1.26}$

TABLE IV. (LHC: 13 TeV) CMS Run 2 data on signal strengths [4] used in this work (138/fb at 13 TeV). $M_H = 125.38$ GeV is taken.

Production mode	Decay mode					
	$\gamma\gamma$	ZZ^*	WW^*	bb	$\tau\tau$	$\mu\mu$
ggF+bbH	$1.08^{+0.12}_{-0.11}$	$0.93^{+0.14}_{-0.13}$	$0.90^{+0.11}_{-0.10}$	$5.31^{+2.97}_{-2.54}$	$0.66^{+0.21}_{-0.21}$	$0.33^{+0.74}_{-0.70}$
VBF	$1.00^{+0.35}_{-0.32}$	$0.32^{+0.48}_{-0.32}$	$0.73^{+0.28}_{-0.24}$	—	$0.86^{+0.17}_{-0.16}$	$1.55^{+0.86}_{-0.73}$
WH	$1.43^{+0.54}_{-0.47}$	$0.00^{+1.55}$	$2.41^{+0.72}_{-0.70}$	$1.26^{+0.42}_{-0.41}$	$1.33^{+0.61}_{-0.57}$	—
ZH	$1.19^{+0.71}_{-0.62}$	$12.24^{+6.59}_{-5.69}$	$1.76^{+0.75}_{-0.67}$	$0.90^{+0.36}_{-0.34}$	$1.89^{+0.65}_{-0.56}$	—
WH \oplus ZH	—	—	—	—	—	$5.63^{+3.04}_{-3.36}$
ttH \oplus tH	$1.38^{+0.34}_{-0.29}$	$0.00^{+0.73}$	$1.44^{+0.32}_{-0.32}$	$0.90^{+0.46}_{-0.44}$	$0.35^{+0.44}_{-0.37}$	$3.07^{+2.63}_{-2.21}$

$\gamma\gamma$ [33], $ZZ \rightarrow 4\ell$ [34], $W^\pm W^\mp \rightarrow \ell\nu\ell\nu$ [35], $Z\gamma$ [36], $\tau^+\tau^-$ [37], $b\bar{b}$ [9, 38–41], $\mu^+\mu^-$ [42], multileptons with ttH/tH [43], and invisible particles [44–46]. Dropping the Higgs decays into $Z\gamma$ and invisible particles as in the ATLAS case, we use 28 signal strengths shown in Table IV and the correlation matrix. ⁷ For the Higgs production, commonly investigated are the six processes of gluon-gluon fusion (ggF), vector-boson fusion (VBF), the associated production with a $V = W/Z$ boson (WH/ZH), the associated production with a top-quark pair (ttH), and the associated production with a single top quark (tH).

We compare the ATLAS+CMS combined Run 1 data on signal strengths with the either ATLAS or CMS Run 2 data on signal strengths for various combinations of Higgs boson production and decay processes, see Table II and Tables III and IV. We note that the tH production process and the $H \rightarrow \mu\mu$ decay mode have been newly measured and the mixed-production modes such as ggF+bbH \oplus VBF, WH \oplus ZH, ttH \oplus tH, ggF+bbH \oplus ttH \oplus tH, and VBF \oplus WH \oplus ZH are involved especially when the Higgs boson decays into a pair of fermions. ⁸ Incidentally, in Run 2, the Higgs decay into ZZ^* is measured also in the WH, ZH, and ttH production modes though the corresponding errors are still large. Further we observe that the ttH and tH production processes have been always combined except in the ATLAS measurement of the

⁷ For the CMS Run 2 signal strengths, see Fig. B.6 in Ref. [4]. For the correlation matrix, see the figure entitled “Production times decay signal strength modifiers correlations” provided in the website <https://dx.doi.org/10.17182/hepdata.127765>.

⁸ We expect that the mixed-production modes might be resolved into individual ones in the next Run(s) with the higher luminosities.

TABLE V. *LHC signal strengths for individual Higgs production processes and decay modes. For the combined Run 1 signal strengths, see Tables 12 and 13 in Ref. [13]. For the ATLAS Run 2 signal strengths, see Fig. 2 in Ref. [3] together with detailed information on them provided in the website <https://doi.org/10.17182/hepdata.130266>. The CMS Run 2 signal strengths are from Fig. 2 in Ref. [4]. Note that the production signal strengths have been obtained assuming that the Higgs boson branching fractions are the same as in the SM and the decay signal strengths have been extracted assuming that the Higgs boson production cross sections are the same as in the SM.*

LHC	Production process						Decay mode					
	ggF(\oplus bbH)	VBF	WH	ZH	ttH	tH	$\gamma\gamma$	ZZ^*	WW^*	bb	$\tau\tau$	$\mu\mu$
Run 1 [13]	$1.03^{+0.16}_{-0.14}$	$1.18^{+0.25}_{-0.23}$	$0.89^{+0.40}_{-0.38}$	$0.79^{+0.38}_{-0.36}$	$2.3^{+0.7}_{-0.6}$	—	$1.14^{+0.19}_{-0.18}$	$1.29^{+0.26}_{-0.23}$	$1.09^{+0.18}_{-0.16}$	$0.70^{+0.29}_{-0.27}$	$1.11^{+0.24}_{-0.22}$	—
Run 2 ATLAS [3]	$1.03^{+0.07}_{-0.07}$	$1.10^{+0.13}_{-0.12}$	$1.16^{+0.23}_{-0.22}$	$0.96^{+0.22}_{-0.21}$	$0.74^{+0.24}_{-0.24}$	$6.61^{+4.24}_{-3.76}$	$1.09^{+0.10}_{-0.09}$	$1.04^{+0.11}_{-0.10}$	$1.20^{+0.12}_{-0.11}$	$0.91^{+0.15}_{-0.14}$	$0.96^{+0.12}_{-0.11}$	$1.21^{+0.62}_{-0.60}$
Run 2 CMS [4]	$0.97^{+0.08}_{-0.08}$	$0.80^{+0.12}_{-0.12}$	$1.49^{+0.26}_{-0.25}$	$1.29^{+0.24}_{-0.23}$	$1.13^{+0.18}_{-0.17}$		$1.13^{+0.09}_{-0.09}$	$0.97^{+0.12}_{-0.11}$	$0.97^{+0.09}_{-0.09}$	$1.05^{+0.22}_{-0.21}$	$0.85^{+0.10}_{-0.10}$	$1.21^{+0.45}_{-0.42}$

$H \rightarrow \gamma\gamma$ decay. For each production-times-decay mode, we note that the measurements of the $H \rightarrow \gamma\gamma$ decay in tH production, $H \rightarrow ZZ^*$ in WH, ZH, ttH and tH, $H \rightarrow WW^*$ in WH and ZH, and $H \rightarrow bb$ in ggF+bbH and VBF are now challenging and they might be significantly improved in near future.

In Ref. [13] and Refs. [3, 4] for the LHC Run 1 and Run 2 data, respectively, also presented are the individual signal strengths for Higgs boson production processes which have been obtained assuming that the Higgs boson branching fractions are the same as in the SM and the individual signal strengths for Higgs boson decay modes which have been extracted assuming that the Higgs boson production cross sections are the same as in the SM. We collect them in Table V. Comparing the ATLAS+CMS combined Run 1 signal strengths with the either ATLAS or CMS Run 2 ones, we observe that, overall, each of the signal strengths is more precisely measured with the errors reduced by the factor of about 2 and the most of their central values approach nearer to the SM value of 1. Especially, the error of the ttH production is reduced by the factor of about 3 and the production mode has been evidenced in Run 2. Looking into the ATLAS and CMS Run 2 signal strengths, we note that the ggF production signal strength $\mu^{\text{ggF}+\text{bbH}}$ ⁹ has been most precisely measured with the errors of 7%-8% followed by μ^{VBF} with about 12% error. The signal strengths of the other production modes of WH, ZH, ttH(\oplus tH) are measured with about 20% errors. For the decays, the $\gamma\gamma$, ZZ^* , WW^* , and $\tau\tau$ modes are measured with about 10% errors while the bb mode with 15 – 20% error. The $\mu\mu$ mode is slightly better measured by CMS with 45% error.

Lastly, also available are the global signal strengths which are simplest and most restrictive among all kinds of signal strengths since they have been yielded under the assumption that all the production and decay processes scale with the same single global signal strength independently of the production and decay processes:

$$\mu_{\text{Run 1}}^{\text{Global}} = 1.09^{+0.11}_{-0.10} [13]; \quad \mu_{\text{Run 2 ATLAS}}^{\text{Global}} = 1.05 \pm 0.06 [3], \quad \mu_{\text{Run 2 CMS}}^{\text{Global}} = 1.002 \pm 0.057 [4]. \quad (3)$$

Together with the Tevatron global strength

$$\mu_{\text{Tevatron}}^{\text{Global}} = 1.44^{+0.55}_{-0.54}, \quad (4)$$

we observe that the global signal strengths have been always consistent with the SM value of 1 and are converging to the SM value of 1 with the ever-decreasing errors. Combining the three LHC global strengths and the Tevatron one, we have obtained

$$\mu_{\text{Tevatron} \oplus [13] \oplus [3] \oplus [4]}^{\text{Global}} = 1.036 \pm 0.038. \quad (5)$$

For the above result, we assume that each global strength is Gaussian distributed and correlation among them could be ignored.

In this work, we use the following 76 Higgs signal strengths which have been extracted for different combinations of Higgs boson production and decay processes without imposing any assumptions:

- Tevatron: 3 signal strengths based on 10/fb at 19.6 TeV, see Table I
- LHC Run 1 (ATLAS+CMS): 20 signal strengths based on about 2×25 /fb at $7 \oplus 8$ TeV, see Table II

⁹ Note that the bbH process is experimentally indistinguishable from ggF production. Though the SM bbH cross section is much smaller than the SM ggF one by the factor of about 100, the two production processes are grouped together for the more precise treatment.

TABLE VI. *LHC signal strengths for individual Higgs production processes and decay modes obtained from the signal strengths in Table II (Run 1), Table III (Run 2 ATLAS), and Table IV (Run 2 CMS). Note that, being different from the signal strengths in Table V, no assumptions have been imposed on the Higgs boson branching ratios and/or production cross sections. The combined signal strengths are shown in the last line including all the 76 signal strengths available.*

LHC	Production process					Decay mode					
	ggF(\oplus bbH)	VBF	WH	ZH	ttH \oplus tH	$\gamma\gamma$	ZZ^*	WW^*	bb	$\tau\tau$	$\mu\mu$
Run 1 (Table II)	$0.99^{+0.11}_{-0.11}$	$1.17^{+0.20}_{-0.20}$	$0.79^{+0.33}_{-0.33}$	$0.78^{+0.34}_{-0.34}$	$1.99^{+0.61}_{-0.63}$	$1.11^{+0.16}_{-0.17}$	$1.03^{+0.28}_{-0.29}$	$1.01^{+0.14}_{-0.14}$	$0.68^{+0.29}_{-0.29}$	$1.04^{+0.25}_{-0.25}$	—
Run 2 ATLAS (Table III)	$1.03^{+0.06}_{-0.06}$	$1.12^{+0.12}_{-0.12}$	$1.22^{+0.23}_{-0.23}$	$0.83^{+0.20}_{-0.20}$	$0.91^{+0.20}_{-0.21}$	$1.04^{+0.09}_{-0.09}$	$1.01^{+0.10}_{-0.10}$	$1.20^{+0.12}_{-0.12}$	$0.89^{+0.15}_{-0.15}$	$0.95^{+0.13}_{-0.15}$	$1.11^{+0.62}_{-0.62}$
Run 2 CMS (Table IV)	$0.93^{+0.07}_{-0.07}$	$0.81^{+0.11}_{-0.11}$	$1.40^{+0.24}_{-0.24}$	$1.50^{+0.26}_{-0.26}$	$1.06^{+0.17}_{-0.17}$	$1.20^{+0.12}_{-0.12}$	$0.90^{+0.13}_{-0.13}$	$0.95^{+0.10}_{-0.11}$	$1.06^{+0.23}_{-0.24}$	$0.79^{+0.11}_{-0.11}$	$1.14^{+0.49}_{-0.49}$
Combined (76 signal strengths)	$0.99^{+0.04}_{-0.04}$	$0.98^{+0.08}_{-0.08}$	$1.20^{+0.15}_{-0.15}$	$1.03^{+0.14}_{-0.14}$	$1.04^{+0.13}_{-0.13}$	$1.10^{+0.07}_{-0.07}$	$0.97^{+0.08}_{-0.08}$	$1.04^{+0.07}_{-0.07}$	$0.90^{+0.12}_{-0.12}$	$0.87^{+0.08}_{-0.08}$	$1.13^{+0.38}_{-0.38}$

- LHC Run 2 (ATLAS): 25 signal strengths based on 139/fb at 13 TeV, see Table III
- LHC Run 2 (CMS): 28 signal strengths based on 138/fb at 13 TeV, see Table IV

From the above 76 signal strengths, we obtain the following global signal strength

$$\mu_{76 \text{ signal strengths}}^{\text{Global}} = 1.012 \pm 0.034, \quad (6)$$

which is consistent with the global signal strength given by Eq. (5) which is obtained from the four LHC and Tevatron global signal strengths.

Observing the difference between the two global signal strengths, see Eqs. (5) and (6), we also show the LHC signal strengths for individual Higgs production processes and decay modes in Table VI, obtained by using the LHC signal strengths in Table II (Run 1), Table III (Run 2 ATLAS), and Table IV (Run 2 CMS). For the production signal strengths, we neglect the tH production process in ATLAS Run 2 and all the mixed-production processes except ttH \oplus tH. Note that, being different from the individual signal strengths in Table V, no assumptions have been imposed on the Higgs boson branching ratios and/or production cross sections. The combined individual production and decay signal strengths obtained by using all the 76 signal strengths are shown in the last line of Table VI. Since any information on correlations among Run 1, Run 2 ATLAS and Run 2 CMS datasets are not currently available, we ignore them accordingly.

III. FRAMEWORK

For the conventions and notations of the model-independent couplings of the 125 GeV Higgs-boson H to the SM particles, we closely follow Ref. [47]. To be most general, we assume that H is a CP-mixed scalar. And then, in terms of the CP-violating (CPV) Higgs couplings, we calculate the theoretical signal strengths used for our global fits. Especially, we have included the production signal strength for the tH process to accommodate the new feature of the LHC Run 2 data and considered the ggF production process beyond leading order in QCD to match the level of precision of the LHC Run 2 data.

A. Higgs Couplings

The interactions of a generic neutral Higgs boson H with the SM charged leptons and quarks, without loss of generality, could be described by the following Lagrangian:

$$\mathcal{L}_{H\bar{f}f} = - \sum_{f=\{\ell,q\}} \frac{gm_f}{2M_W} \left[\bar{f} \left(g_{H\bar{f}f}^S + ig_{H\bar{f}f}^P \gamma_5 \right) f \right] H \quad (7)$$

where $g_{H\bar{f}f}^S$ and $g_{H\bar{f}f}^P$ stand for the H coupling to the scalar and pseudoscalar fermion bilinears, respectively, and they are normalized as $g_{H\bar{f}f}^S = 1$ and $g_{H\bar{f}f}^P = 0$ in the SM limit. The interactions of H with the massive vector bosons $V = Z, W$ are described by

$$\mathcal{L}_{HVV} = g M_W \left(g_{HW} W_\mu^+ W^{-\mu} + g_{HZ} \frac{1}{2c_W^2} Z_\mu Z^\mu \right) H, \quad (8)$$

in terms of the normalized couplings of g_{HWW} and g_{HZZ} with $g = e/s_W$ the $SU(2)_L$ gauge coupling and the weak mixing angle θ_W : $c_W \equiv \cos\theta_W$ and $s_W \equiv \sin\theta_W$. For the SM couplings, we have $g_{HWW} = g_{HZZ} \equiv g_{HVV} = 1$, respecting the custodial symmetry between the W and Z bosons.

The loop-induced Higgs couplings to two photons are described through the following amplitude for the radiative decay process $H \rightarrow \gamma\gamma$:

$$\mathcal{M}_{\gamma\gamma H} = -\frac{\alpha(0)M_H^2}{4\pi v} \left\{ S^\gamma(M_H) (\epsilon_{1\perp}^* \cdot \epsilon_{2\perp}^*) - P^\gamma(M_H) \frac{2}{M_H^2} \langle \epsilon_1^* \epsilon_2^* k_1 k_2 \rangle \right\}, \quad (9)$$

by introducing the scalar and pseudoscalar form factors denoted by S^γ and P^γ , respectively, with $k_{1,2}$ and $\epsilon_{1,2}$ being the four-momenta and wave vectors of the two photons.¹⁰ Retaining only the dominant contributions from third-generation fermions and the charged gauge bosons W^\pm and introducing two residual form factors ΔS^γ and ΔP^γ to parametrize contributions from the triangle loops in which non-SM charged particles are running, the scalar and pseudoscalar form factors are given by

$$\begin{aligned} S^\gamma(M_H) &= 2 \sum_{f=b,t,\tau} N_C^f Q_f^2 g_{H\bar{f}f}^S F_{sf}(\tau_f) - g_{HWW} F_1(\tau_W) + \Delta S^\gamma; \\ P^\gamma(M_H) &= 2 \sum_{f=b,t,\tau} N_C^f Q_f^2 g_{H\bar{f}f}^P F_{pf}(\tau_f) + \Delta P^\gamma, \end{aligned} \quad (10)$$

where $N_C^f = 3$ for quarks and $N_C^f = 1$ for charged leptons, Q_f the electric charge of the fermion f , $\tau_f = M_H^2/4m_f^2$ and $\tau_W = M_H^2/4M_W^2$. For the definitions and behavior of the loop functions $F_{sf,pf,1}$, see, for example, Ref. [47]. Taking $M_H = 125$ GeV, for example, one may obtain the following estimation of the form factors:

$$\begin{aligned} S^\gamma &= -8.324 g_{HWW} + 1.826 g_{H\bar{t}t}^S + (-0.020 + 0.025 i) g_{H\bar{b}b}^S + (-0.024 + 0.022 i) g_{H\bar{\tau}\tau}^S + \Delta S^\gamma; \\ P^\gamma &= 2.771 g_{H\bar{t}t}^P + (-0.022 + 0.025 i) g_{H\bar{b}b}^P + (-0.025 + 0.022 i) g_{H\bar{\tau}\tau}^P + \Delta P^\gamma, \end{aligned} \quad (11)$$

in terms of the Higgs-fermion-fermion and HWW couplings given in Eqs. (7) and (8) supplemented by the two residual form factors ΔS^γ and ΔP^γ . In the SM limit where $g_{HWW} = g_{H\bar{f}f}^S = 1$ and $g_{H\bar{f}f}^P = \Delta S^\gamma = \Delta P^\gamma = 0$, we have $S_{SM}^\gamma = -6.542 + 0.046 i$ and $P_{SM}^\gamma = 0$.

The loop-induced Higgs couplings to two gluons are similarly described through the amplitude

$$\mathcal{M}_{ggH}^{ab} = -\frac{\alpha_s(M_H) M_H^2 \delta^{ab}}{4\pi v} \left\{ S^g(M_H) (\epsilon_{1\perp}^* \cdot \epsilon_{2\perp}^*) - P^g(M_H) \frac{2}{M_H^2} \langle \epsilon_1^* \epsilon_2^* k_1 k_2 \rangle \right\}, \quad (12)$$

where a and b ($a, b = 1$ to 8) are indices of the eight generators in the $SU(3)$ adjoint representation, $k_{1,2}$ the four momenta of the two gluons and $\epsilon_{1,2}$ the wave vectors of the corresponding gluons. Referring to Ref. [47] again for the detailed description and evaluation of the amplitude, the scalar and pseudoscalar form factors are given by

$$S^g(M_H) = \sum_{f=b,t,c} g_{H\bar{f}f}^S F_{sf}(\tau_f) + \Delta S^g; \quad P^g(M_H) = \sum_{f=b,t,c} g_{H\bar{f}f}^P F_{pf}(\tau_f) + \Delta P^g, \quad (13)$$

retaining only the dominant contributions from third-generation and charm quarks and introducing ΔS^g and ΔP^g to parametrize contributions from the triangle loops in which non-SM colored particles are running. Taking $M_H = 125$ GeV, one might have

$$\begin{aligned} S^g &= 0.688 g_{H\bar{t}t}^S + (-0.043 + 0.063 i) g_{H\bar{b}b}^S + (-0.009 + 0.008 i) g_{H\bar{c}c}^S + \Delta S^g; \\ P^g &= 1.047 g_{H\bar{t}t}^P + (-0.050 + 0.063 i) g_{H\bar{b}b}^P + (-0.010 + 0.008 i) g_{H\bar{c}c}^P + \Delta P^g, \end{aligned} \quad (14)$$

in terms of the Higgs-fermion-fermion couplings given in Eq. (7) supplemented by the two residual form factors of ΔS^g and ΔP^g . We have $S_{SM}^g = 0.636 + 0.071 i$ and $P_{SM}^g = 0$ in the SM limit.

¹⁰ For the detailed description and evaluation of the amplitude, we refer to Ref. [47] while, in this work, we concentrate on the two form factors which are most relevant regarding this work.

B. Theoretical Signal Strengths

In this work, to calculate the theoretical signal strengths, we adopt the factorization assumption under which the production and decay processes are well separated like as in the resonant s -channel Higgs production in the narrow-width approximation and neglect nonresonant and interference effects. Under the assumption, for a specific production-times-decay process, each theoretical signal strength is given by the product of the production and decay signal strengths as

$$\mu(\mathcal{P}, \mathcal{D}) \simeq \hat{\mu}(\mathcal{P}) \hat{\mu}(\mathcal{D}). \quad (15)$$

Here \mathcal{P} stands for one of the six productions processes of ggF, VBF, WH, ZH, ttH, and tH while \mathcal{D} one of the six decay products of $\gamma\gamma$, ZZ^* , WW^* , bb , $\tau\tau$, and $\mu\mu$ which are supposed to be visible at the LHC in this work.

The productions signal strength for the production process \mathcal{P} is given by

$$\hat{\mu}(\mathcal{P}) = \frac{\sigma_{\mathcal{P}}}{\sigma_{\mathcal{P}}^{\text{SM}}}. \quad (16)$$

On the other hand, the decay signal strength for the process $H \rightarrow \mathcal{D}$ is given by

$$\hat{\mu}(\mathcal{D}) = \frac{B(H \rightarrow \mathcal{D})}{B(H_{\text{SM}} \rightarrow \mathcal{D})} = \frac{\Gamma(H \rightarrow \mathcal{D})}{\Gamma(H_{\text{SM}} \rightarrow \mathcal{D})} \times \frac{\Gamma_{\text{tot}}(H_{\text{SM}})}{\Gamma_{\text{tot}}(H) + \Delta\Gamma_{\text{tot}}}, \quad (17)$$

with the branching fraction of each decay mode defined by

$$B(H \rightarrow \mathcal{D}) = \frac{\Gamma(H \rightarrow \mathcal{D})}{\Gamma_{\text{tot}}(H) + \Delta\Gamma_{\text{tot}}}, \quad B(H_{\text{SM}} \rightarrow \mathcal{D}) = \frac{\Gamma(H_{\text{SM}} \rightarrow \mathcal{D})}{\Gamma_{\text{tot}}(H_{\text{SM}})}. \quad (18)$$

Note that an arbitrary non-SM contribution $\Delta\Gamma_{\text{tot}}$ to the total decay width is introduced to parametrize invisible Higgs decays into non-SM and/or undetected particles.¹¹ We observe that the partial and total decay widths of $\Gamma(H \rightarrow \mathcal{D})$ and $\Gamma_{\text{tot}}(H)$ becomes the SM ones of $\Gamma(H_{\text{SM}} \rightarrow \mathcal{D})$ and $\Gamma_{\text{tot}}(H_{\text{SM}})$, respectively, when $g_{H\bar{f}f}^S = 1$, $g_{H\bar{f}f}^P = 0$, $g_{HWW, HZZ} = 1$, and $\Delta S^{\gamma,g} = \Delta P^{\gamma,g} = 0$. To calculate the decay widths of a generic Higgs boson, we meticulously follow the recent review on the decays of Higgs bosons [47] which provides explicit analytical expressions and supplemental materials for the individual partial decay widths as precisely as possible by including the state-of-the-art theoretical calculations of QCD corrections together with the SM electroweak corrections.

At leading order (LO), the six production signal strengths are given by

$$\begin{aligned} \hat{\mu}(\text{ggF})^{\text{LO}} &= \frac{|S^g(M_H)|^2 + |P^g(M_H)|^2}{|S_{\text{SM}}^g(M_H)|^2}; \quad \hat{\mu}(\text{bbH}) = (g_{H\bar{b}b}^S)^2 + (g_{H\bar{b}b}^P)^2, \\ \hat{\mu}(\text{VBF}) &= 0.73 g_{HWW}^2 + 0.27 g_{HZZ}^2, \\ \hat{\mu}(\text{WH}) &= g_{HWW}^2, \\ \hat{\mu}(\text{ZH}) &= g_{HZZ}^2, \\ \hat{\mu}(\text{ttH}) &= (g_{H\bar{t}t}^S)^2 + (g_{H\bar{t}t}^P)^2, \\ \hat{\mu}(\text{tH}) &= 2.99 [(g_{H\bar{t}t}^S)^2 + (g_{H\bar{t}t}^P)^2] + 3.38 g_{HWW}^2 - 5.37 g_{H\bar{t}t}^S g_{HWW}, \end{aligned} \quad (19)$$

in terms of the relevant form factors and couplings. For $\hat{\mu}(\text{VBF})$, we consider the W - and Z -boson fusion processes separately and the decomposition coefficients are given by the ratios of the SM cross sections of $\sigma_{W \rightarrow H}^{\text{SM}}/\sigma_{\text{VBF}}^{\text{SM}} \simeq 0.73$ and $\sigma_{ZZ \rightarrow H}^{\text{SM}}/\sigma_{\text{VBF}}^{\text{SM}} \simeq 0.27$ which are largely independent of \sqrt{s} .

For the tH production, we consider the two main production processes of $q'b \rightarrow tHq$ (tHq) and $gb \rightarrow tHW$ (tHW). In the 5-flavor scheme (5FS), the LO tHq process is mediated by the t -channel exchange of the W boson with H radiated from W or t . The LO tHW process is mediated by the s -channel exchange of the b quark with H , again, radiated from W or t . Both the production processes contain the two types of diagrams which involve the top-Yukawa and gauge-Higgs

¹¹ Precisely, we calculate the total Higgs decay width by summing over the 9 partial widths of the Higgs decay modes into $b\bar{b}$, WW^* , gg , $\tau^+\tau^-$, $c\bar{c}$, ZZ^* , $\gamma\gamma$, $Z\gamma$, and $\mu^+\mu^-$. Therefore, $\Delta\Gamma_{\text{tot}}$ addresses either all the Higgs decays into particles other than these 9 final states such as dark matter and light quarks or decays into gg , $c\bar{c}$, and $Z\gamma$ beyond the SM.

TABLE VII. The LO tHq and tHW cross sections in fb at $\sqrt{s} = 13$ TeV for the three values of $g_{H\bar{t}t}^S$ taking $g_{H\bar{t}t}^P = 0$. To calculate the cross sections, we use MG5_aMC@NLO [48] with NN23LO PDF set [49] and no generator-level cuts are applied. $M_H = 125$ GeV and $M_t = 172.5$ GeV are taken.

$\sqrt{s} = 13$ TeV	$g_{H\bar{t}t}^S = +1$ (SM)	$g_{H\bar{t}t}^S = 0$	$g_{H\bar{t}t}^S = -1$
tHq	71.8	264	890
tHW	17.2	36.7	155

couplings and the destructive interference between them is very significant, leading to the large negative value for the coefficient of the term proportional to the product of the $g_{H\bar{t}t}^S$ and g_{HWW} couplings. Using the LO tHq and tHW cross sections for the three values of $g_{H\bar{t}t}^S = +1, 0, -1$ taking $g_{H\bar{t}t}^P = 0$, see Table VII, we derive the three decomposition coefficients of the tHq and tHW processes as follows:

$$\begin{aligned}\widehat{\mu}(\text{tHq}) &= 3.02 [(g_{H\bar{t}t}^S)^2 + (g_{H\bar{t}t}^P)^2] + 3.68 g_{HWW}^2 - 5.70 g_{H\bar{t}t}^S g_{HWW}, \\ \widehat{\mu}(\text{tHW}) &= 2.88 [(g_{H\bar{t}t}^S)^2 + (g_{H\bar{t}t}^P)^2] + 2.14 g_{HWW}^2 - 4.02 g_{H\bar{t}t}^S g_{HWW},\end{aligned}\quad (20)$$

and, by combining them using the SM LO cross sections given in Table VII, we finally have

$$\widehat{\mu}(\text{tH}) = \frac{\sigma_{\text{tHq}}^{\text{SM}} \widehat{\mu}(\text{tHq}) + \sigma_{\text{tHW}}^{\text{SM}} \widehat{\mu}(\text{tHW})}{\sigma_{\text{tHq}}^{\text{SM}} + \sigma_{\text{tHW}}^{\text{SM}}} = 2.99 [(g_{H\bar{t}t}^S)^2 + (g_{H\bar{t}t}^P)^2] + 3.38 g_{HWW}^2 - 5.37 g_{H\bar{t}t}^S g_{HWW}, \quad (21)$$

which gives $\widehat{\mu}(\text{tH})$ in Eq. 19.

Note that the LO ggF production signal strength given in Eq. (19) should be reliable only when higher order corrections to the numerator and those to the denominator are largely canceled out in the ratio $\widehat{\mu}(\text{ggF}) = \sigma_{\text{ggF}}/\sigma_{\text{ggF}}^{\text{SM}}$. But, unfortunately, it turns out that the QCD corrections to the diagrams in which top quarks are running and those to the diagrams in which bottom quarks are running are significantly different [50] and, accordingly, the LO ggF production signal strength given in Eq. (19) is unreliable. In this work, combining ggF and bbH beyond LO, we use ¹²

$$\begin{aligned}\widehat{\mu}(\text{ggF} + \text{bbH}) &= \frac{\sigma_{\text{ggF}}^{\text{SM}} \widehat{\mu}(\text{ggF}) + \sigma_{\text{bbH}}^{\text{SM}} \widehat{\mu}(\text{bbH})}{\sigma_{\text{ggF}}^{\text{SM}} + \sigma_{\text{bbH}}^{\text{SM}}} \\ &= \sum_{X=S,P} [c_{tt}^X (g_{H\bar{t}t}^X)^2 + c_{bb}^X (g_{H\bar{b}b}^X)^2 + c_{tb}^X (g_{H\bar{t}t}^X g_{H\bar{b}b}^X) + c_{tc}^X (g_{H\bar{t}t}^X g_{H\bar{c}c}^X) + c_{t\Delta}^X (g_{H\bar{t}t}^X \Delta X^g) + c_{\Delta\Delta}^X (\Delta X^g)^2],\end{aligned}\quad (22)$$

with the decomposition coefficients given in Table VIII. In comparison to Refs. [51, 52], we exploit the N³LO (NNLO) production cross sections obtained by using SusHi-1.7.0 [53, 54] for several combinations of the CP-even (CP-odd) Yukawa couplings having in mind the possibility that H is a CP-mixed state. We further consider the beyond-LO effects on the contributions from the triangle loops in which non-SM heavy particles are running. For the detailed derivation of the coefficients for $\widehat{\mu}(\text{ggF})$ beyond LO in QCD, see Appendix A.

TABLE VIII. The decomposition coefficients $c_{qq^{(\prime)}}^X$, $c_{t\Delta}^X$, and $c_{\Delta\Delta}^X$ for $\widehat{\mu}(\text{ggF} + \text{bbH})$ beyond LO in QCD, see Eq. (22), at $\sqrt{s} = 7 \oplus 8$ TeV and 13 TeV. In the third and fourth lines, the LO coefficients obtained by using Eq. (14) are also shown for comparisons. The Run 1 and Run 2 LO coefficients are slightly different because the ratio $\sigma_{\text{bbH}}^{\text{SM}}/\sigma_{\text{ggF}}^{\text{SM}}$ depends on \sqrt{s} , see Eq. (22). $M_H = 125$ GeV and $M_t = 172.5$ GeV are taken.

	c_{tt}^S	c_{bb}^S	c_{tb}^S	c_{tc}^S	$c_{t\Delta}^S$	$c_{\Delta\Delta}^S$	c_{tt}^P	c_{bb}^P	c_{tb}^P	c_{tc}^P	$c_{t\Delta}^P$	$c_{\Delta\Delta}^P$
$\sqrt{s} = 7 \oplus 8$ TeV	1.050	0.018	-0.054	-0.010	1.814	0.784	2.244	0.018	-0.104	-0.019	2.690	0.806
$\sqrt{s} = 13$ TeV	1.043	0.018	-0.050	-0.009	1.778	0.758	2.222	0.018	-0.096	-0.018	2.632	0.779
LO ($\sqrt{s} = 7 \oplus 8$ TeV)	1.1452	0.0248	-0.1433	-0.0315	3.3278	2.4176	2.6507	0.0264	-0.2512	-0.0508	5.0629	2.4176
LO ($\sqrt{s} = 13$ TeV)	1.1447	0.0253	-0.1433	-0.0314	3.3262	2.4164	2.6494	0.0269	-0.2510	-0.0508	5.0604	2.4164

¹² To combine ggF and bbH, we use the SM cross sections for $g_{H\bar{t}t}^S = g_{H\bar{b}b}^S = g_{H\bar{c}c}^S = 1$ given in Table XVIII obtained by using SusHi-1.7.0.

TABLE IX. The SM cross sections from Ref. [55] used for Eq. (23) taking $M_H = 125$ GeV: ggF from Table 191, VBF from Tables 25 and 26, WH from Table 223, ZH from Table 225, ttH from Table 231, tHq from Table 237, and bbH from Table 247. On the other hand, the 13-TeV tHW cross section is from Ref. [56].

\sqrt{s} (TeV)	ggF (pb)	VBF (fb)	WH (fb)	ZH (fb)	ttH (fb)	tHq (fb)	tHW (fb)	bbH (fb)
7	16.85	1241.4	577.30	339.10	88.78	12.26	–	155.20
8	21.42	1601.2	702.50	420.70	133.0	18.69	–	202.10
13	48.57	3781.7	1373.00	883.70	507.2	74.25	15.2	488.00

For the mixed-production mode involved with two production processes or more, we use the following production signal strength weighted by the cross sections of all the production processes involved:

$$\hat{\mu}(\mathcal{Q}) = \frac{\sum_{\mathcal{P}_i \subset \mathcal{Q}} \sigma_{\mathcal{P}_i}^{\text{SM}} \hat{\mu}(\mathcal{P}_i)}{\sum_{\mathcal{P}_i \subset \mathcal{Q}} \sigma_{\mathcal{P}_i}^{\text{SM}}}, \quad (23)$$

where, for the SM cross sections, we adopt those given in Ref. [55], see Table IX. Explicitly, for the Run 2 mixed-productions modes at $\sqrt{s} = 13$ TeV, we use

$$\begin{aligned} \hat{\mu}(\text{ggF} + \text{bbH} \oplus \text{VBF}) &= 0.928 \hat{\mu}(\text{ggF} + \text{bbH}) + 0.072 \hat{\mu}(\text{VBF}) \\ &= 0.969 (g_{H\bar{t}t}^S)^2 + 0.016 (g_{H\bar{b}b}^S)^2 - 0.046 (g_{H\bar{t}t}^S g_{H\bar{b}b}^S) - 0.009 (g_{H\bar{t}t}^S g_{H\bar{c}c}^S) + 1.651 (g_{H\bar{t}t}^S \Delta S^g) + 0.703 (\Delta S^g)^2 \\ &\quad + 2.063 (g_{H\bar{t}t}^P)^2 + 0.017 (g_{H\bar{b}b}^P)^2 - 0.089 (g_{H\bar{t}t}^P g_{H\bar{b}b}^P) - 0.016 (g_{H\bar{t}t}^P g_{H\bar{c}c}^P) + 2.444 (g_{H\bar{t}t}^P \Delta P^g) + 0.724 (\Delta P^g)^2 \\ &\quad + 0.052 g_{HWW}^2 + 0.019 g_{HZZ}^2; \\ \hat{\mu}(\text{WH} \oplus \text{ZH}) &= 0.608 g_{HWW}^2 + 0.392 g_{HZZ}^2; \\ \hat{\mu}(\text{ttH} \oplus \text{tH}) &= 1.299 [(g_{H\bar{t}t}^S)^2 + (g_{H\bar{t}t}^P)^2] + 0.507 g_{HWW}^2 - 0.806 g_{H\bar{t}t}^S g_{HWW}; \\ \hat{\mu}(\text{ggF} + \text{bbH} \oplus \text{ttH} \oplus \text{tH}) &= 0.988 \hat{\mu}(\text{ggF} + \text{bbH}) + 0.012 \hat{\mu}(\text{ttH} \oplus \text{tH}) \\ &= 1.047 (g_{H\bar{t}t}^S)^2 + 0.017 (g_{H\bar{b}b}^S)^2 - 0.049 (g_{H\bar{t}t}^S g_{H\bar{b}b}^S) - 0.009 (g_{H\bar{t}t}^S g_{H\bar{c}c}^S) + 1.757 (g_{H\bar{t}t}^S \Delta S^g) + 0.749 (\Delta S^g)^2 \\ &\quad + 2.211 (g_{H\bar{t}t}^P)^2 + 0.018 (g_{H\bar{b}b}^P)^2 - 0.095 (g_{H\bar{t}t}^P g_{H\bar{b}b}^P) - 0.017 (g_{H\bar{t}t}^P g_{H\bar{c}c}^P) + 2.601 (g_{H\bar{t}t}^P \Delta P^g) + 0.770 (\Delta P^g)^2 \\ &\quad - 0.010 g_{H\bar{t}t}^S g_{HWW} + 0.006 g_{HWW}^2; \\ \hat{\mu}(\text{VBF} \oplus \text{WH} \oplus \text{ZH}) &= 0.685 g_{HWW}^2 + 0.315 g_{HZZ}^2. \end{aligned} \quad (24)$$

C. χ^2 Analysis

Once all the theoretical signal strengths $\mu(\mathcal{Q}, \mathcal{D}) \simeq \hat{\mu}(\mathcal{Q}) \hat{\mu}(\mathcal{D})$, each of which is associated with the specific production process of \mathcal{Q} and the decay mode $H \rightarrow \mathcal{D}$, have been obtained, one may carry out a chi-square analysis. For the Tevatron data in which observables are uncorrelated, each χ^2 is given by

$$\chi^2(\mathcal{Q}, \mathcal{D}) = \frac{[\mu(\mathcal{Q}, \mathcal{D}) - \mu^{\text{EXP}}(\mathcal{Q}, \mathcal{D})]^2}{[\sigma^{\text{EXP}}(\mathcal{Q}, \mathcal{D})]^2}, \quad (25)$$

where $\mu^{\text{EXP}}(\mathcal{Q}, \mathcal{D})$ and $\sigma^{\text{EXP}}(\mathcal{Q}, \mathcal{D})$ denote the experimentally measured signal strength and the associated error, respectively. For the LHC Run 1 and Run 2 data, taking account of correlation among the observables in each set of data, we use χ^2 for n correlated observables:

$$\chi_n^2 = \sum_{i,j=1}^n \frac{(\mu_i - \mu_i^{\text{EXP}})}{\sigma_i^{\text{EXP}}} (\rho^{-1})_{ij} \frac{(\mu_j - \mu_j^{\text{EXP}})}{\sigma_j^{\text{EXP}}}, \quad (26)$$

where the indices i, j count n correlated production-times-decay modes and ρ denotes the relevant $n \times n$ correlation matrix satisfying the relations of $\rho_{ij} = \rho_{ji}$ and $\rho_{ii} = 1$. If $\rho_{ij} = \delta_{ij}$, we note that χ_n^2 reduces to

$$\chi_n^2 = \sum_{i=1}^n \frac{(\mu_i - \mu_i^{\text{EXP}})^2}{(\sigma_i^{\text{EXP}})^2},$$

i.e., the sum of χ^2 of each uncorrelated observable.

For our chi-square analysis, we consider two statistical measures: (i) goodness of fit (gof) quantifying the agreement with the experimentally measured signal strengths in a given fit, and (ii) p -value against the SM for a given fit hypothesis to be compatible with the SM one: ¹³

$$\text{goodness of fit (gof)} = \int_{\chi_{\min}^2}^{\infty} f[x, n] dx; \quad p\text{-value against the SM} = \int_{\chi_{\text{SM}}^2 - \chi_{\min}^2}^{\infty} f[x, m] dx,$$

where n is the degree of freedom (dof) and m the number of fitting parameters against the SM null hypothesis with $\mu = 1$. In our case, we have $n = 76 - m$. The probability density function is given by

$$f[x, l] = \frac{x^{l/2-1} e^{-x/2}}{2^{l/2} \Gamma(l/2)},$$

with $\Gamma(l/2)$ being the gamma function. The goodness of fit approaches to 1 when the value of χ^2 per degree of freedom becomes smaller. On the other hand, the p -value for compatibility with the SM hypothesis approaches to 1 when the test hypothesis becomes more and more SM-like.

IV. GLOBAL FITS

Now we are ready to perform global fits of the Higgs boson couplings to the full Higgs datasets collected at the LHC. Throughout this section, we use the following short notations for the 125 GeV Higgs H couplings to the SM particles:

$$\begin{aligned} C_W &= g_{HWW}, & C_Z &= g_{HZZ}; \\ C_t^{S,P} &= g_{H\bar{t}t}^{S,P}, & C_c^{S,P} &= g_{H\bar{c}c}^{S,P}, & C_b^{S,P} &= g_{H\bar{b}b}^{S,P}, & C_\tau^{S,P} &= g_{H\bar{\tau}\tau}^{S,P}, & C_\mu^{S,P} &= g_{H\bar{\mu}\mu}^{S,P}. \end{aligned} \quad (27)$$

Depending on specific models, all the Higgs couplings are not independent. For example, the Higgs couplings to the massive vector bosons could be the same as in the SM and the Yukawa couplings could be the same separately in the up- and down-quark and charged-lepton sectors. In this case, we denote the couplings as:

$$C_V = C_W = C_Z; \quad C_u^{S,P} = C_t^{S,P} = C_c^{S,P}, \quad C_d^{S,P} = C_b^{S,P}, \quad C_\ell^{S,P} = C_\tau^{S,P} = C_\mu^{S,P}. \quad (28)$$

Further, some of the Yukawa couplings could be the same like as in the four types of two Higgs doublet models (2HDMs) which are classified according to the Glashow-Weinberg condition [58] to avoid unwanted tree-level Higgs-mediated flavor-changing neutral currents (FCNCs). In this case, we denote the Higgs couplings as: ¹⁴

$$\begin{aligned} C_f^{S,P} &= C_u^{S,P} = C_d^{S,P} = C_\ell^{S,P} \text{ (as in type-I 2HDM)}, \\ C_u^{S,P}, C_{d\ell}^{S,P} &= C_d^{S,P} = C_\ell^{S,P} \text{ (as in type-II 2HDM)}, \\ C_{ud}^{S,P} &= C_u^{S,P} = C_d^{S,P}, \quad C_\ell^{S,P} \text{ (as in type-III 2HDM)}, \\ C_{u\ell}^{S,P} &= C_u^{S,P} = C_\ell^{S,P}, \quad C_d^{S,P} \text{ (as in type-IV 2HDM)}. \end{aligned} \quad (29)$$

Last but not least, when all the Higgs couplings of C_V and C_f^S to the SM particles scale with a single parameter as in, for example, Higgs-portal [60] and/or inert Higgs models, we denote the coupling as:

$$C_{Vf} = C_W = C_Z = C_t^S = C_c^S = C_b^S = C_\tau^S = C_\mu^S. \quad (30)$$

¹³ For the second statistical measure to test the SM null hypothesis with $\mu = 1$, we use the likelihood ratio $\lambda(1) = L(1)/L(\hat{\mu})$: see Eq. (40.49) and below in the 2023 edition of the review “**40. Statistics**” by G. Cowan in Ref. [57]. Note that, in the limit where the data sample is very large, the distribution of $-2 \ln \lambda(1) = \chi_{\text{SM}}^2 - \chi_{\min}^2$ approaches a χ^2 distribution with the number of degrees of freedom being equal to the number of fitting parameters.

¹⁴ In this work, we adopt the conventions and notations of 2HDMs as in Ref. [59].

Our fits are categorized into the CP-conserving (CPC) and CP-violating (CPV) fits as in the previous studies [6, 7, 12]. The CPC fits have been performed assuming that $C_f^P = 0$ and $\Delta P^\gamma = \Delta P^g = 0$ and, in this case, we have 10 varying fitting parameters which might be grouped into the non-SM and SM ones as follow:

$$\begin{aligned} \text{CPC parameters} &= \left\{ \Delta\Gamma_{\text{tot}}, \Delta S^\gamma, \Delta S^g \right\}_{\text{non-SM}} \\ &\oplus \left\{ C_V = \{C_W, C_Z\}, C_f^S = \left\{ C_u^S = \{C_t^S, C_c^S\}, C_d^S = \{C_b^S\}, C_\ell^S = \{C_\tau^S, C_\mu^S\} \right\} \right\}_{\text{SM}}. \end{aligned} \quad (31)$$

The non-SM parameters describe the variation of the signal strengths due to the H couplings to non-SM particles such as light invisible and heavy charged/colored ones. One the other hand, the SM parameters address the changes of the signal strengths due to the H couplings to the SM particles of the massive vector bosons (C_V) and the up- and down-type quarks ($C_{u,d}^S$), and the charged leptons (C_ℓ^S). When the normalized Yukawa couplings of H to the SM fermions are generation and flavor independent, we have only one Yukawa parameter $C_f^S = C_u^S = C_d^S = C_\ell^S$. To be more general, one may separately vary the H couplings to the W and Z bosons (C_W and C_Z) without keeping the custodial symmetry between them and those to the top and charm quarks (C_t^S and C_c^S). The couplings to a pair of tau leptons and muons (C_τ^S and C_μ^S) also can be separately varied without assuming the lepton universality of the normalized charged-lepton Yukawa couplings. In the SM limit, the non-SM parameters are vanishing and all the SM ones take the SM value of 1. On the other hand, in the CPV fits under the assumption that H is a CP-mixed state, we have the following extended set of fitting parameters containing 17 parameters:

$$\begin{aligned} \text{CPV parameters} &= \left\{ \Delta\Gamma_{\text{tot}}, \{\Delta S^\gamma, \Delta P^\gamma\}, \{\Delta S^g, \Delta P^g\} \right\}_{\text{non-SM}} \\ &\oplus \left\{ C_V = \{C_W, C_Z\}, C_f^S = \left\{ C_u^S = \{C_t^S, C_c^S\}, C_d^S = \{C_b^S\}, C_\ell^S = \{C_\tau^S, C_\mu^S\} \right\} \right. \\ &\quad \left. , C_f^P = \left\{ C_u^P = \{C_t^P, C_c^P\}, C_d^P = \{C_b^P\}, C_\ell^P = \{C_\tau^P, C_\mu^P\} \right\} \right\}_{\text{SM}}. \end{aligned} \quad (32)$$

A. CP-conserving fits

We generically label the CPC fits as **CPC n** with n standing for the number of fitting parameters. Since there are 10 parameters to fit most generally, each **CPC n** contain several subfits. One can not exhaust all the possibilities and the CPC fits considered in this work are listed here: ¹⁵

- **CPC1**: in this fit, we consider the four subfits as follows:
 - IU: vary $\Delta\Gamma_{\text{tot}}$ to accommodate invisible Higgs decays into light non-SM and/or undetected particles
 - HC: vary ΔS^γ to parametrize the contributions to $H \rightarrow \gamma\gamma$ from the triangle loops in which heavy electrically charged non-SM particles are running
 - IH: vary C_{Vf} to address the case in which all the normalized Higgs couplings to the SM particles are the same like as in inert Higgs models
 - I: vary C_f^S to address the case in which all the normalized Yukawa couplings are the same like as type-I 2HDM
- **CPC2**: in this fit, we consider the eight subfits as follows:
 - IUHC: vary $\{\Delta\Gamma_{\text{tot}}, \Delta S^\gamma\}$ for the case in which the light and heavy (electrically charged) non-SM particles coexist
 - HCC: vary $\{\Delta S^\gamma, \Delta S^g\}$ for the contributions to ggF, $H \rightarrow gg$, and $H \rightarrow \gamma\gamma$ from heavy non-SM particles which are electrically charged *and* colored
 - CSB: vary $\{C_W, C_Z\}$ separately for the case in which the custodial symmetry between the W and Z bosons is broken

¹⁵ In each subfit of **CPC n** fits, note that the parameters not mentioned are assumed to take the SM value of either 0 or 1.

TABLE X. **CPCn** fits and their subfits considered in this work. Varied parameters are denoted by \surd in each subfit of **CPCn** and the SM value of either 0 or 1 is assumed otherwise.

Parameters		CPC1				CPC2							
		IU	HC	IH	I	IUHC	HCC	CSB	I	II	III	IV	HP
non-SM	$\Delta\Gamma_{\text{tot}}$	\surd	0	0	0	\surd	0	0	0	0	0	0	\surd
	ΔS^γ	0	\surd	0	0	\surd	\surd	0	0	0	0	0	0
	ΔS^g	0	0	0	0	0	\surd	0	0	0	0	0	0
SM	C_V	1	1	$\surd(C_{Vf})$	1	1	1	$\surd(C_W)$	$\surd(C_V)$	1	1	1	$\surd(C_{Vf})$
	C_f^S				$\surd(C_f^S)$			1	$\surd(C_f^S)$	$\surd(C_u^S)$	$\surd(C_{ud}^S)$	$\surd(C_{u\ell}^S)$	

Parameters		CPC3					CPC4		CPC5		CPC6
		IUHCC	II	III	IV	HP	A	HP	AHC	LUB	CSBLUB
non-SM	$\Delta\Gamma_{\text{tot}}$	\surd	0	0	0	\surd	0	\surd	0	0	0
	ΔS^γ	\surd	0	0	0	\surd	0	\surd	\surd	0	0
	ΔS^g	\surd	0	0	0	0	0	\surd	0	0	0
SM	C_V	1	$\surd(C_V)$	$\surd(C_V)$	$\surd(C_V)$	$\surd(C_{Vf})$	$\surd(C_V)$	$\surd(C_{Vf})$	$\surd(C_V)$	$\surd(C_V)$	$\surd(C_W)$
	C_f^S		$\surd(C_u^S)$	$\surd(C_{ud}^S)$	$\surd(C_{u\ell}^S)$		$\surd(C_d^S)$		$\surd(C_u^S)$	$\surd(C_d^S)$	$\surd(C_d^S)$

- I: vary $\{C_V, C_f^S\}$ for the case in which all the Yukawa couplings are as in type-I 2HDM
- II: vary $\{C_u^S, C_{d\ell}^S\}$ for the case in which the Yukawa couplings are as in type-II 2HDM
- III: vary $\{C_{ud}^S, C_\ell^S\}$ for the case in which the Yukawa couplings are as in type-III 2HDM
- IV: vary $\{C_{u\ell}^S, C_d^S\}$ for the case in which the Yukawa couplings are as in type-IV 2HDM
- HP: vary $\{\Delta\Gamma_{\text{tot}}, C_{Vf}\}$ to address the Higgs-portal case in which Higgs decays invisibly and all the Higgs couplings to the SM particles scale with a single parameter
- **CPC3**: in this fit, we consider the five subfits as follows:
 - IUHCC: vary $\{\Delta\Gamma_{\text{tot}}, \Delta S^\gamma, \Delta S^g\}$ for the case in which the light and heavy (charged *and* colored) non-SM particles coexist
 - II: vary $\{C_V, C_u^S, C_{d\ell}^S\}$ for the case in which the Yukawa couplings are as in type-II 2HDM
 - III: vary $\{C_V, C_{ud}^S, C_\ell^S\}$ for the case in which the Yukawa couplings are as in type-III 2HDM
 - IV: vary $\{C_V, C_{u\ell}^S, C_d^S\}$ for the case in which the Yukawa couplings are as in type-IV 2HDM
 - HP: vary $\{\Delta\Gamma_{\text{tot}}, \Delta S^\gamma, C_{Vf}\}$ to address the Higgs-portal case when there exist heavy electrically charged non-SM particles in addition to light particles into which H could decay
- **CPC4**: in this fit, we consider the two subfits as follows:
 - A: vary $\{C_V, C_u^S, C_d^S, C_\ell^S\}$ for the case in which the Yukawa couplings are as in aligned 2HDM (A2HDM) [61]
 - HP: vary $\{\Delta\Gamma_{\text{tot}}, \Delta S^\gamma, \Delta S^g, C_{Vf}\}$ to address the Higgs-portal case when heavy charged *and* colored non-SM particles exist in addition to light particles into which H could decay
- **CPC5**: in this fit, we consider the following two subfits:
 - AHC: vary $\{\Delta S^\gamma, C_V, C_u^S, C_d^S, C_\ell^S\}$ like as in **CPC4-A** in the presence of heavy electrically charged particles such as charged Higgs bosons contributing to $H \rightarrow \gamma\gamma$

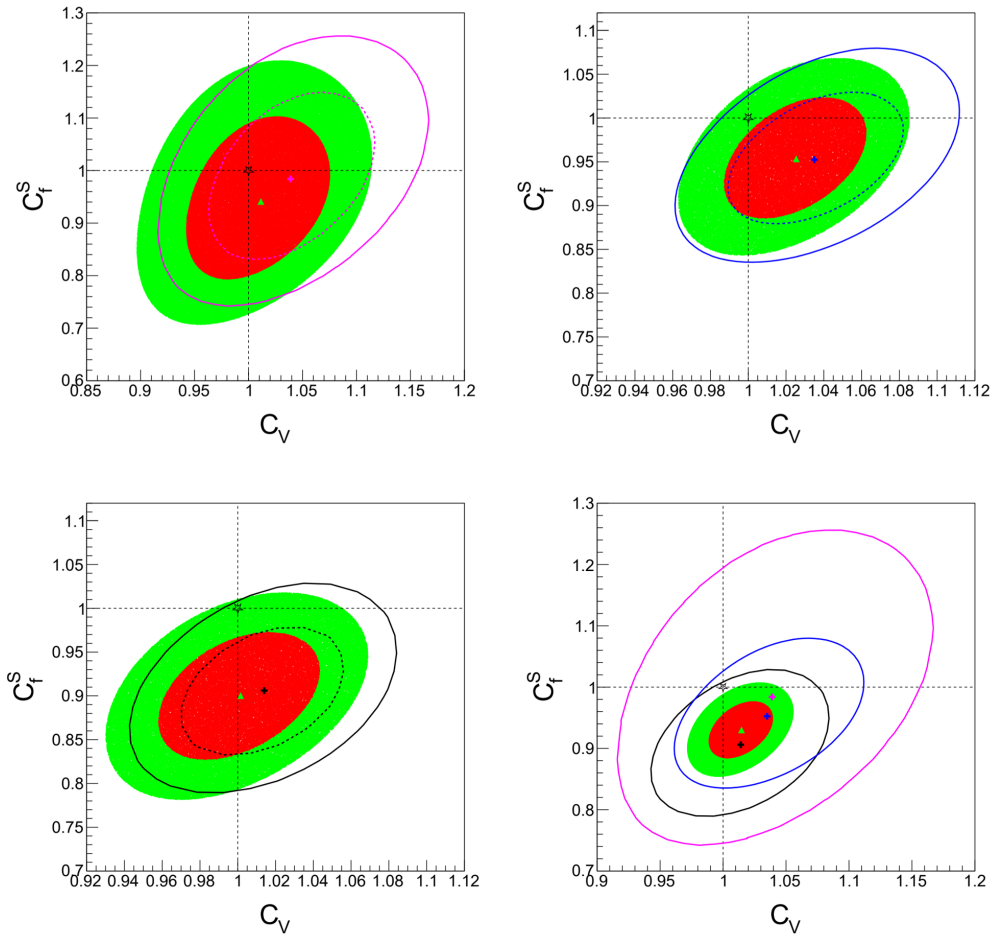


FIG. 1. The 68% (red) and 95% (green) CL regions in the (C_V, C_f^S) planes obtained using the ATLAS+CMS Run 1 (upper-left), ATLAS Run 2 (upper-right), and CMS Run 2 (lower-left) experimental signal strengths in Tables II, III, and IV, respectively, and the theoretical ones in subsection III B. The couplings of C_V and C_f^S are varied as in **CPC2-I**. Also shown are the dashed and solid ellipses enclosing the 68% and 95% CL regions, respectively, presented in Refs. [13] (upper-left), [3] (upper-right), and [4] (lower-left). In the lower-right frame, the CL regions obtained using the full LHC Run 1 and Run 2 data are shown together with the solid magenta, blue, and black ellipses for the 95% CL regions presented in Refs. [13], [3], and [4]. The colors and lines are the same in all the frames and the vertical and horizontal lines denote the SM values of $C_V = 1$ and $C_f^S = 1$ with the best-fit points denoted by triangles (colored regions) and pluses (ellipses). The SM points where $C_V = C_f^S = 1$ are denoted by stars.

- LUB: vary $\{C_V, C_u^S, C_d^S, C_\tau^S, C_\mu^S\}$ to address the case in which the lepton universality of the normalized Yukawa couplings to charged leptons is broken
- **CPC6**: in this fit, we consider the following scenario:
 - CSBLUB: vary $\{C_W, C_Z, C_u^S, C_d^S, C_\tau^S, C_\mu^S\}$ to address the most general case of the Higgs couplings to the SM particles involved under the constraint of $C_t^S = C_c^S = C_u^S$

We provide Table X to summarize all the **CPCn** fits together with their subfits. Note that we do not address the case in which the charm- and top-quark Yukawa couplings are different from each other in this work. If only C_c^S is fitted while all the other non-SM and SM parameters are fixed at their SM values, we have $|C_c^S| \lesssim 2$ at 95% CL.¹⁶ But, if other gauge-Higgs and Yukawa couplings are simultaneously varied taking $C_c^S \neq C_t^S$, fitting to the 76 signal strengths considered in this work does not lead to the bounded results for the couplings. From a search for the Higgs boson decaying into a pair of charm quarks, the ATLAS collaboration gives the observed (expected) constraints of $|C_c^S| < 8.5$ (12.4) at 95% CL and $|C_c^S/C_b^S| < 4.5$ at 95% CL (5.1 expected) [30]. The CMS collaboration gives the observed (expected) 95% CL value of $1.1 < |C_c^S| < 5.5$ ($|C_c^S| < 3.40$) [62].

Before presenting the results of the **CPCn** fits and their subfits and discussing details of them separately, we make comparisons of the 68% and 95% confidence-level (CL) regions presented in Refs. [13], [3], and [4] with those obtained by

¹⁶ See Appendix B.

using the LHC Run 1 and Run 2 experimental signal strengths taken in this work¹⁷ and the theoretical ones elaborated in subsection III B. To be specific, we have taken **CPC2-I** subfit in which the couplings C_V and C_f^S are varied and the ATLAS \oplus CMS Run 1, ATLAS Run 2, and CMS Run 2 CL regions are taken from Fig. 26 in Ref. [13], Fig. 4 in Ref. [3], and Fig. 3 in Ref. [4], respectively: see the regions inside the dashed (68%) and solid (95%) ellipses in the upper and lower-left frames of Fig. 1. The CL regions obtained in this work are colored in red (68%) and green (95%). We observe that the best-fit values for C_f^S agrees excellently for ATLAS Run 2 and CMS Run 2 while, for ATLAS \oplus CMS Run 1, our value is smaller by the amount of about 0.04 which corresponds to about 0.5- σ level. On the other hand, our best-fit values for C_V are nearer to the SM point and the differences are at the level below 0.7 σ (Run 1) and 0.5 σ (Run 2). The 1 σ errors agree well except C_V of ATLAS Run 2 for which we have obtained $C_V^{\text{this work}} = 1.025 \pm 0.025$ while $C_V^{\text{ATLAS}[3]} = 1.035 \pm 0.031$: the lower edges of the two 1 σ regions are around 1 while our upper edge reduces to the SM direction by the amount 0.016 which corresponds to about 0.5- σ level. From these critical comparisons, we conclude that our global fits to the Higgs signal strengths in Tables II, III, and IV using the theoretical signal strengths given in subsection III B remarkably reproduces the fitting results in Ref. [13] (Run 1) and Refs. [3, 4] (Run 2) within the 0.5- σ level. Further we have arrived at the conclusion that the combined results of our precision analysis of the full LHC Run 1 and Run 2 data should be reliable better than the 0.5- σ level since Run 2 data are now statistically dominant and our Run 2 results are more consistent with those in Refs. [3, 4]. Lastly, we present the fully combined results in the lower-right frame of Fig. 1: the 68% (red) and 95% (green) CL regions are obtained from the full LHC Run 1 and Run 2 data. For comparisons, we also show the 95% CL magenta, blue, and black solid ellipses from Refs. [13], [3], and [4], respectively, which are the same as in the upper-left, upper-right, and lower-left frames, respectively. From Run 1 to Run 2, we observe that C_V approaches to the SM value of 1 while C_f^S deviates from it, see the points marked by pluses in the lower-right frame. The combined results gives $C_V = 1.015 \pm 0.017$ and $C_f^S = 0.930 \pm 0.031$ and the SM point denoted by a star locates just outside of the 95% CL region. The deviation of C_f^S from its SM value of 1 has been noticed not only in Refs. [3, 4] but also in Ref. [63] and our combined analysis strengthens the observation by showing that its best-fitted value is more than 2 standard deviations below the SM prediction.

1. CPC1

We show the fitting results for the four subfits of **CPC1** and $\Delta\chi^2$ above each minimum in Table XI and Fig. 2, respectively. The p -values against the SM for compatibility with the SM hypothesis are high for IU and IH but they are only 8% (HC) and 1% (I).

In IU where we consider the case in which there exist light non-SM invisible and/or undetected particles and the 125

TABLE XI. **CPC1**: The best-fitted values in the four **CPC1** subfits. Also shown are the corresponding minimal chi-square per degree of freedom ($\chi_{\text{min}}^2/\text{dof}$), goodness of fit (gof), and p -value against the SM for compatibility with the SM hypothesis. For the SM, we obtain $\chi_{\text{SM}}^2/\text{dof} = 82.3480/76$ and $\text{gof} = 0.2895$.

Parameters		CPC1			
		IU	HC	IH	I
non-SM	$\Delta\Gamma_{\text{tot}}/\text{MeV}$	$-0.042_{-0.132}^{+0.142}$	0	0	0
	ΔS^γ	0	$-0.313_{-0.176}^{+0.176}$	0	0
	ΔS^g	0	0	0	0
SM	C_V	1	1	$C_{Vf} = 1.005_{-0.017}^{+0.017}$	1
	C_f^S				$C_f^S = 0.920_{-0.029}^{+0.029}$
$\chi_{\text{min}}^2/\text{dof}$		82.2540/75	79.2183/75	82.2568/75	75.0931/75
goodness of fit (gof)		0.2649	0.3474	0.2649	0.4753
p -value against the SM		0.7590	0.0769	0.7626	0.0071

¹⁷ Precisely, we mean the 76 signal strengths in Tables I, II, III, and IV.

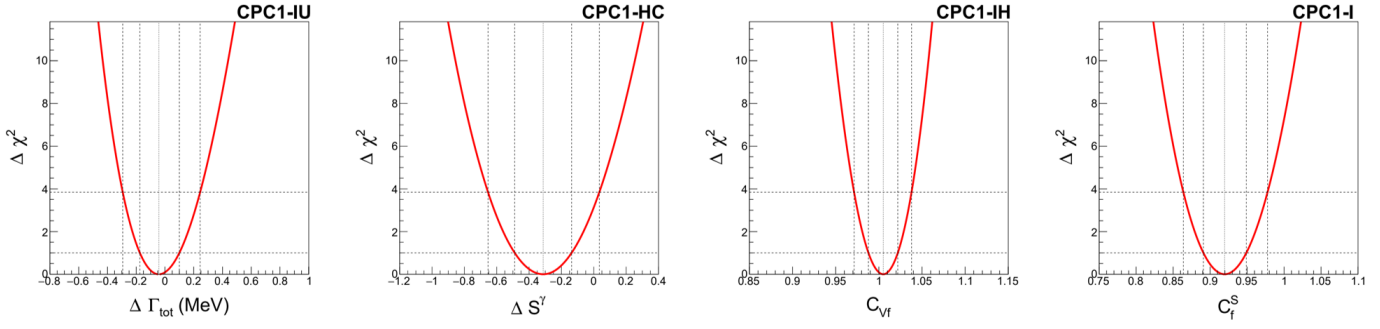


FIG. 2. **CPC1**: $\Delta\chi^2$ above the minimum versus $\Delta\Gamma_{\text{tot}}$ in MeV (left), ΔS^γ (middle-left), C_{Vf} (middle-right), and C_f^S (right) in the IU, HC, IH, and I subfits, respectively. The vertical and horizontal lines find the 1σ errors and 95% confidence intervals.

GeV Higgs boson H can decay into them, we obtain ¹⁸

$$\Delta\Gamma_{\text{tot}} = -0.042^{+0.142}_{-0.132} \text{ MeV}. \quad (33)$$

The central value is below zero by the amount of about 1% of the total SM Higgs decay width $\Gamma_{\text{tot}}(H_{\text{SM}}) = 4.059 - 4.128$ MeV in the range between $M_H = 125.0 - 125.5$ GeV. Considering the current theoretical and parametric uncertainties of $0.6 \sim 1\%$ [55] involved in the calculation of the total SM Higgs decay width around $M_H = 125$ GeV, we observe that it is consistent with zero. The gof value is 0.2649 which is a little bit worse than the SM (gof = 0.2895) as consistently indicated by chi-square per degree of freedom: $(\chi_{\text{min}}^2/\text{dof})^{\text{CPC1-IU}} = 82.2540/75 = 1.09672$ and $(\chi_{\text{SM}}^2/\text{dof})^{\text{SM}} = 82.3480/76 = 1.08353$. The 95% CL range is given by $\Delta\Gamma_{\text{tot}} = -0.042^{+0.287}_{-0.251}$ MeV, see the left frame of Fig. 2. Since the negative central value of $\Delta\Gamma_{\text{tot}}$ is unphysical, we take the upper error of 0.287 MeV as the conservative upper limit to obtain the following limit on the non-SM branching ratio at 95% CL:

$$B(H \rightarrow \text{non-SM}) < 7.1\%, \quad (34)$$

which is better than the combined 95% CL limit of either 10.7% (ATLAS: 7.7% expected) [64] or 15% (CMS: 8% expected) [65] observed in searches for decays of the Higgs boson to invisible particles.

In HC where the gauge-Higgs and Yukawa couplings of the Higgs boson are the same as in the SM while there exist heavy electrically charged non-SM particles which could modify the loop-induced Higgs couplings to two photons, we obtain

$$\Delta S^\gamma = -0.313 \pm 0.176, \quad (35)$$

which shows a 1.8σ deviation from the SM. This could be understood by observing that the combined decay signal strength of the $H \rightarrow \gamma\gamma$ mode is 1.10 ± 0.07 , see Table VI. Note that $S_{\text{SM}}^\gamma = -6.542 + 0.046i$ and $\Delta S^\gamma/S_{\text{SM}}^\gamma \simeq 0.048 \pm 0.027$. The gof value is 0.3474 which is definitely better than the SM. Incidentally, we obtain the following 95% CL region and limit:

$$-0.654 < \Delta S^\gamma < 0.034; \quad \left| \frac{\Delta S^\gamma}{S_{\text{SM}}^\gamma} \right| < 0.1, \quad (36)$$

see the middle-left frame of Fig. 2.

In IH where all the Higgs couplings to the SM particles scale with a single coupling $C_{Vf} = C_W = C_Z = C_t^S = C_c^S = C_b^S = C_\tau^S = C_\mu^S$, we obtain

$$C_{Vf} = 1.005 \pm 0.017. \quad (37)$$

The gof value is the same as in **CPC1-IU**. Actually, in **CPC1-IH** and **CPC1-IU**, all the production and decay processes scale with the overall single theoretical signal strength as follows:

$$\mu(\mathcal{P}, \mathcal{D})^{\text{CPC1-IH}} = C_{Vf}^2; \quad \mu(\mathcal{P}, \mathcal{D})^{\text{CPC1-IU}} = \frac{1}{1 + \Delta\Gamma_{\text{tot}}/\Gamma_{\text{tot}}(H_{\text{SM}})}. \quad (38)$$

¹⁸ Note that the asymmetric upper and lower 1σ errors indicate non-Gaussianity in the fitting results, as shown in the left frame of Fig. 2. For each one-parameter fit, we derive the 1σ errors and the 95% CL range from the $\Delta\chi^2 = 1$ and 3.84 lines, respectively, in the plot of $\Delta\chi^2$ distribution above the corresponding minimum, see Fig. 2. In fits with more than two parameters, even with non-Gaussianities, we derive the 68.27%, 95%, and 99.73% CL regions in two-parameter planes from the contours of $\Delta\chi^2 = 2.3$, 5.99, and 11.83, assuming Gaussian distributions, see Fig. 3 for example. Therefore, be cautious when interpreting our fitting results if non-Gaussianities are significant.

Accordingly, the best-fitted values are consistent with the global signal strength of $\mu_{76}^{\text{Global}} = 1.012 \pm 0.034$, see Eq. (6), which leads to the best-fit point deviated from the SM one by the amount of about +1% with about $\pm 3\%$ error in terms of signal strength.

In I where all the Yukawa couplings to the SM fermions scale with the same coupling parameter $C_f^S = C_u^S = C_d^S = C_\ell^S$ like as in type-I 2HDM but C_V is fixed at its SM value of 1, we obtain

$$C_f^S = 0.920 \pm 0.029. \quad (39)$$

Note that we have the highest gof value of 0.4753 which is larger than the **CPC2-IV** gof value of 0.4699 though slightly, see Table XII. We find that this simple one-parameter fit gives the best gof value among the **CPC** and **CPV** fits considered in this work, see Fig. 13.

2. CPC2

We show the fitting results for the eight subfits of **CPC2** in Table XII and depict their CL regions in Fig. 3. In HP, we perform the fit under the constraints of $\Delta\Gamma_{\text{tot}} \geq 0$ and $C_{Vf} = C_W = C_Z \leq 1$ and, only for this, we have the gof value worse than the SM. Otherwise, the gof values range between 0.3267 (IUHC) and 0.4699 (IV) which are indeed better than the SM. The p -values against the SM for compatibility with the SM hypothesis are only a few % for I, II, III, and IV.

In IUHC, we assume the simultaneous existence of the light non-SM particles into which the Higgs boson H decays and the heavy electrically charged non-SM particles contributing to $H \rightarrow \gamma\gamma$ through the triangle loops. The gof value is better than **CPC1-IU** but a little bit worse than **CPC1-HC**. Otherwise, the best-fitted values are similar to those in **CPC1** with a bit larger 1σ errors. The SM point lies outside the 68% CL region, see the upper-left frame of the left panel of Fig. 3.

In HCC, we assume the existence of the heavy electrically charged *and* colored non-SM particles contributing to ggF and $H \rightarrow \gamma\gamma$ through the triangle loops. The scalar form factor ΔS^γ deviates from the SM by 2σ similarly as in **CPC1-HC** and **CPC2-IUHC** while ΔS^g is consistent with the SM value of 0 within 1σ . The SM point lies outside of the 68% CL region, see the upper-right frame of the left panel of Fig. 3. The negative central value of -0.032 of ΔS^g decreases $|\Delta S^g/S_{\text{SM}}^g|$ by the amount of about 5% with $S_{\text{SM}}^g = 0.636 + 0.071i$ which contributes to the 1% increment of the global signal strength μ_{76}^{Global} since

$$\hat{\mu}(\mathcal{D} \neq \gamma\gamma, gg)^{\text{CPC2-HCC}} = \frac{\Gamma_{\text{tot}}(H_{\text{SM}})}{\Gamma_{\text{tot}}(H)} \simeq \frac{1}{0.92 + 0.08(1 + \Delta S^g/|S_{\text{SM}}^g|)^2}. \quad (40)$$

In CSB, C_W is 2σ above the SM with the 1σ error of 2%, while C_Z is consistent with the SM with the 1σ error of 3%. This is understood by comparing the WH production and $H \rightarrow WW^*$ decay signal strengths of $\mu(\text{WH}, \sum \mathcal{D}) = 1.20 \pm 0.15$ and $\mu(\sum \mathcal{P}, WW^*) = 1.04 \pm 0.07$ to ZH production and $H \rightarrow ZZ^*$ decay signal strengths of $\mu(\text{ZH}, \sum \mathcal{D}) = 1.03 \pm 0.14$

TABLE XII. **CPC2**: The best-fitted values in the eight **CPC2** subfits. Also shown are the corresponding minimal chi-square per degree of freedom ($\chi_{\text{min}}^2/\text{dof}$), goodness of fit (gof), and p -value against the SM for compatibility with the SM hypothesis. For the SM, we obtain $\chi_{\text{SM}}^2/\text{dof} = 82.3480/76$ and $\text{gof} = 0.2895$.

Parameters		CPC2							
		IUHC	HCC	CSB	I	II	III	IV	HP
non-SM	$\Delta\Gamma_{\text{tot}}/\text{MeV}$	$0.090^{+0.168}_{-0.157}$	0	0	0	0	0	0	$0.0^{+0.105}$
	ΔS^γ	$-0.369^{+0.202}_{-0.207}$	$-0.400^{+0.196}_{-0.196}$	0	0	0	0	0	0
	ΔS^g	0	$-0.032^{+0.031}_{-0.031}$	0	0	0	0	0	0
SM	C_V	1	1	$C_W = 1.038^{+0.018}_{-0.018}$	$1.015^{+0.017}_{-0.017}$	1	1	1	$C_{Vf} = 1.0_{-0.013}$
	C_f^S			1	$0.930^{+0.031}_{-0.031}$	$C_u^S = 0.931^{+0.032}_{-0.032}$	$C_{ud}^S = 0.919^{+0.037}_{-0.035}$	$C_{u\ell}^S = 0.920^{+0.029}_{-0.028}$	
$\chi_{\text{min}}^2/\text{dof}$		78.8971/74	78.1906/74	77.8970/74	74.3664/74	74.3154/74	75.0916/74	74.2510/74	82.3480/74
goodness of fit (gof)		0.3267	0.3473	0.3559	0.4662	0.4678	0.4427	0.4699	0.2369
p -value against the SM		0.1781	0.1252	0.1080	0.0185	0.0180	0.0266	0.0174	1.0

and $\mu(\sum \mathcal{P}, ZZ^*) = 0.97 \pm 0.08$, see Table VI. The SM point lies outside of the 68% CL region, see the lower-left frame of the left panel of Fig. 3.

In I, we assume all the Yukawa couplings to the SM particles are the same like as in type-I 2HDM but, compared to **CPC1-I**, C_V is also varied. We obtain that

$$C_V = 1.015 \pm 0.017; \quad C_f^S = 0.930 \pm 0.031. \quad (41)$$

While C_V is consistent with the SM with the 1σ error of about 2%, C_f^S deviates from the SM by the amount of more than 2σ resulting in that the SM point lies just outside of the 95% CL region, see the lower-right frame of the left panel of Fig. 3. We observe that this is a combined result of $\mu(\sum \mathcal{P}, \gamma\gamma) = 1.10 \pm 0.07$, $\mu(\sum \mathcal{P}, ZZ^*) = 0.97 \pm 0.08$, $\mu(\sum \mathcal{P}, WW^*) = 1.04 \pm 0.07$, $\mu(\sum \mathcal{P}, bb) = 0.90 \pm 0.12$, and $\mu(\sum \mathcal{P}, \tau\tau) = 0.87 \pm 0.08$, see Table VI. More precisely, we find that the central value 1.10 of $\mu(\sum \mathcal{P}, \gamma\gamma)$ correlates C_V and C_f^S as $C_f^S \sim 3C_V - 2.1$ ¹⁹ under which the Yukawa coupling C_f^S is driven to give the branching ratios 10% below the SM by $\mu(\sum \mathcal{P}, bb)$ and $\mu(\sum \mathcal{P}, \tau\tau)$ while the gauge coupling C_V near to the SM value of 1 by $\mu(\sum \mathcal{P}, ZZ^*)$ and $\mu(\sum \mathcal{P}, WW^*)$. Indeed, we find that

$$(C_V)^{H \rightarrow \gamma\gamma} = 1.038_{-0.039}^{+0.041}; \quad (C_f^S)^{H \rightarrow \gamma\gamma} = 0.999_{-0.098}^{+0.114}, \quad (42)$$

by fitting to the $\gamma\gamma$ signal strengths only and

$$(C_V)^{H \rightarrow ff} = 1.022_{-0.072}^{+0.078}; \quad (C_f^S)^{H \rightarrow ff} = 0.910_{-0.044}^{+0.042}, \quad (43)$$

by fitting to the fermionic signal strengths only. Incidentally, we obtain

$$(C_V)^{H \rightarrow \gamma\gamma, WW^*, ZZ^*} = 1.020 \pm 0.020; \quad (C_f^S)^{H \rightarrow \gamma\gamma, WW^*, ZZ^*} = 0.956_{-0.049}^{+0.052}, \quad (44)$$

by fitting to the bosonic signal strengths only.

In II, III, and IV, taking $C_V = 1$, we assume the Yukawa couplings to the SM particles behave like as in type-II,

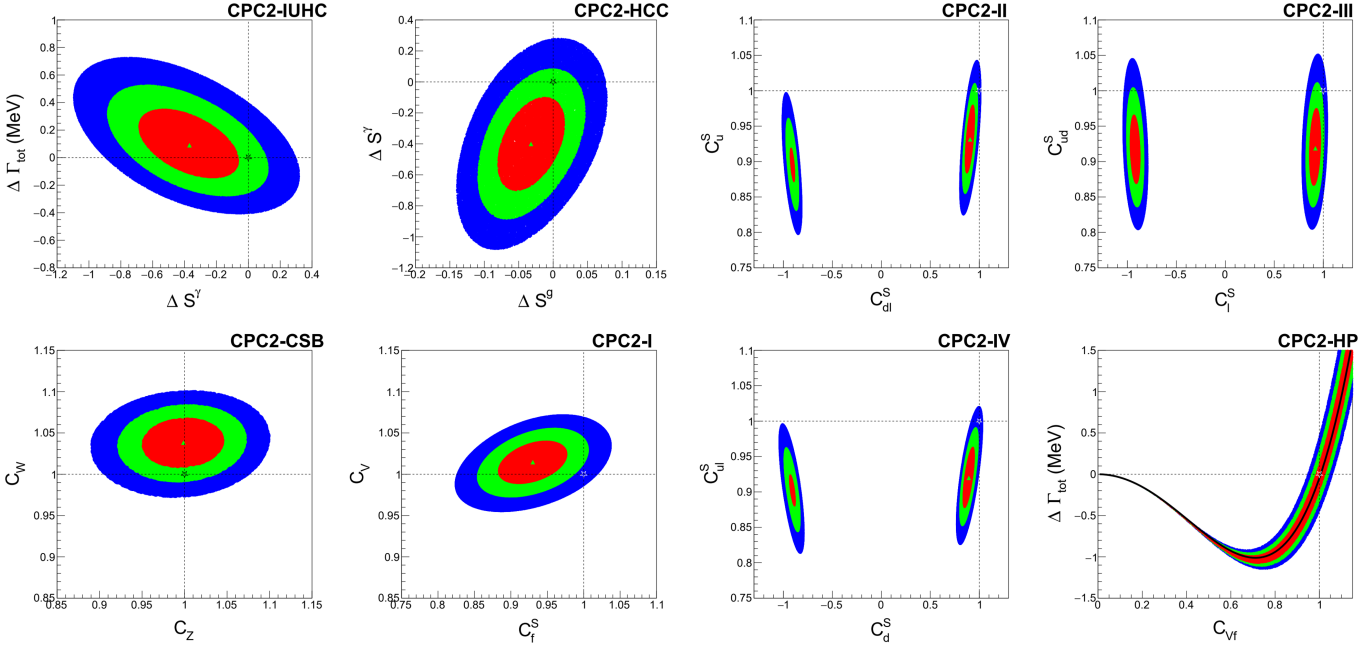


FIG. 3. **CPC2**: The CL regions of the eight **CPC2** subfits in two-parameter planes. The contour regions shown are for $\Delta\chi^2 \leq 2.3$ (red), $\Delta\chi^2 \leq 5.99$ (green), $\Delta\chi^2 \leq 11.83$ (blue) above the minimum, which correspond to confidence levels of 68.27%, 95%, and 99.73%, respectively. In each frame, the vertical and horizontal lines locate the SM point denoted by a star and the best-fit point is denoted by a triangle.

¹⁹ See Appendix C.

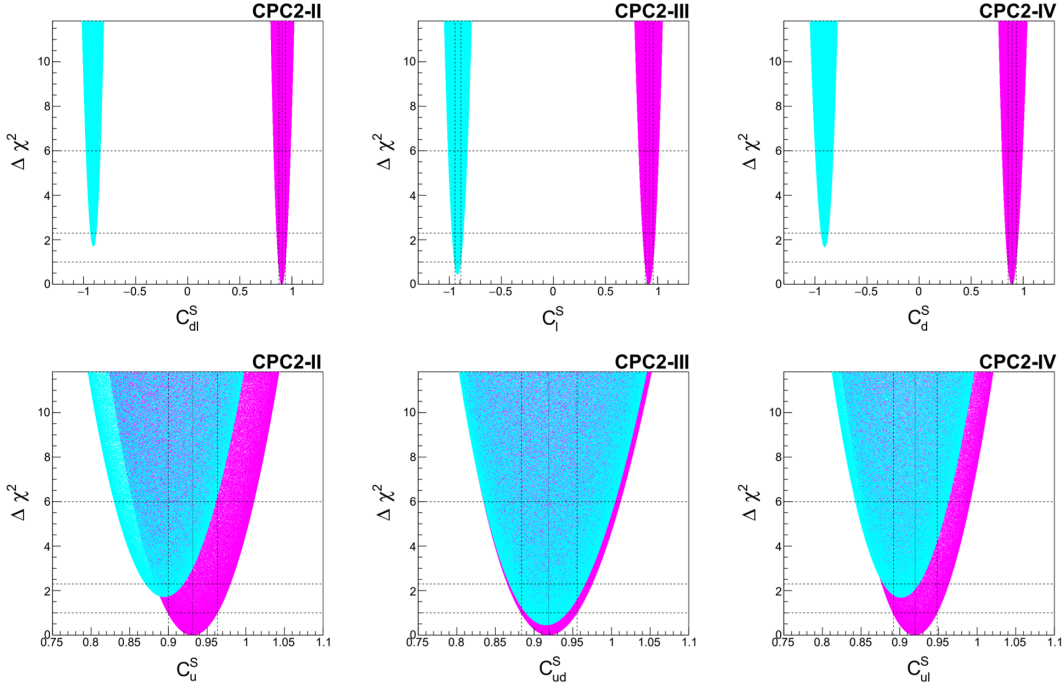


FIG. 4. **CPC2**: $\Delta\chi^2$ above the minimum versus Yukawa couplings in the II (left), III, (middle), and IV (right) subfits. The magenta (cyan) points are for the positive (negative) values of the Yukawa couplings of the down-type quarks and/or charged leptons. In each frame, the horizontal lines finds the 1σ errors and the 68.27% and 95% CL regions in two-parameter planes.

type-III, and type-IV 2HDMs, respectively. We obtain

$$\begin{aligned}
 (C_u^S)^{\text{II}} &= 0.931 \pm 0.032, & (C_{d\ell}^S)^{\text{II}} &= 0.907 \pm 0.032; \\
 (C_{ud}^S)^{\text{III}} &= 0.919_{-0.035}^{+0.037}, & (C_\ell^S)^{\text{III}} &= 0.921 \pm 0.038; \\
 (C_{u\ell}^S)^{\text{IV}} &= 0.920_{-0.028}^{+0.029}, & (C_d^S)^{\text{IV}} &= 0.894_{-0.039}^{+0.040}.
 \end{aligned} \tag{45}$$

We note that C_ℓ^S is basically determined by $\mu(\sum \mathcal{P}, \tau\tau) = 0.87 \pm 0.08$, see Table VI. Otherwise, all the Yukawa couplings deviate from the SM by the amount of more than 2σ like as in **CPC2-I** with the 1σ errors of 3%-4%. The SM point lies around the boundary between the 95% and 99.73% CL regions, see the upper-left (II), upper-right (III), and lower-left (IV) frames of the right panel of Fig. 3. We further note that all the best-fitted values are positive and the negative values of the Yukawa couplings $C_{d\ell}^S$, C_ℓ^S , and C_d^S around -1 are a bit less favored. In Fig. 4, we show $\Delta\chi^2$ above the positive minimum versus the down-type Yukawa couplings in the II (left), III, (middle), and IV (right) subfits. For $C_{d\ell}^S$, C_ℓ^S , and C_d^S , we observe that the data prefer the positive minima to the negative ones by $\Delta\chi^2 \sim 1.5$ ($C_{d\ell}^S$ and C_d^S) and $\Delta\chi^2 \sim 0.5$ (C_ℓ^S), see the upper frames of Fig. 4. This could be understood by observing that $\widehat{\mu}(\text{ggF} + \text{bbH})$ increases by the amount of about 10% by changing C_b^S from $+1$ to -1 , see Eq. (22) and Table VIII.²⁰ Similarly, $\widehat{\mu}(\gamma\gamma)$ is also sensitive to the sign of C_τ^S but the sign dependence is weaker due to the dominance of the W -boson loop contribution to S^γ , see Eq. (11). In fact, $\widehat{\mu}(\gamma\gamma)$ is powerful to reject the wrong sign of the top-quark Yukawa coupling and we see that negative C_t^S is completely ruled out, see the lower frames of Fig. 4.

In II, III, and IV, we scrutinize that the fitting results are consistent with the pattern of the Yukawa couplings predicted in each model. In type-II, type-III, and type-IV 2HDMs, the Yukawa couplings are correlated as follows:²¹

$$\begin{aligned}
 \text{II} : & \quad C_u^S = \cos \gamma - 1/\tan \beta \sin \gamma, & C_{d\ell}^S &= \cos \gamma + \tan \beta \sin \gamma, \\
 \text{III} : & \quad C_{ud}^S = \cos \gamma - 1/\tan \beta \sin \gamma, & C_\ell^S &= \cos \gamma + \tan \beta \sin \gamma, \\
 \text{IV} : & \quad C_{u\ell}^S = \cos \gamma - 1/\tan \beta \sin \gamma, & C_d^S &= \cos \gamma + \tan \beta \sin \gamma.
 \end{aligned} \tag{46}$$

²⁰ It is worthwhile to note that the increment of $\widehat{\mu}(\text{ggF} + \text{bbH})$ due to the sign flip amounts to about 30% if we consider ggF in LO. Considering ggF beyond LO, we lose a power to reject the negative bottom-quark Yukawa coupling.

²¹ Note again that we adopt the conventions and notations of 2HDMs as in Ref. [59].

TABLE XIII. **CPC3** and **CPC4**: The best-fitted values in the five **CPC3** and two **CPC4** subfits. Also shown are the corresponding minimal chi-square per degree of freedom (χ_{\min}^2/dof), goodness of fit (gof), and p -value against the SM for compatibility with the SM hypothesis. For the SM, we obtain $\chi_{\text{SM}}^2/\text{dof} = 82.3480/76$ and $\text{gof} = 0.2895$.

Parameters		CPC3					CPC4	
		IUHCC	II	III	IV	HP	A	HP
non-SM	$\Delta\Gamma_{\text{tot}}/\text{MeV}$	$-0.029^{+0.215}_{-0.191}$	0	0	0	$0.0^{+0.255}$	0	$0.0^{+0.186}$
	ΔS^γ	$-0.392^{+0.204}_{-0.206}$	0	0	0	$-0.366^{+0.197}_{-0.209}$	0	$-0.400^{+0.181}_{-0.200}$
	ΔS^g	$-0.036^{+0.042}_{-0.039}$	0	0	0	0	0	$-0.032^{+0.039}_{-0.030}$
SM	C_V	1	$1.007^{+0.026}_{-0.026}$	$1.015^{+0.017}_{-0.017}$	$1.004^{+0.034}_{-0.035}$	$C_{Vf} = 0.989^{+0.011}_{-0.019}$	$1.002^{+0.034}_{-0.035}$	$C_{Vf} = 1.0_{-0.021}$
	C_f^S		$C_u^S = 0.932^{+0.032}_{-0.032}$	$C_{ud}^S = 0.933^{+0.039}_{-0.039}$	$C_{ul}^S = 0.923^{+0.038}_{-0.037}$		$C_u^S = 0.927^{+0.040}_{-0.040}$	
			$C_{dl}^S = 0.917^{+0.048}_{-0.047}$	$C_\ell^S = 0.928^{+0.038}_{-0.039}$	$C_d^S = 0.902^{+0.084}_{-0.084}$		$C_d^S = 0.902^{+0.082}_{-0.081}$	
							$C_\ell^S = 0.916^{+0.047}_{-0.046}$	
χ_{\min}^2/dof	78.1707/73	74.2343/73	74.3554/73	74.2386/73	78.8928/73	74.1893/72	78.1906/72	
goodness of fit (gof)	0.3181	0.4377	0.4338	0.4376	0.2981	0.4067	0.2883	
p -value against the SM	0.2429	0.0437	0.0462	0.0438	0.3265	0.0859	0.3874	

Note that, in each model, only one of the two couplings could be larger or smaller than 1 depending on the sign of $\sin \gamma$ when $\cos \gamma = C_V \sim 1$. It is impossible to have both the couplings larger or smaller than 1 likes as in type-I 2HDM. In the upper-left (II), upper-right (III), and lower-left (IV) frames of the right panel of Fig. 3, we note that most of the 95% CL regions locate where both of the couplings are smaller than 1. The situation will be clearer in **CPC3** by varying C_V also and in **CPC4-A** by varying the Yukawa couplings of the up- and down-type quarks and the charged leptons separately.

In HP, all the production and decay processes scale with the overall single theoretical signal strength of:

$$\mu(\mathcal{P}, \mathcal{D})^{\text{CPC2-HP}} = \frac{C_{Vf}^4}{C_{Vf}^2 + \Delta\Gamma_{\text{tot}}/\Gamma_{\text{tot}}(H_{\text{SM}})}, \quad (47)$$

which leads to the relation

$$\frac{\Delta\Gamma_{\text{tot}}}{\Gamma_{\text{tot}}(H_{\text{SM}})} = C_{Vf}^2 \left(\frac{C_{Vf}^2}{\mu^{\text{Global}}} - 1 \right). \quad (48)$$

In the lower-right frame of the right panel of Fig. 3, the black line passing the origin $(\Delta\Gamma_{\text{tot}}, C_{Vf}) = (0, 0)$ and the SM point $(\Delta\Gamma_{\text{tot}}, C_{Vf}) = (0, 1)$ represents the above relation when $\mu^{\text{Global}} = 1$. In Higgs-portal models, the varying parameters are physically constrained by $\Delta\Gamma_{\text{tot}} \geq 0$ and $C_{Vf} \leq 1$. Imposing these conditions, we find the following best-fitted values

$$\Delta\Gamma_{\text{tot}}/\text{MeV} = 0.0^{+0.105}, \quad C_{Vf} = 1.0_{-0.013}. \quad (49)$$

We consider some extended HP scenarios in **CPC3** and **CPC4**.

3. CPC3 and CPC4

We show the fitting results for the five **CPC3** and two **CPC4** subfits in Table XIII. In the HP scenarios, we perform the fit under the constraints of $\Delta\Gamma_{\text{tot}} \geq 0$ and $C_{Vf} = C_W = C_Z \leq 1$ and we have the gof values similar to the SM. Otherwise, the gof values range between 0.3181 (**CPC3-IUHCC**) and 0.4377 (**CPC3-II**) which are better than the SM but slightly worse than the corresponding **CPC2** fits. The gof value of **CPC4-A** is also larger than 0.4. The CL regions in two-parameter planes are depicted in Fig. 5 and Fig. 6 for **CPC3** and **CPC4**, respectively. Note that, in the HP scenarios, we show the parameter spaces in which the fitting constraints of $\Delta\Gamma_{\text{tot}} \geq 0$ and $C_{Vf} \leq 1$ are fulfilled. The p -values against the SM for compatibility with the SM hypothesis are smaller than 10% except **CPC3-IUHCC**, **CPC3-HP**, and **CPC4-HP**.

In **CPC3-IUHCC**, we vary all the three non-SM parameters. The best-fitted values for $\Delta\Gamma_{\text{tot}}$ and ΔS^g are consistent with the SM within 1σ while ΔS^γ deviates from the SM by about 1.5σ . The 1σ errors are about 5% for $\Delta\Gamma_{\text{tot}}/\Gamma_{\text{tot}}(H_{\text{SM}})$, 3% for $|\Delta S^\gamma/S_{\text{SM}}^\gamma|$, and 6% for $|\Delta S^g/S_{\text{SM}}^g|$ which are slightly larger than those found in **CPC1-IU**, **CPC2-IUHC**, and

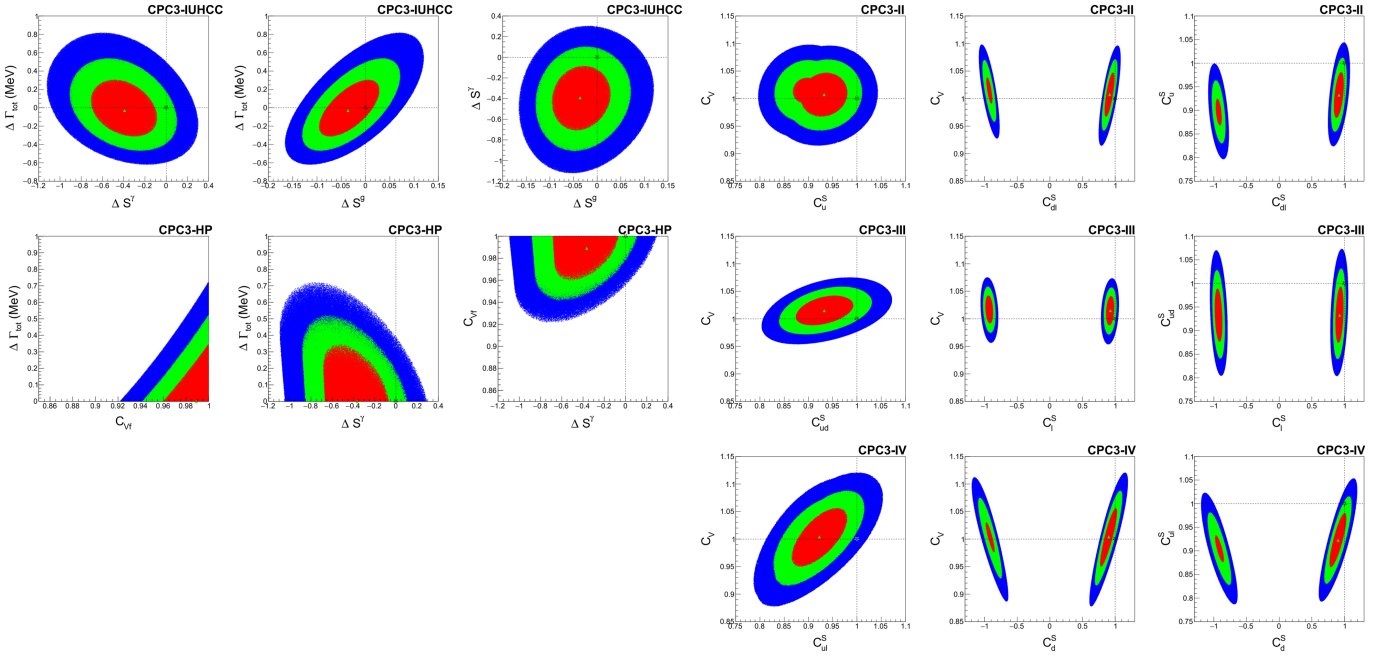


FIG. 5. **CPC3**: The CL regions of the five **CPC3** subfits in two-parameter planes: [Left] IUHCC (upper) and HP (middle) [Right] II (upper), III (middle), and IV (lower). The contour regions shown are for $\Delta\chi^2 \leq 2.3$ (red), $\Delta\chi^2 \leq 5.99$ (green), $\Delta\chi^2 \leq 11.83$ (blue) above the minimum, which correspond to confidence levels of 68.27%, 95%, and 99.73%, respectively. In each frame, the vertical and horizontal lines locate the SM point denoted by a star and the best-fit point is denoted by a triangle.

CPC2-HCC. The SM points lies outside of the 68% CL regions in the $(\Delta S^\gamma, \Delta\Gamma_{\text{tot}})$ and $(\Delta S^q, \Delta S^\gamma)$ planes, see the upper frames of the left panel of Fig. 5.

In II, III, IV subfits of **CPC3**, we additionally vary C_V compared to the corresponding **CPC2** subfits. We observe that C_V is consistent with SM within 1σ errors of about 2%-3%. In contrast, the Yukawa couplings are about 2σ below the SM except for C_d^S (IV). The 1σ errors of C_u^S (II), C_{ud}^S (III), and C_{ul}^S (IV) grouped with the up-type quarks are 3%-4% and those of C_{dl}^S (II), C_ℓ^S (III), and C_d^S (IV) for the down-type fermions 4-8%. The larger error of the down-type fermions could be understood from the positive correlations between C_V and the absolute values of them, see the upper-, middle-, and lower-middle frames of the right panel of Fig. 5. The stronger correlation leads to the the larger errors. We find that the minima for the negative values of C_{dl}^S (II), C_ℓ^S (III), and C_d^S (IV) are above the corresponding positive ones by the amount of $\Delta\chi^2 \sim 1.5$, ~ 0.3 , and ~ 1.7 , respectively. Incidentally, we observe that the distortion of the CL regions in

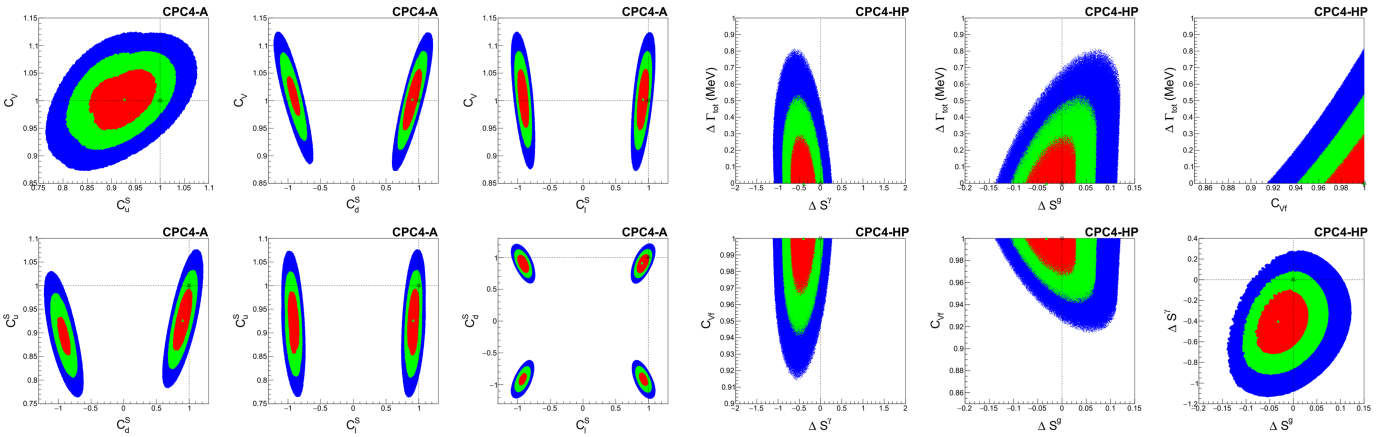


FIG. 6. **CPC4**: The CL regions of **CPC4-A** [Left] and **CPC4-HP** [Right] subfits in two-parameter planes: The contour regions shown are for $\Delta\chi^2 \leq 2.3$ (red), $\Delta\chi^2 \leq 5.99$ (green), $\Delta\chi^2 \leq 11.83$ (blue) above the minimum, which correspond to confidence levels of 68.27%, 95%, and 99.73%, respectively. In each frame, the vertical and horizontal lines locate the SM point denoted by a star and the best-fit point is denoted by a triangle.

TABLE XIV. **CPC5** and **CPC6**: The best-fitted values in the two **CPC5** and one **CPC6** subfits. Also shown are the corresponding minimal chi-square per degree of freedom (χ_{\min}^2/dof), goodness of fit (gof), and p -value against the SM for compatibility with the SM hypothesis. For the SM, we obtain $\chi_{\text{SM}}^2/\text{dof} = 82.3480/76$ and $\text{gof} = 0.2895$. Note that there are two degenerate minima for the positive and negative values of either C_ℓ^S (**CPC5-AHC**) or C_μ^S (**CPC5-LUB** and **CPC6-CSBLUB**).

Parameters		CPC5		CPC6
		AHC	LUB	CSBLUB
non-SM	$\Delta\Gamma_{\text{tot}}/\text{MeV}$	0	0	0
	ΔS^γ	$-0.102_{-0.212}^{+0.217}$ ($C_\ell^S > 0$), $-0.146_{-0.208}^{+0.219}$ ($C_\ell^S < 0$)	0	0
	ΔS^g	0	0	0
SM	C_V	$0.998_{-0.035}^{+0.034}$ ($C_\ell^S > 0$), $0.998_{-0.034}^{+0.035}$ ($C_\ell^S < 0$)	$1.003_{-0.030}^{+0.033}$	$C_W = 1.012_{-0.033}^{+0.033}$ $C_Z = 0.987_{-0.038}^{+0.037}$
	C_f^S	$C_u^S = 0.929_{-0.040}^{+0.041}$ ($C_\ell^S > 0$), $C_u^S = 0.929_{-0.038}^{+0.040}$ ($C_\ell^S < 0$)	$C_u^S = 0.925_{-0.035}^{+0.036}$	$C_u^S = 0.933_{-0.035}^{+0.035}$
		$C_d^S = 0.907_{-0.078}^{+0.079}$ ($C_\ell^S > 0$), $C_d^S = 0.907_{-0.082}^{+0.081}$ ($C_\ell^S < 0$)	$C_d^S = 0.902_{-0.076}^{+0.073}$	$C_d^S = 0.913_{-0.067}^{+0.066}$
	$C_\ell^S = 0.920_{-0.043}^{+0.046}$, $-0.920_{-0.046}^{+0.045}$	$C_\tau^S = 0.910_{-0.044}^{+0.042}$	$C_\tau^S = 0.915_{-0.039}^{+0.039}$	
		$C_\mu^S = \pm 1.057_{-0.151}^{+0.134}$	$C_\mu^S = \pm 1.061_{-0.131}^{+0.118}$	
χ_{\min}^2/dof		73.9870/71	73.4684/71	72.9828/70
goodness of fit (gof)		0.3809	0.3972	0.3803
p -value against the SM		0.1374	0.1140	0.1541

(C_u^S, C_V) (II) plane appearing the upper-left frame of the right panel of Fig. 5 is due to the minimum around $C_u^S = 0.9$ for the negative values of $C_{d\ell}^S$, see the upper-right frame of the same panel in the ($C_{d\ell}^S, C_u^S$) plane. Finally, we observe that the 68% CL regions locate where both of the Yukawa couplings are smaller than 1 indicating deviation from the conventional type-II, type-III, and type-IV 2HDMs, see the upper-, middle-, and lower-right frames of the right panel of Fig. 5.

In **CPC3-HP** where we add the non-SM contribution to $H \rightarrow \gamma\gamma$ compared to **CPC2-HP**, ΔS^γ is fitted to accommodate $\hat{\mu}(\gamma\gamma) = 1.1 \pm 0.07$ like as in **CPC1-HC**. The parameters $\Delta\Gamma_{\text{tot}}$ and C_{Vf} are fitted to have the SM values like as in **CPC2-HP** but with a bit larger 1σ errors under the constraints of $\Delta\Gamma_{\text{tot}} > 0$ and $C_{Vf} < 1$. In **CPC4-HP**, we further add the non-SM contribution also to $H \rightarrow gg$ assuming non-SM particles such as vector-like quarks. For ΔS^γ and ΔS^g , the fitting results are very similar to **CPC2-HCC** and the parameters $\Delta\Gamma_{\text{tot}}$ and C_{Vf} are again fitted to have the SM values under the constraints of $\Delta\Gamma_{\text{tot}} > 0$ and $C_{Vf} < 1$ like as in other HP scenarios. The SM points lie outside of the 68% CL regions in the ($\Delta\Gamma_{\text{tot}}, \Delta S^\gamma$), ($C_{Vf}, \Delta S^\gamma$), and ($\Delta S^g, \Delta S^\gamma$) planes, see the right panel of Fig. 6.

In **CPC4-A**, we vary the Yukawa couplings of the up- and down-type quarks and the charged leptons separately together with C_V . This scenario does not alter our previous observation made in **CPC3** for the Yukawa couplings: they are about 1σ (C_d^S) and 2σ (C_u^S and C_ℓ^S) below the SM. The C_V is very consistent with the SM with the 1σ error of about 3% and the 1σ errors of C_u^S , C_ℓ^S , and C_d^S are 4%, 5%, and 8%, respectively. And, from the CL regions in the (C_d^S, C_u^S), (C_ℓ^S, C_u^S), and (C_ℓ^S, C_d^S) planes shown in the lower frames of the left panel of Fig. 6, we see that the data favor the type-I 2HDM over the other three models. Incidentally, we find that the minima for the negative values of C_d^S and C_ℓ^S are above the positive ones by the amount of $\Delta\chi^2 \sim 1.5$ and ~ 0.3 , respectively.

4. CPC5 and CPC6

We show the fitting results for the two **CPC5** and one **CPC6** subfits in Table XIV. The gof values are 0.3809 (**CPC5-AHC**), 0.3972 (**CPC5-LUB**) and 0.3803 (**CPC6-CSBLUB**) which are better than the SM. The p -values against the SM for compatibility with the SM hypothesis are low and it is 15% for **CPC6-CSBLUB**. The CL regions in two-parameter planes are depicted in Fig. 7 and Fig. 8 for **CPC5** and **CPC6**, respectively.

In **CPC5-AHC**, compared to **CPC4-A**, we add the contribution to $H \rightarrow \gamma\gamma$ from heavy electrically charged particles. First of all, we find that the minima for the positive and negative values of C_ℓ^S are degenerate with the change of ΔS^γ by the amount of 0.044 compensating the effects of the flipped sign of C_ℓ^S , see Eq. (11). The parameter ΔS^γ is consistent with the SM: $\Delta S^\gamma/S_{\text{SM}}^\gamma \sim 0.016 \pm 0.03$ and 0.022 ± 0.03 for the positive and negative values of C_ℓ^S , respectively, and the two minima of ΔS^γ are very near to each other separated by only $\sim 0.2\sigma$. The gauge-Higgs coupling C_V and the Yukawa couplings of C_u^S , C_d^S , and $|C_\ell^S|$ are fitted similarly as in **CPC4-A**.²² The SM points are now near to or in the 68% CL regions, see the left panel of Fig. 7. We find that the negative minimum of C_d^S is above the positive one by the amount of $\Delta\chi^2 \sim 1.5$.

²² Note that, in **CPC5-AHC**, the best-fitted values of the fitting parameters at the two degenerate minima are almost the same except for ΔS^γ : the 1σ errors of C_V and $C_{u,d}^S$ depend on the sign of C_ℓ^S very weakly with their central values untouched, see Table XIV.

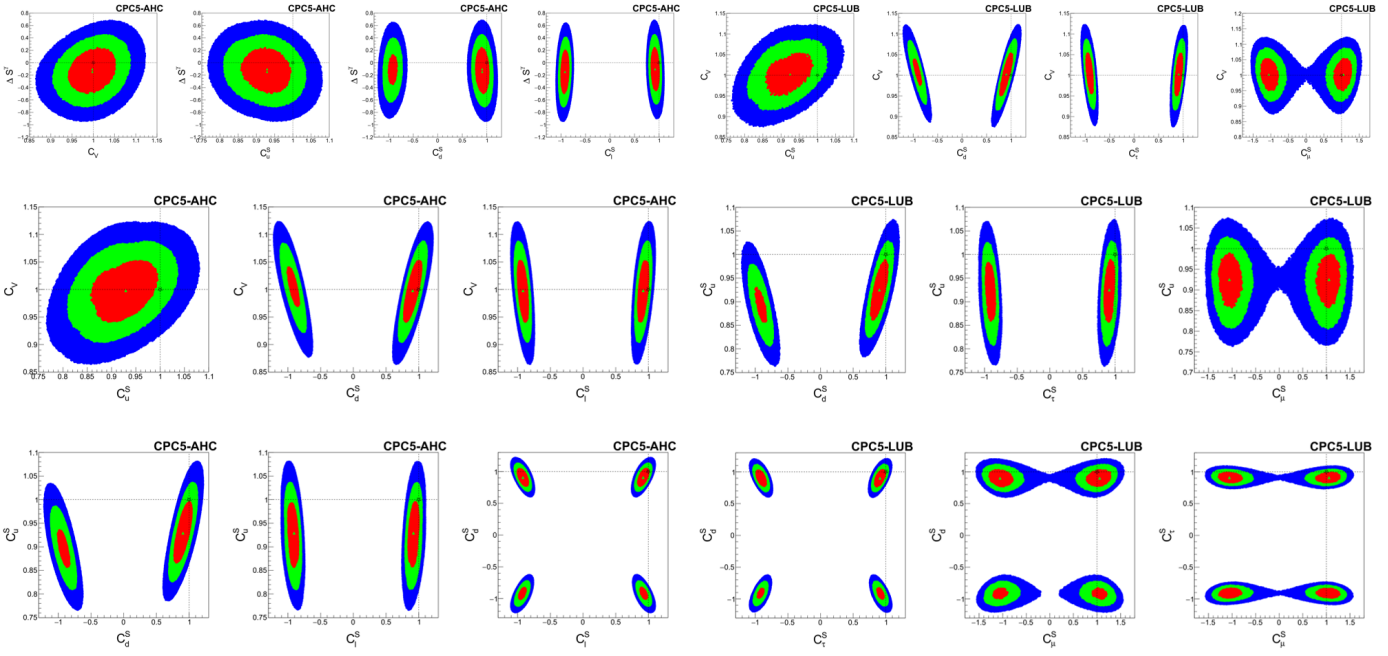


FIG. 7. **CPC5**: The CL regions of the two **CPC5** subfits in two-parameter planes: [Left] AHC [Right] LUB. The contour regions shown are for $\Delta\chi^2 \leq 2.3$ (red), $\Delta\chi^2 \leq 5.99$ (green), $\Delta\chi^2 \leq 11.83$ (blue) above the minimum, which correspond to confidence levels of 68.27%, 95%, and 99.73%, respectively. In each frame, the vertical and horizontal lines locate the SM point denoted by a star and the best-fit is denoted by a triangle.

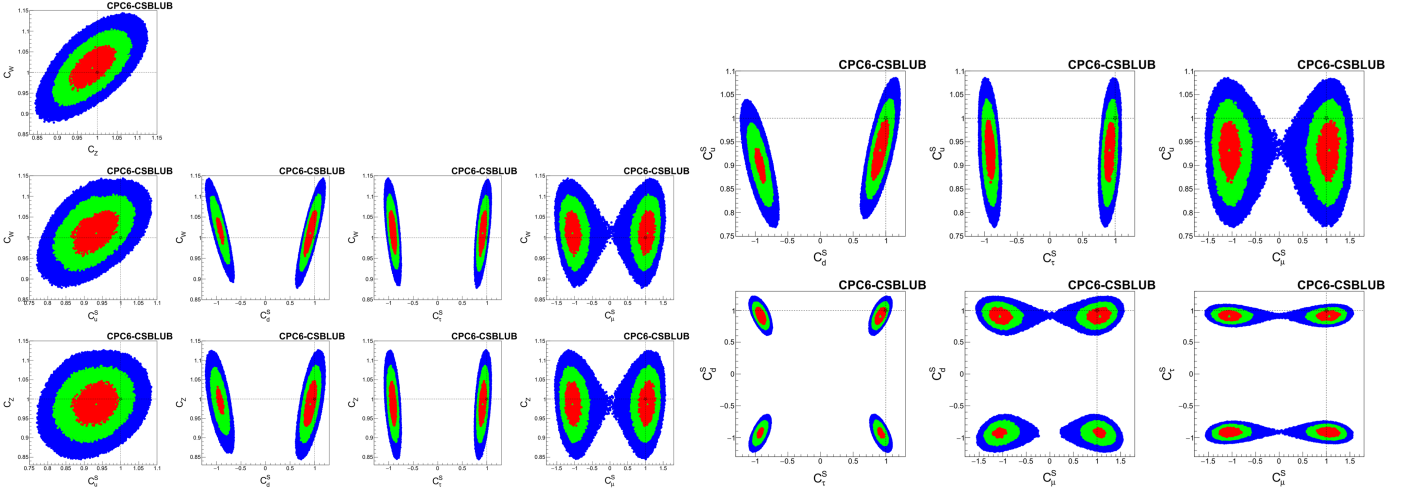


FIG. 8. **CPC6**: The CL regions of **CPC6-CSBLUB**. The contour regions shown are for $\Delta\chi^2 \leq 2.3$ (red), $\Delta\chi^2 \leq 5.99$ (green), $\Delta\chi^2 \leq 11.83$ (blue) above the minimum, which correspond to confidence levels of 68.27%, 95%, and 99.73%, respectively. In each frame, the vertical and horizontal lines locate the SM point denoted by a star and the best-fit point is denoted by a triangle.

In **CPC5-LUB**, compared to **CPC4-A**, we fit the tau-lepton- and muon-Yukawa couplings separately. We obtain that the gauge-Higgs coupling is consistent with the SM with the 1σ error of about 3% and the up-quark and tau-lepton Yukawa couplings are about 2σ below the SM with the 1σ errors of about 4%. The down-quark Yukawa coupling is about 1σ below the SM with the 1σ error of about 7%-8%. We find that the minima for the positive and negative values of C_μ^S are degenerate and, at the positive minimum, the muon-Yukawa coupling is consistent with the SM with the 1σ error of 13%-15%. The best-fitted values of the gauge-Higgs coupling C_V and the Yukawa couplings of $C_{u,d,\tau}^S$ are the same at the two degenerate minima. Around the SM values of $C_\tau^S = C_\mu^S = 1$, the 1σ regions of $(C_\tau^S)_{1\sigma} = [0.866, 0.952]$ and $(C_\mu^S)_{1\sigma} = [0.906, 1.191]$ overlap with no violation of lepton universality. We find that the negative minima of C_d^S and C_τ^S

TABLE XV. Varying parameters in the **CPV n** fits and their subfits considered in this work. The parameters not mentioned are supposed to take the SM value of either 0 or 1. For the total 17 CPV parameters, see Eq. (32).

	CPV2				CPV3					CPV4		CPV5	CPV7
	U	D	L	HC	U	D	L	F	IUHC	IUF	HCC	IUHCC	A
non-SM Parameters Varied				ΔS^γ ΔP^γ					$\Delta\Gamma_{\text{tot}}$ ΔS^γ ΔP^γ	$\Delta\Gamma_{\text{tot}}$	ΔS^γ ΔP^γ ΔS^g ΔP^g	$\Delta\Gamma_{\text{tot}}$ ΔS^γ ΔP^γ ΔS^g ΔP^g	
SM Parameters Varied	C_u^S C_u^P	C_d^S C_d^P	C_ℓ^S C_ℓ^P		C_V C_u^S C_u^P	C_V C_d^S C_d^P	C_V C_ℓ^S C_ℓ^P	C_V C_f^S C_f^P		C_V C_f^S C_f^P			C_V C_u^S C_u^P C_d^S C_d^P C_ℓ^S C_ℓ^P

are above the positive ones by the amount of $\Delta\chi^2 \sim 1.5$ and ~ 0.2 , respectively. The negative and positive regions of C_μ^S are connected at 99.73% CL, see the right panel of Fig. 7.

In **CPC6-CSBLUB**, we vary the six SM parameters independently under the constraint of $C_t^S = C_c^S = C_u^S$ and we find that the gauge-Higgs couplings are consistent with the SM with the 1σ errors of about 3%-4%. The central value of C_W (C_Z) is slight above (below) the SM value of 1. The up-quark and tau-lepton Yukawa couplings are about 2σ below the SM with the 1σ errors of about 4%. The down-quark Yukawa coupling is about 1σ below the SM with the 1σ error of about 7%. We find that the minima for the positive and negative values of C_μ^S are degenerate and, at the positive minimum, the muon Yukawa coupling is consistent with the SM with the 1σ error of about 13%. The best-fitted values of the gauge-Higgs couplings $C_{W,Z}$ and the Yukawa couplings of $C_{u,d,\tau}^S$ are the same at the two degenerate minima. We observe that, around the SM values of $C_\tau^S = C_\mu^S = 1$, the 1σ regions of the normalized couplings of $(C_\tau^S)_{1\sigma} = [0.876, 0.954]$ and $(C_\mu^S)_{1\sigma} = [0.930, 1.179]$ marginally overlap with no violation of lepton universality. Comparing the CL regions shown in the left (right) panel of Fig. 8 with those in the upper (middle and lower) frames of the right panel of Fig. 7, we observe that the CL regions **CPC6-CSBLUB** are very similar to those of **CPC5-LUB**.

Before moving to **CPV**, we provide the following brief summary for the SM parameters obtained from **CPC3**, **CPC4**, **CPC5**, and **CPC6** fits:²³

- C_V, C_W, C_Z : consistent with the SM with the 1σ error of 2%-3%
- $C_u^S, C_{ud}^S, C_{u\ell}^S$: about 2σ below the SM with the 1σ error of 3%-4%
- $C_{d\ell}^S, C_\ell^S, C_\tau^S$: about 2σ below the SM with the 1σ error of 4%-5%
- C_d^S : about 1σ below the SM with the 1σ error of 7%-8%
- $|C_\mu^S|$: consistent with the SM with the 1σ error of 12-15%

We further note that the BSM models predicting the same normalized Yukawa couplings to the up- and down-type quarks and charged leptons are preferred.

B. CP-violating fits

We generically label the CPV fits as **CPV n** with n standing for the number of fitting parameters like as in the CPC fits. Since there are 17 parameters to fit most generally, it is more challenging to exhaust all the possibilities than in the

²³ For correlations among the fitting parameters in **CPC2**, **CPC3**, and **CPC4**, see Appendix D.

CPC fits. Noting that CP violation is signaled by the simultaneous existence of the Higgs couplings to the scalar and pseudoscalar fermion bilinears,²⁴ we consider the following CPV fits in this work:

- **CPV2**: in this fit, we consider the four subfits as follows:
 - U: vary $\{C_u^S, C_u^P\}$ for the case in which CP violation resides in the up-type quark sector
 - D: vary $\{C_d^S, C_d^P\}$ for the case in which CP violation resides in the down-type quark sector
 - L: vary $\{C_\ell^S, C_\ell^P\}$ for the case in which CP violation resides in the charged-lepton sector
 - HC: vary $\{\Delta S^\gamma, \Delta P^\gamma\}$ for the case in which CP violation occurs due to heavy electrically charged non-SM fermions coupling to the Higgs boson
- **CPV3**: in this fit, we consider the five subfits as follows:
 - U: vary $\{C_V, C_u^S, C_u^P\}$ for the up-quark sector CP violation
 - D: vary $\{C_V, C_d^S, C_d^P\}$ for the down-quark sector CP violation
 - L: vary $\{C_V, C_\ell^S, C_\ell^P\}$ for the charged-lepton sector CP violation
 - F: vary $\{C_V, C_f^S, C_f^P\}$ assuming the universal normalized CPV couplings to the SM quarks and charged leptons
 - IUHC: vary $\{\Delta\Gamma_{\text{tot}}, \Delta S^\gamma, \Delta P^\gamma\}$ for the case in which CP violation occurs due to the H couplings to heavy electrically charged non-SM fermions in the presence of light non-SM particles into which H could decay
- **CPV4**: in this fit, we consider the following two subfits:
 - IUF: vary $\{\Delta\Gamma_{\text{tot}}, C_V, C_f^S, C_f^P\}$ assuming the universal normalized CPV couplings to the SM fermions in the presence of light non-SM particles into which H could decay
 - HCC: vary $\{\Delta S^\gamma, \Delta P^\gamma, \Delta S^g, \Delta P^g\}$ for the case in which CP violation occurs due to the H couplings to heavy electrically charged *and* colored non-SM fermions
- **CPV5**: in this fit, we consider the following scenario:
 - IUHCC: vary $\{\Delta\Gamma_{\text{tot}}, \Delta S^\gamma, \Delta P^\gamma, \Delta S^g, \Delta P^g\}$ for the case in which CP violation occurs due to the H couplings to heavy electrically charged *and* colored non-SM fermions in the presence of light non-SM particles into which H could decay
- **CPV7**: in this fit, we consider the following scenario:
 - A: vary $\{C_V, C_u^S, C_u^P, C_d^S, C_d^P, C_\ell^S, C_\ell^P\}$ with the H couplings to the SM particles like as in CPV A2HDM

We provide Table XV for the summary of the CPV fits considered in this work which explicitly shows the parameters varied in each subfit of **CPVn**.

Since the signal strengths are CP-even quantities, they do not contain CPV products such as $C_{u,d,\ell,f}^S \times C_{u,d,\ell,f}^P$ and $S^{\gamma,g} \times P^{\gamma,g}$. Therefore, the CL regions appear as a circle or an ellipse or some overlapping of them in the $(C_{u,d,\ell,f}^S, C_{u,d,\ell,f}^P)$ and $(\Delta S^{\gamma,g}, \Delta P^{\gamma,g})$ planes.

1. CPV2 and CPV3

We show the fitting results for the four **CPV2** and five **CPV3** subfits in Table XVI. We have the largest gof value for **CPV3-F** and note that the p -values against the SM for compatibility with the SM hypothesis are high in **CPV2-U** and **CPV2-D** with $\chi_{\text{min}}^2 \sim \chi_{\text{SM}}^2$. In the left panel of Fig. 9, the CL regions are depicted in the $(C_{u,d,\ell,f}^S, C_{u,d,\ell,f}^P)$ and $(\Delta S^\gamma, \Delta P^\gamma)$ planes for **CPV2** and **CPV3**. The other **CPV3** CL regions in the $(C_{u,d,\ell,f}^{S,P}, C_V)$, $(\Delta S^\gamma, \Delta\Gamma_{\text{tot}})$, and $(\Delta P^\gamma, \Delta\Gamma_{\text{tot}})$ planes are shown in the right panel of Fig. 9.

In **CPV2-U**, we obtain the sickle-shaped CL region in the (C_u^S, C_u^P) plane, see the upper-left frame of the left panel of Fig. 9. This could be understood by observing that the top-Yukawa couplings are involved in the ggF+bbH and

²⁴ We suppose that the contributions from the triangle loops in which non-SM heavy charged and/or colored fermions are running result in the coexistence of the scalar and pseudoscalar form factors of $\Delta S^{\gamma,g}$ and $\Delta P^{\gamma,g}$ when the Higgs boson simultaneously couples to the scalar and pseudoscalar bilinears of the non-SM fermions.

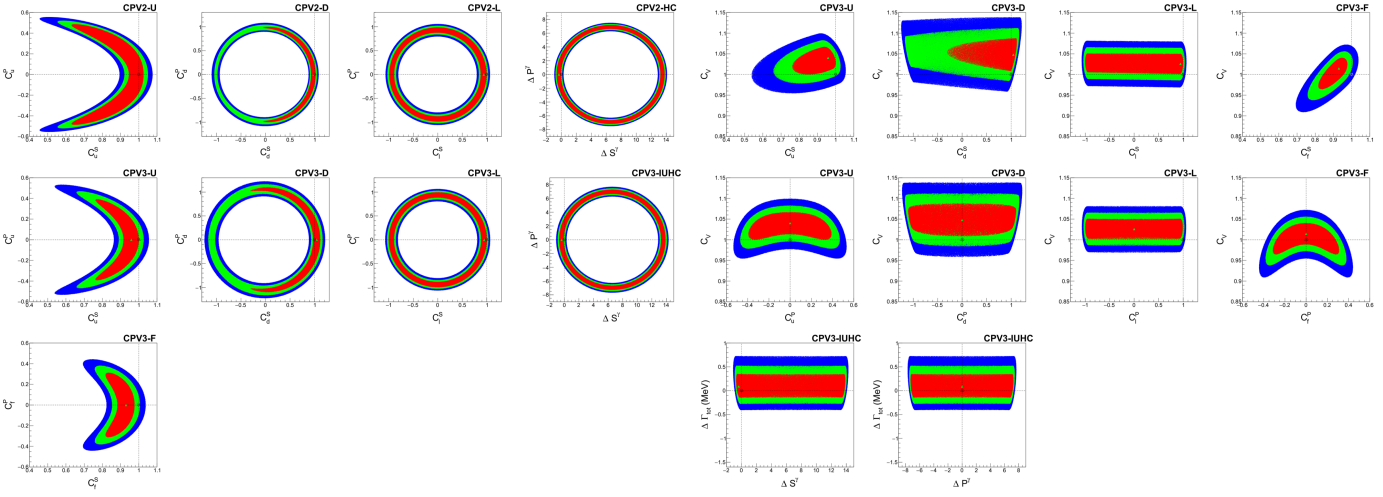


FIG. 9. **CPV2** and **CPV3**: [Left] The CL regions of the four **CPV2** (upper) and five **CPV3** (middle and lower) subfits in the $(C_{u,d,\ell,f}^S, C_{u,d,\ell,f}^P)$ and $(\Delta S^\gamma, \Delta P^\gamma)$ planes. [Right] The CL regions of the five **CPV3** subfits in the $(C_{u,d,\ell,f}^S, C_V)$ (upper), $(C_{u,d,\ell,f}^P, C_V)$ (middle), $(\Delta S^\gamma, \Delta \Gamma_{\text{tot}})$, and $(\Delta P^\gamma, \Delta \Gamma_{\text{tot}})$ (lower) planes. The contour regions shown are for $\Delta\chi^2 \leq 2.3$ (red), $\Delta\chi^2 \leq 11.83$ (blue) above the minimum, which correspond to confidence levels of 68.27%, 95%, and 99.73%, respectively. In each frame, the vertical and horizontal lines locate the SM point denoted by a star and the best-fit point is denoted by a triangle.

ttH \oplus tH production processes and the $H \rightarrow \gamma\gamma$ decay mode. From Eq. (22) with the Run 2 decomposition coefficients in Table VIII, Eq. (11) with $S_{\text{SM}}^\gamma = -6.542 + 0.046i$, and Eq. (24), we have

$$\begin{aligned} \hat{\mu}(\text{ggF} + \text{bbH})^{\text{CPV2-U}} &\simeq [1.04(C_u^S)^2 - 0.06C_u^S + 0.02] + 2.2(C_u^P)^2 \simeq 1.04(C_u^S - 0.03)^2 + 2.2(C_u^P)^2 + 0.02, \\ \hat{\mu}(\gamma\gamma)^{\text{CPV2-U}} &\simeq (-1.28 + 0.28C_u^S)^2 + 1.016(0.42C_u^P)^2, \\ \hat{\mu}(\text{ttH} \oplus \text{tH})^{\text{CPV2-U}} &\simeq 1.3[(C_u^S)^2 + (C_u^P)^2] - 0.8C_u^S + 0.5 \simeq 1.3[(C_u^S - 0.31)^2 + (C_u^P)^2] + 0.38, \end{aligned} \quad (50)$$

where the factor 1.016 in the second line for $\hat{\mu}(\gamma\gamma)$ takes account of the difference in the QCD and electroweak corrections to the scalar and pseudoscalar parts [47]. Note that $\hat{\mu}(\text{ggF} + \text{bbH}) \simeq 1$ gives an ellipse centered at $(C_u^S, C_u^P) \simeq (0, 0)$ with the lengths of the major (C_u^S) and minor (C_u^P) axes of 1 and 0.67 while $\hat{\mu}(\gamma\gamma) \simeq 1$ an ellipse centered at $(C_u^S, C_u^P) \simeq (4.6, 0)$ with the lengths of the major (C_u^S) and minor (C_u^P) axes of 3.6 and 2.4. In addition, $\hat{\mu}(\text{ttH} \oplus \text{tH}) \simeq 1$ gives a circle centered at $(C_u^S, C_u^P) \simeq (0.3, 0)$ with a radius of about 0.7. Both the ellipses and the circle pass the SM point of $(C_u^S, C_u^P) = (1, 0)$ as they should with the ggF+bbH ellipse and the ttH \oplus tH circle extending to the negative C_u^S direction from the SM point and the $\gamma\gamma$ ellipse to the positive C_u^S direction. The overlapping of the two ellipses and a circle with some corresponding

TABLE XVI. **CPV2** and **CPV3**: The best-fitted values in the four **CPV2** and five **CPV3** subfits. Also shown are the corresponding minimal chi-square per degree of freedom ($\chi_{\text{min}}^2/\text{dof}$), goodness of fit (gof), and p -value against the SM for compatibility with the SM hypothesis. For the SM, we obtain $\chi_{\text{SM}}^2/\text{dof} = 82.3480/76$ and $\text{gof} = 0.2895$.

	CPV2				CPV3				
	U	D	L	HC	U	D	L	F	IUHC
non-SM Parameters				$\Delta S^\gamma = -0.313^{+14.00}_{-0.175}$					$\Delta \Gamma_{\text{tot}}/\text{MeV} = 0.090^{+0.168}_{-0.157}$
Varied				$\Delta P^\gamma = 0.0^{+7.075}_{-7.074}$					$\Delta S^\gamma = -0.369^{+14.14}_{-0.207}$
SM Parameters	$C_u^S = 0.987^{+0.026}_{-0.322}$	$C_d^S = 0.978^{+0.029}_{-0.482}$	$C_\ell^S = 0.939^{+0.038}_{-1.893}$		$C_u^S = 1.040^{+0.018}_{-0.029}$	$C_u^S = 0.950^{+0.028}_{-0.143}$	$C_u^S = 1.045^{+0.048}_{-0.671}$	$C_u^S = 1.015^{+0.017}_{-0.036}$	$C_u^S = 1.015^{+0.017}_{-0.036}$
Varied	$C_u^P = 0.0^{+0.469}_{-0.469}$	$C_d^P = 0.0^{+0.845}_{-0.844}$	$C_\ell^P = 0.0^{+0.964}_{-0.964}$		$C_u^P = 0.0^{+0.341}_{-0.341}$	$C_u^P = 0.0^{+0.341}_{-0.341}$	$C_d^P = 0.0^{+0.986}_{-0.989}$	$C_f^P = 0.930^{+0.031}_{-0.081}$	$C_f^P = 0.0^{+0.267}_{-0.268}$
$\chi_{\text{min}}^2/\text{dof}$	82.1034/74	81.7649/74	79.7168/74	79.2183/74	77.1617/73	78.4013/73	77.2007/73	74.3664/73	78.8971/73
goodness of fit (gof)	0.2427	0.2509	0.3040	0.3178	0.3471	0.3116	0.3460	0.4335	0.2979
p -value against the SM	0.8849	0.7470	0.2683	0.2091	0.1587	0.2673	0.1613	0.0464	0.3272

errors explain the sickle-shaped CL region in the (C_u^S, C_u^P) plane which also appears in **CPV3-U** and **CPV3-F**, see the middle-left and lower-left frames of the left panel of Fig. 9. We observe that the SM point lies outside the 68% CL region in **CPV3-F** with $C_f^S = 0.930_{-0.081}^{+0.031}$ which deviates from the SM point more than C_u^S in **CPC2-U** and **CPC3-U** with the smaller negative error.

The circles in the (C_d^S, C_d^P) planes for **CPV2-D** and **CPV3-D** shown in the two middle-left frames of the left panel of Fig. 9 are understood by noting that the signal strength of the bb decay mode is given by

$$\widehat{\mu}(bb)^{\text{CPV3-D}} \simeq \frac{(C_d^S)^2 + (C_d^P)^2}{0.57[(C_d^S)^2 + (C_d^P)^2] + 0.25C_V^2 + 0.18}. \quad (51)$$

The positive values of C_d^S are preferred because of the interferences between the top- and bottom-quark contributions to ggF. We note that $\Delta\chi^2$ above the minimum at $(C_d^S, C_d^P) \simeq (1, 0)$ increases by the amount of about 5 while C_d^S changes from +1 to -1. When C_d^P changes from +1 to -1, $\Delta\chi^2$ above the minimum increases by the amount smaller than 2.

The circles in the (C_ℓ^S, C_ℓ^P) planes for **CPV2-L** and **CPV3-L** shown in the two middle-right frames of the left panel of Fig. 9 are understood by noting that the signal strength of the $\tau\tau$ and $\mu\mu$ decay modes is given by $\widehat{\mu}(\tau\tau) \simeq \widehat{\mu}(\mu\mu) \simeq (C_\ell^S)^2 + (C_\ell^P)^2$. We note that $\Delta\chi^2$ above the minimum $(C_\ell^S, C_\ell^P) \simeq (0.94, 0)$ increases by the amount less than 1 while $C_\ell^{S,P}$ changes from +1 to -1. We note that the charged-lepton circles are smaller than the down-type-quark circles.

The circles in the $(\Delta S^\gamma, \Delta P^\gamma)$ planes for **CPV2-HC** and **CPV3-IUHC** shown in the two right frames of the left panel of Fig. 9 are understood by noting that $\widehat{\mu}(\gamma\gamma) = 1$ gives a circle centered at $(\Delta S^\gamma, \Delta P^\gamma) \simeq (6.5, 0)$ with the radius of about 6.5 with the signal strength of the $H \rightarrow \gamma\gamma$ decay mode given by

$$\widehat{\mu}(\gamma\gamma)^{\text{CPV2-HC}} \simeq \left(-1 + \frac{\Delta S^\gamma}{|S_{\text{SM}}^\gamma} \right)^2 + \left(\frac{\Delta P^\gamma}{|S_{\text{SM}}^\gamma} \right)^2. \quad (52)$$

From the ten frames of the right panel of Fig. 9, we observe that the most of the SM points are outside of the 68% CL regions except **CPV3-F** in the (C_f^P, C_V) plane (middle-right) and **CPV3-IUHC** (lower). There are almost no correlations between C_V and $C_\ell^{S,P}$ (upper-middle-right and middle-middle-right) and the correlation between C_V and C_d^P in **CPV3-D** (middle-middle-left) is weakly correlated. We also see almost no correlations between $\Delta\Gamma_{\text{tot}}$ and ΔS^γ (lower-left) and $\Delta\Gamma_{\text{tot}}$ and ΔP^γ (lower-middle) in **CPV3-IUHC**.

2. CPV4, CPV5, and CPV7

We show the fitting results for **CPV4**, **CPV5**, and **CPV7** in Table XVII. Note that, in **CPV4-IUF**, the parameters are not bounded like as in the HP scenarios and we implement the fit under the constraints of $\Delta\Gamma_{\text{tot}} \geq 0$ and $C_V \leq 1$.

TABLE XVII. **CPV4, CPV5, and CPV7**: The best-fitted values in the **CPV4, CPV5, and CPV7** fits. Also shown are the corresponding minimal chi-square per degree of freedom ($\chi_{\text{min}}^2/\text{dof}$), goodness of fit (gof), and p-value against the SM for compatibility with the SM hypothesis. For the SM, we obtain $\chi_{\text{SM}}^2/\text{dof} = 82.3480/76$ and $\text{gof} = 0.2895$.

	CPV4		CPV5	CPV7
	IUF	HCC	IUHCC	A
non-SM	$\Delta\Gamma_{\text{tot}} = 0.0^{+0.155}$		$\Delta\Gamma_{\text{tot}} = -0.029_{-0.491}^{+0.211}$	
Parameters		$\Delta S^\gamma = -0.400_{-0.208}^{+14.21}$	$\Delta S^\gamma = -0.392_{-0.213}^{+14.17}$	
Varied		$\Delta P^\gamma = 0.0_{-7.183}^{+7.190}$	$\Delta P^\gamma = 0.0_{-7.176}^{+7.178}$	
		$\Delta S^g = -0.032_{-0.257}^{+0.031}$	$\Delta S^g = -0.036_{-0.609}^{+0.041}$	
		$\Delta P^g = 0.0_{-0.745}^{+0.743}$	$\Delta P^g = 0.0_{-0.988}^{+0.987}$	
SM	$C_V = 1.0_{-0.020}$			$C_V = 1.002_{-0.034}^{+0.034}$
Parameters	$C_f^S = 0.900_{-0.050}^{+0.035}$			$C_u^S = 0.927_{-0.106}^{+0.037}$
Varied	$C_f^P = 0.169_{-0.440}^{+0.101}, -0.169_{-0.101}^{+0.440}$			$C_u^P = 0.0_{-0.294}^{+0.300}$
				$C_d^S = 0.902_{-0.902}^{+0.075}$
				$C_d^P = 0.0_{-0.950}^{+0.951}$
				$C_\tau^S = 0.916_{-0.916}^{+0.044}$
				$C_f^P = 0.0_{-0.952}^{+0.954}$
$\chi_{\text{min}}^2/\text{dof}$	74.3500/72	78.1906/72	78.1707/71	74.1893/69
goodness of fit (gof)	0.4340	0.3175	0.2893	0.3129
p-value against the SM	0.0461	0.2450	0.3825	0.3188

We have the largest gof value for **CPV4-IUF** which is slightly higher than that of **CPV3-F**. The left panel of Fig. 10 is for **CPV4**. In the six left and middle frames, the CL regions in IUF are depicted and, in the two upper- and middle-right frames, those in HCC are shown in the $(\Delta S^\gamma, \Delta P^\gamma)$ and $(\Delta S^g, \Delta P^g)$ planes. The right panel of Fig. 10 is for **CPV5-IUHCC** and the CL regions in the $(\Delta S^\gamma, \Delta P^\gamma)$ and $(\Delta S^g, \Delta P^g)$ planes are depicted in the two left frames. In Fig. 11, we show the CL regions of **CPV7** in the $(C_{u,d,\ell}^S, C_{u,d,\ell}^P)$ planes in the upper three frames and some others below them.

In **CPV4-IUF**, $\Delta\Gamma_{\text{tot}}$ and C_V are driven to the SM values under the constraints of $\Delta\Gamma_{\text{tot}} \geq 0$ and $C_V \leq 1$ and, being different from **CPV2** and **CPV3**, we have the two degenerate minima at $(C_f^S, C_f^P) \simeq (0.90, \pm 0.17)$. The central value of C_f^S is smaller than those in the **CPC** fits by the amount of 2%-3% which is compensated by the relation of $\sqrt{(C_f^S)^2 + (C_f^P)^2} \simeq 0.92$ at the minima. The CL regions are shown in the left and middle six frames of the left panel of Fig. 10. Both the two degenerate minima are in the 68% CL region and the SM point is outside the 95% CL region, see the left three frames for C_f^P , $\Delta\Gamma_{\text{tot}}$, and C_V versus C_f^S .

In **CPV4-HCC**, we have the $\hat{\mu}(\gamma\gamma)$ circle centered at $(\Delta S^\gamma, \Delta P^\gamma) \simeq (7, 0)$ with the radius of about 7, see the upper-right frame of the left panel of Fig. 10. There is no visible change in $\Delta\chi^2$ above the minimum along the circle passing the center of the 68% CL region. On the other hand, we obtain the sickle-shaped CL region in the $(\Delta S^g, \Delta P^g)$ plane, see the middle-right frame of the left panel of Fig. 10. This is understood by the overlapping of the $\hat{\mu}(\text{ggF} + \text{bbH})$ and $\hat{\mu}(\mathcal{D} \neq \gamma\gamma, \text{gg})$ circles:

$$\begin{aligned} \hat{\mu}(\text{ggF} + \text{bbH})^{\text{CPV4-HCC}} &= [1 + 1.778 \Delta S^g + 0.758 (\Delta S^g)^2] + 0.779 (\Delta P^g)^2 \simeq 0.76 (\Delta S^g + 1.15)^2 + 0.78 (\Delta P^g)^2, \\ \hat{\mu}(\mathcal{D} \neq \gamma\gamma, \text{gg})^{\text{CPV4-HCC}} &\simeq \frac{1}{0.92 + 0.08 [(1 + \Delta S^g / |S_{\text{SM}}^g|)^2 + 0.96 (\Delta P^g / |S_{\text{SM}}^g|)^2]}. \end{aligned} \quad (53)$$

For $\hat{\mu}(\text{ggF} + \text{bbH})$, we use Eq. (22) with the Run 2 decomposition coefficients in Table VIII. We note that $\hat{\mu}(\text{ggF} + \text{bbH}) = 1$ gives a circle centered at $(\Delta S^g, \Delta P^g) \simeq (-1.15, 0)$ with the radius of about 1.15. In the second line for $\hat{\mu}(\mathcal{D} \neq \gamma\gamma, \text{gg})$, the factor 0.96 takes account of the difference in the QCD and electroweak corrections to the scalar and pseudoscalar parts [47]. With $S_{\text{SM}}^g = 0.636 + 0.071i$ and $P_{\text{SM}}^g = 0$, we note that $\hat{\mu}(\mathcal{D} \neq \gamma\gamma, \text{gg}) = 1$ gives a circle centered at $(\Delta S^g, \Delta P^g) \simeq (-0.64, 0)$ with the radius of about 0.64 which is smaller than the $\hat{\mu}(\text{ggF} + \text{bbH})$ circle. Note that we obtain the sickle-shaped CL region in the $(\Delta S^g, \Delta P^g)$ plane because we consider the ggF+bbH production process beyond LO in QCD.

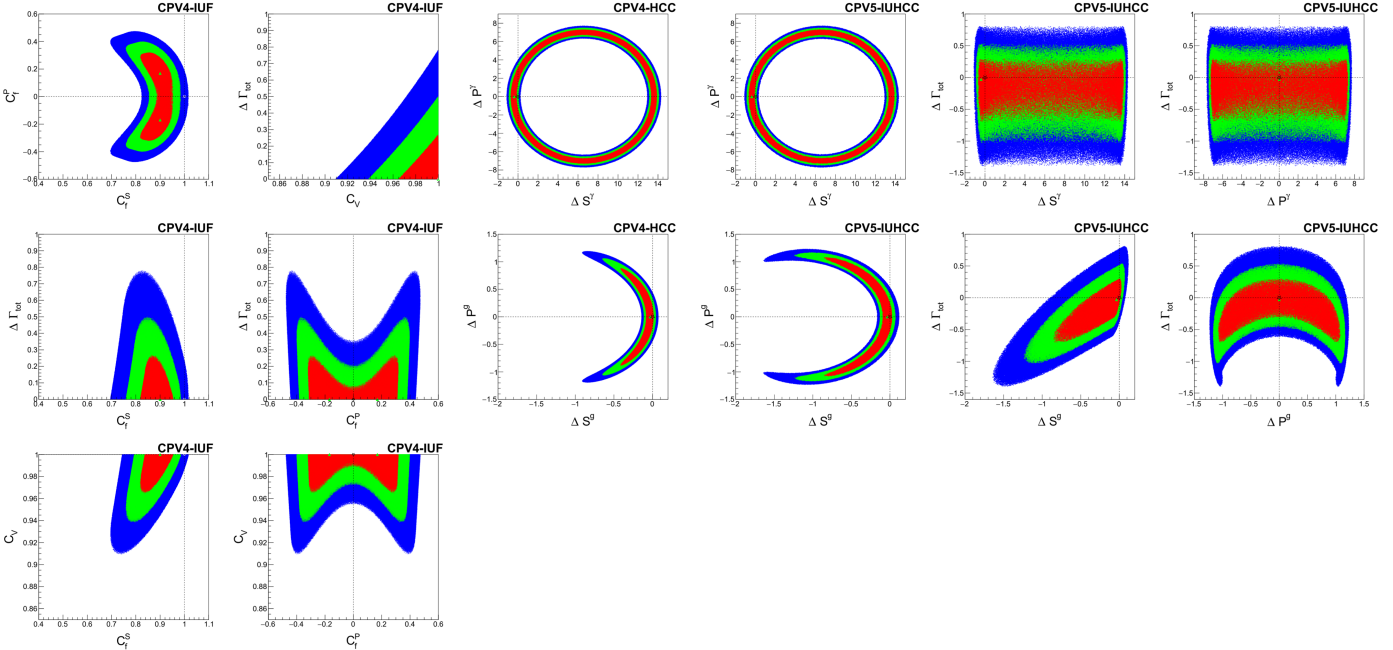


FIG. 10. **CPV4** and **CPV5**: [Left] The CL regions of **CPV4-IUF** (left and middle) and **CPV4-HCC** (right) in two-parameter planes. [Right] The CL regions of **CPV5-IUHCC** in two-parameter planes. The contour regions shown are for $\Delta\chi^2 \leq 2.3$ (red), $\Delta\chi^2 \leq 5.99$ (green), $\Delta\chi^2 \leq 11.83$ (blue) above the minimum, which correspond to confidence levels of 68.27%, 95%, and 99.73%, respectively. In each frame, the vertical and horizontal lines locate the SM point denoted by a star and the best-fit point is denoted by a triangle.

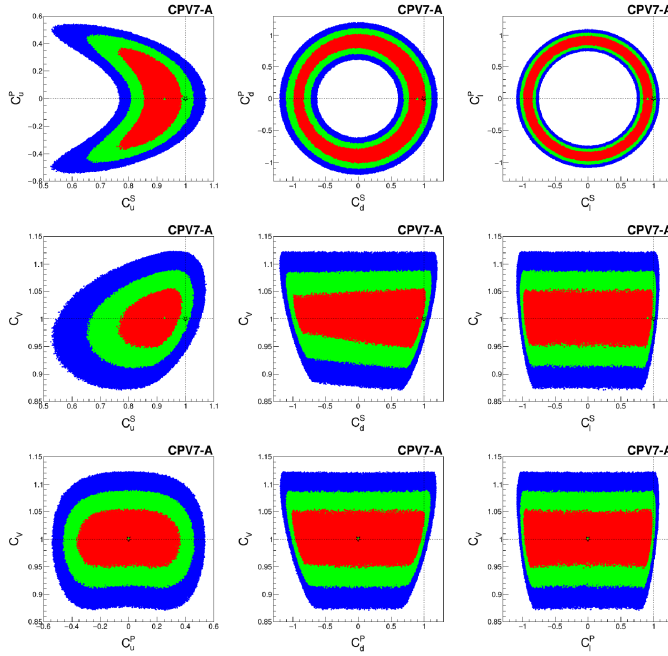


FIG. 11. **CPV7**: The CL regions of **CPV7-A** in two-parameter planes. The contour regions shown are for $\Delta\chi^2 \leq 2.3$ (red), $\Delta\chi^2 \leq 5.99$ (green), $\Delta\chi^2 \leq 11.83$ (blue) above the minimum, which correspond to confidence levels of 68.27%, 95%, and 99.73%, respectively. In each frame, the vertical and horizontal lines locate the SM point denoted by a star and the best-fit point is denoted by a triangle.

In **CPV5-IUHCC**, compared to **CPV4-HCC**, we vary $\Delta\Gamma_{\text{tot}}$ additionally. The best-fitted values are similar to those in **CPV4-HCC** with a bit larger errors for ΔS^g and ΔP^g . We observe that the sickle-shaped CL region in the $(\Delta S^g, \Delta P^g)$ plane extends at the cost of negative $\Delta\Gamma_{\text{tot}}$, see the middle three frames in the right panel of Fig. 10. Note that $\Delta\Gamma_{\text{tot}}$ is almost insensitive to ΔS^γ and ΔP^γ in the allowed regions.

In **CPV7-A**, C_V is consistent with the SM with the 1σ error less than 4%. The scalar couplings $C_{u,d,\ell}^S$ below the SM with the positive 1σ errors of 4-8%. The negative 1σ errors are larger or much larger: about 10% for C_u^S and almost 100% for $C_{d,\ell}^S$. Comparing with the best-fitted values in **CPC4-A**, we find that the central values and the positive errors of $C_{u,d,\ell}^S$ are similar while the negative errors extend to the negative direction and the positive and negative regions are connected for $C_{d,\ell}^S$: compare the CL regions shown in the upper frames of the left panel of Fig 6 (**CPC4-A**) and those in the middle frames of Fig 11 (**CPV7-A**). For the pseudoscalar couplings, C_u^P is constrained around its SM value of 0 with the 1σ error of 30%. For the other pseudoscalar couplings of C_d^P and C_ℓ^P , we have the 1σ errors of about 100%. We clearly see the SM points outside of the 68% CL in the (C_u^S, C_u^P) and (C_u^S, C_V) planes, see the upper- and middle-left frames of Fig. 11.

C. Predictions for $H \rightarrow Z\gamma$

Recently, the ATLAS and CMS collaborations report the first evidence for the Higgs boson decay to a Z boson and a photon with a statistical significance of 3.4 standard deviations based on the Run 2 data with 140/fb luminosity for each experiment [14]. The combined analysis gives the measured signal yield of 2.2 ± 0.7 times the SM prediction which corresponds to $B(H \rightarrow Z\gamma) = (3.4 \pm 1.1) \times 10^{-3}$ assuming SM Higgs boson production cross sections.²⁵

The loop-induced Higgs couplings to a Z boson and a photon are similarly described as those to two photons and two gluons by using the scalar and pseudoscalar form factors of $S^{Z\gamma}$ and $P^{Z\gamma}$. For the detailed description and analytic structure of them, we refer to Ref. [47]. Taking $M_H = 125$ GeV, we have

$$\begin{aligned} S^{Z\gamma} &= -12.3401 g_{HWW} + 0.6891 g_{H\bar{t}t}^S + (-0.0186 + 0.0111 i) g_{H\bar{b}b}^S + (-0.0005 + 0.0002 i) g_{H\tau\tau}^S + \Delta S^{Z\gamma}, \\ P^{Z\gamma} &= 1.0459 g_{H\bar{t}t}^P + (-0.0219 + 0.0112 i) g_{H\bar{b}b}^P + (-0.0006 + 0.0002 i) g_{H\tau\tau}^P + \Delta P^{Z\gamma}, \end{aligned} \quad (54)$$

²⁵ The SM prediction for $B(H \rightarrow Z\gamma)$ is 1.58×10^{-3} [47].

retaining only the dominant contributions from third-generation SM fermions and the charged gauge bosons W^\pm and introducing $\Delta S^{Z\gamma}$ and $\Delta P^{Z\gamma}$ to parametrize contributions from the triangle loops in which non-SM charged particles are running. In the SM limit, $S_{\text{SM}}^{Z\gamma} = -11.6701 + 0.0114i$ and $P_{\text{SM}}^{Z\gamma} = 0$.

We first examine how large $\hat{\mu}(Z\gamma)$ can be in **CPC2-I** in which C_V and C_f^S are varied in the absence of non-SM particles contributing to $\Delta S^{Z\gamma}$. In this scenario, we have

$$\hat{\mu}(Z\gamma)^{\text{CPC2-I}} = \frac{\Gamma_{\text{tot}}(H_{\text{SM}})}{\Gamma_{\text{tot}}(H)} \frac{|S^{Z\gamma}|^2}{|S_{\text{SM}}^{Z\gamma}|^2} \simeq 4 \frac{|1.06 C_V - 0.06 C_f^S|^2}{C_V^2 + 3(C_f^S)^2}, \quad (55)$$

where we use Eq. (C.2) for $\Gamma_{\text{tot}}(H_{\text{SM}})/\Gamma_{\text{tot}}(H)$. Using the best-fitted values of $C_V = 1.015 \pm 0.017$ and $C_f^S = 0.930 \pm 0.031$ in **CPC2-I**, see Table XII, we have

$$\hat{\mu}(Z\gamma)^{\text{CPC2-I}} \simeq 1.15_{-0.13}^{+0.14} \quad (95\% \text{ CL}), \quad (56)$$

leading to the enhanced Higgs decay into $Z\gamma$ by the amount of 30% at the upper boundary of the 95% CL region which is in the right direction to be consistent with the the measured signal strength of 2.2 ± 0.7 . We note that C_f^S fitted below the SM value of 1 increases $\hat{\mu}(Z\gamma)$, see the two **CPC2-I** frames of Fig. 12. In **CPC4-A** and **CPC6-CSBLUB** where we have the more fitting parameters of the gauge-Higgs and Yukawa couplings but still with $\Delta S^{Z\gamma} = 0$, we find that

$$\hat{\mu}(Z\gamma)^{\text{CPC4-A}} \simeq \hat{\mu}(Z\gamma)^{\text{CPC6-CSBLUB}} \simeq 1.17_{-0.19}^{+0.25} \quad (95\% \text{ CL}), \quad (57)$$

which leads to the enhanced Higgs decay into $Z\gamma$ by the amount of 40% at the upper boundary of the 95% CL region with the larger errors compared to **CPC2-I**, see the four **CPC4-A** and **CPC6-CSBLUB** frames of Fig. 12. We observe that CP violation does not alter the situation, see the two **CPV7-A** frames of Fig. 12. These observations indicate that one might need nonvanishing $\Delta S^{Z\gamma} \sim -5$ to accommodate the measured $H \rightarrow Z\gamma$ signal strength of 2.2 ± 0.7 comfortably. For global fits including the $H \rightarrow Z\gamma$ data, see Appendix E.

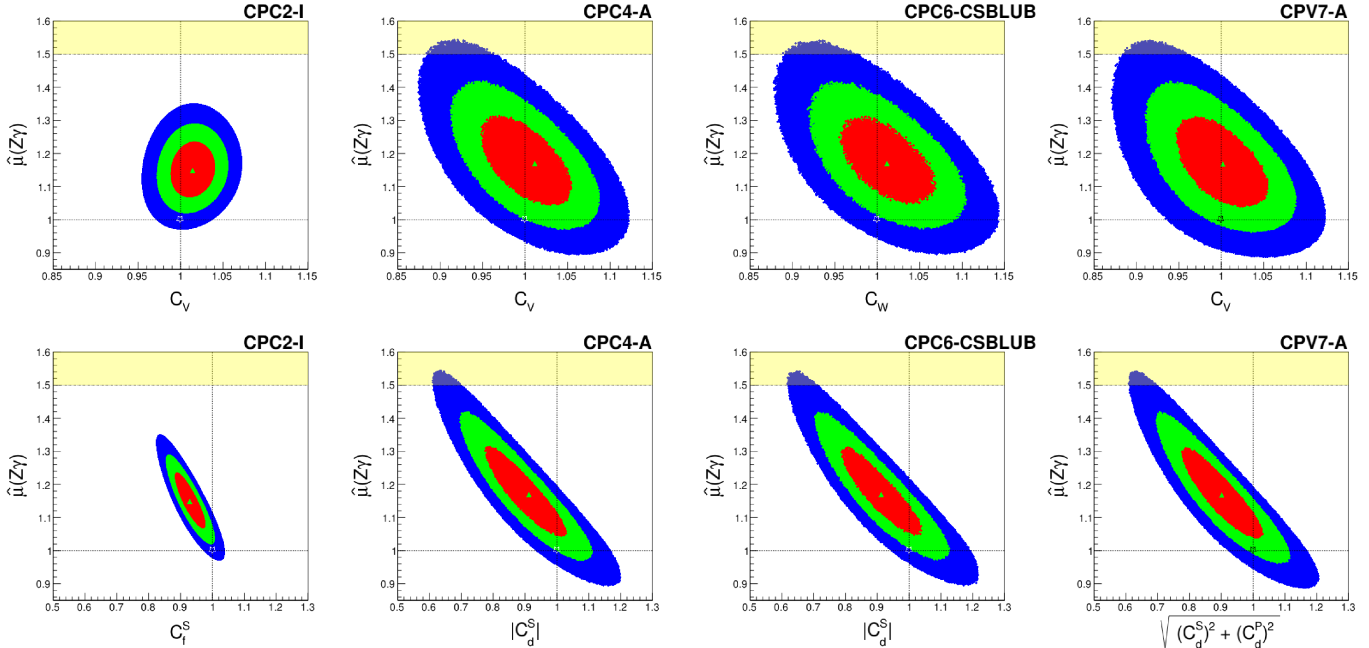


FIG. 12. Predictions for $\hat{\mu}(Z\gamma)$ in **CPC2-I**, **CPC4-A**, **CPC6-CSBLUB**, and **CPV7-A**. The upper frames are versus C_V , C_V , C_W , and C_V and the lower ones versus C_f^S , $|C_d^S|$, $|C_d^P|$ and $\sqrt{(C_d^S)^2 + (C_d^P)^2}$ from **CPC2-I** to **CPV7-A**. In each frame, the horizontal line at $\hat{\mu}(Z\gamma) = 1.5$ denotes the lower boundary of the shaded 1σ region of the measured $H \rightarrow Z\gamma$ signal strength of 2.2 ± 0.7 [14]. The contour regions shown are for $\Delta\chi^2 \leq 2.3$ (red), $\Delta\chi^2 \leq 5.99$ (green), $\Delta\chi^2 \leq 11.83$ (blue) above the minimum, which correspond to confidence levels of 68.27%, 95%, and 99.73%, respectively. In each frame, the vertical and horizontal lines locate the SM point denoted by a star and the best-fit point is denoted by a triangle.

V. CONCLUSIONS

We perform global fits of the Higgs boson couplings to the full Higgs datasets collected at the LHC with the integrated luminosities per experiment of approximately 5/fb at 7 TeV, 20/fb at 8 TeV, and up to 139/fb at 13 TeV. To enhance the sensitivity of our global analysis, we combine the LHC Run 1 dataset with the two Run 2 datasets separately given by the ATLAS and CMS collaborations ignoring correlations among them. We have carefully chosen the 76 production-times-decay signal strengths and, based on them, we consistently reproduce the global and individual (production and decay) signal strengths in the literature. We further demonstrate that our combined analysis based on the 76 experimental signal strengths and the theoretical ones elaborated in this work reliably reproduce the fitting results presented in Ref. [13] (Run 1) and Refs. [3, 4] (Run 2) within 0.5 standard deviations. Note that we have included the production signal strength for the tH process to accommodate the new feature of the LHC Run 2 data and considered the ggF production process beyond leading order in QCD to match the level of precision of the LHC Run 2 data.

We have implemented the 22 CPC subfits from **CPC1** to **CPC6** in Table X and the 13 CPV subfits from **CPV2** to **CPV7** in Table XV taking account of various scenarios found in several well-motivated BSM models. Our extensive and comprehensive analysis reveals that the LHC Higgs precision data are no longer best described by the SM Higgs boson.²⁶ For example, in **CPC2-I** for which we obtain the higher gof value of 0.47 than in the SM and the low p -value of 0.02 for compatibility with the SM, we find the following best-fitted values of

$$C_V^{\text{CPC2-I}} = 1.015 \pm 0.017; \quad (C_f^S)^{\text{CPC2-I}} = 0.930 \pm 0.031,$$

with C_V being consistent with the SM with the 1σ error of 2% and C_f^S below the SM by more than 2 standard deviations with the 1σ error of 3%. We show that this could be understood by looking into the individual decay signal strengths presented in Table VI: $\gamma\gamma$ gives the relation $C_f^S \sim 3C_V - 2.1$ around the SM point under which WW^* and ZZ^* drive C_V near to the SM value of 1 while the Yukawa couplings are driven smaller to match the signal strengths of about 0.9 for $pp \rightarrow H \rightarrow bb$ and $pp \rightarrow H \rightarrow \tau\tau$. In **CPC3**, **CPC4**, **CPC5**, and **CPC6** where we have the more fitting parameters of the gauge-Higgs and Yukawa couplings, we find that these features remain the same but with a bit larger 1σ errors. Explicitly, we observe the following behavior of the gauge-Higgs and Yukawa couplings to the SM particles:

- C_V, C_W, C_Z : consistent with the SM with the 1σ error of 2%-3%
- $C_u^S, C_{ud}^S, C_{u\ell}^S$: about 2σ below the SM with the 1σ error of 3%-4%
- $C_{d\ell}^S, C_\ell^S, C_\tau^S$: about 2σ below the SM with the 1σ error of 4%-5%
- C_d^S : about 1σ below the SM with the 1σ error of 7%-8%
- $|C_\mu^S|$: consistent with the SM with the 1σ error of 12-15%

Incidentally, in many of the two-parameter planes, the SM points locate outside the 68% CL region easily and even the 95% CL region sometimes. In Fig. 13, we compare the gof values of all the **CPCn** and **CPVn** subfits considered in this work. We indeed observe that the most of them have the better goodness of fit than the SM. Incidentally, we note that CP violation is largely unconstrained by the LHC Higgs data with the CL regions appearing as a circle or an ellipse or some overlapping of them in the CP-violating two-parameter planes. We explain the details of how the ellipses and circles emerge in several subfits of **CPVn**. Especially, in **CPV4-HCC** and **CPV5-IUHCC**, we note that the sickle-shaped CL regions in the $(\Delta S^g, \Delta P^g)$ plane are obtained since we consider the ggF production beyond LO in QCD,

Interestingly, we find that the BSM models predicting the same normalized Yukawa couplings to the up- and down-type quarks and charged leptons are preferred. For example, among the four types of 2HDMs classified according to the Glashow-Weinberg condition to avoid FCNCs, this could be achieved only in the type-I 2HDM. Last but not least, we note that the reduced Yukawa couplings help to explain the combined $H \rightarrow Z\gamma$ signal strength of 2.2 ± 0.7 recently reported by the ATLAS and CMS collaborations [14]. But one might need nonvanishing $\Delta S^{Z\gamma} \sim -5$ to comfortably accommodate the large central value of 2.2.

ACKNOWLEDGMENT

We thank Kingman Cheung for the informative comments regarding $H \rightarrow Z\gamma$ and statistics. Our thanks go to Seong Youl Choi, Pyungwon Ko, Chan Beom Park, Seodong Shin, Minho Son, Jeonghyeon Song, and Hwidong Yoo for ample

²⁶ We remind that the SM value of goodness of fit is only 0.29 with $\chi_{\text{SM}}^2/\text{dof} = 82/76$.

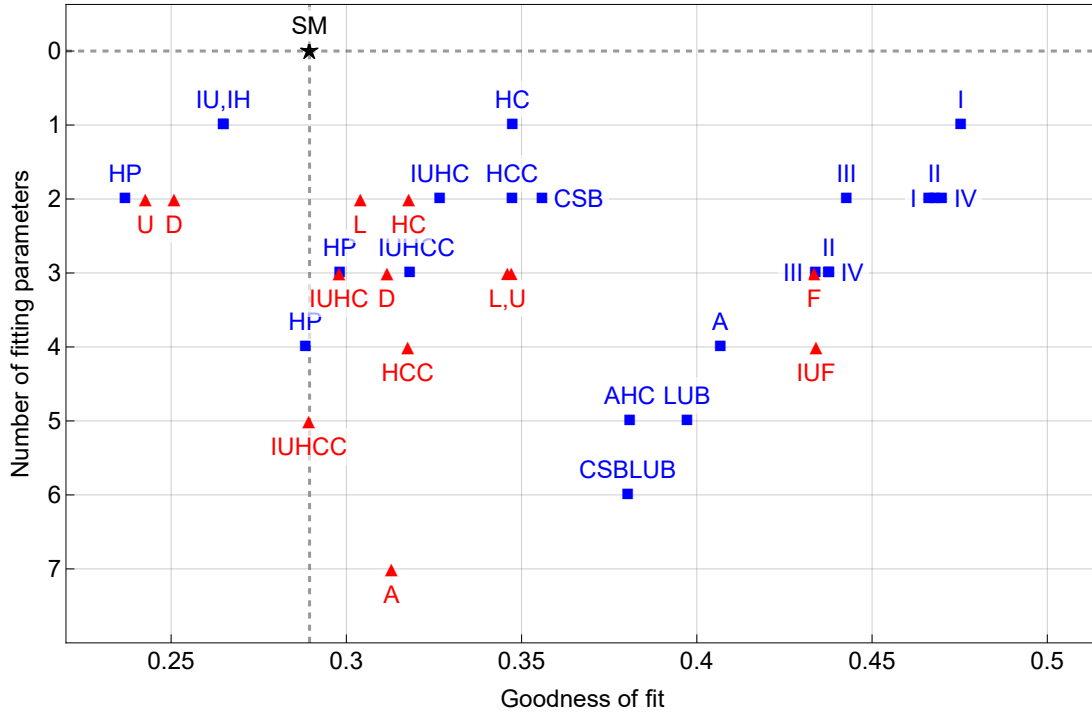


FIG. 13. Goodness of fit of the **CPCn** (blue boxes) and **CPVn** (red triangles) subfits considered in this work. The SM point is denoted by a star.

discussions at 2024 LSSU Theory Meeting for Future Colliders. This work was supported by the National Research Foundation (NRF) of Korea Grant No. NRF-2021R1A2B5B02087078 (Y.H., D.-W.J., J.S.L.). The work of D.-W.J. was also supported in part by the NRF of Korea Grant No. NRF-2019R1A2C1089334, No. NRF-2021R1A2C2011003, and No. RS-2023-00246268 and in part by IBS under the project code IBS-R018-D3. The work of J.S.L. was also supported in part by the NRF of Korea Grant No. NRF-2022R1A5A1030700.

APPENDICES

Appendix A: $\hat{\mu}(\text{ggF})$ beyond LO in QCD

The ggF productions signal strength is given by

$$\hat{\mu}(\text{ggF}) = \frac{\sigma_{\text{ggF}}}{\sigma_{\text{ggF}}^{\text{SM}}}. \quad (\text{A.1})$$

At LO, $\hat{\mu}(\text{ggF})$ is given by the following ratio in terms of the absolute squares of the relevant scalar and pseudoscalar form factors:

$$\hat{\mu}(\text{ggF})^{\text{LO}} = \frac{|S^g(M_H)|^2 + |P^g(M_H)|^2}{|S_{\text{SM}}^g(M_H)|^2}, \quad (\text{A.2})$$

numerator of which depends on the model-independent Yukawa couplings of $g_{H\bar{t}t}^{S,P}$, $g_{H\bar{b}b}^{S,P}$, and $g_{H\bar{c}c}^{S,P}$, and the non-SM parameters of ΔS^g and ΔP^g denoting the contributions from the triangle loops in which non-SM colored particles are running. The LO ggF production signal strength should be reliable only if some higher order corrections to the non-SM cross section σ_{ggF} and those to the SM cross section $\sigma_{\text{ggF}}^{\text{SM}}$ are largely canceled out in the ratio. It turns out this is not the case with the QCD corrections [50] and, in this work, we consider the production signal strength beyond LO in QCD. Using the numerical expressions for the form factors given in Eq. (14) for $M_H = 125$ GeV, we have the following LO ggF

TABLE XVIII. σ_{ggF}^S at $N^3\text{LO}$ and σ_{ggF}^P at NNLO for several combinations of the relevant Yukawa couplings obtained by using **SusHi-1.7.0** [53, 54] with **PDF4LHC15** [66]. For each combination of the Yukawa couplings, σ_{bbH} at NNLO is also shown. We consider three values of $\sqrt{s} = 7 \text{ TeV}, 8 \text{ TeV}, \text{ and } 13 \text{ TeV}$ and $M_H = 125 \text{ GeV}$ has been taken. The renormalization and factorization scales are chosen $\mu_R = \mu_F = M_H/2$ for σ_{ggF} and $\mu_R = 4\mu_F = M_H$ for σ_{bbH} . When $g_{H\bar{t}t}^{S,P} = 1$ and $g_{H\bar{b}b}^{S,P} = g_{H\bar{c}c}^{S,P} = 0$, the LO ggF cross sections are also shown in parentheses.

Couplings			σ_{ggF}^S (pb)			σ_{bbH} (pb)			Couplings			σ_{ggF}^P (pb)			σ_{bbH} (pb)		
$g_{H\bar{t}t}^S$	$g_{H\bar{b}b}^S$	$g_{H\bar{c}c}^S$	7 TeV	8 TeV	13 TeV	7 TeV	8 TeV	13 TeV	$g_{H\bar{t}t}^P$	$g_{H\bar{b}b}^P$	$g_{H\bar{c}c}^P$	7 TeV	8 TeV	13 TeV	7 TeV	8 TeV	13 TeV
1	1	1	16.66	21.21	48.29	0.18	0.23	0.55	1	1	1	35.85	45.57	103.23	0.18	0.23	0.55
1	0	0	17.70 (5.91)	22.50 (7.46)	50.95 (16.44)	0	0	0	1	0	0	37.87 (13.67)	48.09 (17.26)	108.52 (38.06)	0	0	0
0	1	0	0.12	0.15	0.32	0.18	0.23	0.55	0	1	0	0.13	0.16	0.34	0.18	0.23	0.55
0	0	1	0.004	0.005	0.01	0	0	0	0	0	1	0.004	0.005	0.01	0	0	0
1	1	0	16.84	21.43	48.75	0.18	0.23	0.55	1	1	0	36.17	45.98	104.08	0.18	0.23	0.55
1	0	1	17.48	22.22	50.39	0	0	0	1	0	1	37.49	47.63	107.55	0	0	0
0	1	1	0.16	0.20	0.44	0.18	0.23	0.55	0	1	1	0.17	0.22	0.47	0.18	0.23	0.55

production signal strength:

$$\begin{aligned} \hat{\mu}(\text{ggF})^{\text{LO}} \simeq & 1.158 (g_{H\bar{t}t}^S)^2 + 0.014 (g_{H\bar{b}b}^S)^2 - 0.145 (g_{H\bar{t}t}^S g_{H\bar{b}b}^S) - 0.032 (g_{H\bar{t}t}^S g_{H\bar{c}c}^S) + 3.364 (g_{H\bar{t}t}^S \Delta S^g) + 2.444 (\Delta S^g)^2 \\ & + 2.680 (g_{H\bar{t}t}^P)^2 + 0.016 (g_{H\bar{b}b}^P)^2 - 0.254 (g_{H\bar{t}t}^P g_{H\bar{b}b}^P) - 0.051 (g_{H\bar{t}t}^P g_{H\bar{c}c}^P) + 5.118 (g_{H\bar{t}t}^P \Delta P^g) + 2.444 (\Delta P^g)^2, \end{aligned} \quad (\text{A.3})$$

assuming that ΔS^g and ΔP^g are real and the interferences terms proportional to the products of $g_{H\bar{b}b}^{S,P} \times g_{H\bar{c}c}^{S,P}$, $g_{H\bar{b}b}^S g_{H\bar{c}c}^S \times \Delta S^g$, $g_{H\bar{b}b}^P g_{H\bar{c}c}^P \times \Delta P^g$ and the diagonal terms $(g_{H\bar{c}c}^{S,P})^2$ have been neglected.

To go beyond LO in QCD, to begin with, we consider the contributions from top-, bottom-, and charm-quark loops taking $\Delta S^g = \Delta P^g = 0$. In this case, the ggF production cross section of a CP-mixed Higgs boson H might be organized as follow:

$$\sigma_{\text{ggF}} = \sigma_{\text{ggF}}^S (g_{H\bar{t}t}^S, g_{H\bar{b}b}^S, g_{H\bar{c}c}^S) + \sigma_{\text{ggF}}^P (g_{H\bar{t}t}^P, g_{H\bar{b}b}^P, g_{H\bar{c}c}^P), \quad (\text{A.4})$$

where

$$\begin{aligned} \sigma_{\text{ggF}}^S (g_{H\bar{t}t}^S, g_{H\bar{b}b}^S, g_{H\bar{c}c}^S) & \equiv (g_{H\bar{t}t}^S)^2 \sigma_{tt}^S + (g_{H\bar{b}b}^S)^2 \sigma_{bb}^S + (g_{H\bar{t}t}^S g_{H\bar{b}b}^S) \sigma_{tb}^S + (g_{H\bar{t}t}^S g_{H\bar{c}c}^S) \sigma_{tc}^S + \mathcal{O}(\sigma_{cc}^S, \sigma_{bc}^S), \\ \sigma_{\text{ggF}}^P (g_{H\bar{t}t}^P, g_{H\bar{b}b}^P, g_{H\bar{c}c}^P) & \equiv (g_{H\bar{t}t}^P)^2 \sigma_{tt}^P + (g_{H\bar{b}b}^P)^2 \sigma_{bb}^P + (g_{H\bar{t}t}^P g_{H\bar{b}b}^P) \sigma_{tb}^P + (g_{H\bar{t}t}^P g_{H\bar{c}c}^P) \sigma_{tc}^P + \mathcal{O}(\sigma_{cc}^P, \sigma_{bc}^P). \end{aligned} \quad (\text{A.5})$$

In Table XVIII, we present various ggF and bbH cross sections obtained by using **SusHi-1.7.0** [53, 54] for several combinations of the $g_{H\bar{q}q}^{S,P}$ couplings at $\sqrt{s} = 7 \text{ TeV}, 8 \text{ TeV}, \text{ and } 13 \text{ TeV}$. Neglecting $\sigma_{cc}^{S,P} \lesssim 0.01 \text{ pb}$ and $\sigma_{bc}^{S,P} \lesssim 0.1 \text{ pb}$, at each value of \sqrt{s} , one may derive the interference cross sections as follows:

$$\begin{aligned} \sigma_{tb}^{S,P} & = \sigma_{\text{ggF}}^{S,P}(1, 1, 1) - \sigma_{\text{ggF}}^{S,P}(1, 0, 1) - \sigma_{\text{ggF}}^{S,P}(0, 1, 0), \\ \sigma_{tc}^{S,P} & = \sigma_{\text{ggF}}^{S,P}(1, 1, 1) - \sigma_{\text{ggF}}^{S,P}(1, 1, 0), \end{aligned} \quad (\text{A.6})$$

together with the diagonal ones $\sigma_{tt}^{S,P} = \sigma_{\text{ggF}}^{S,P}(1, 0, 0)$ and $\sigma_{bb}^{S,P} = \sigma_{\text{ggF}}^{S,P}(0, 1, 0)$. Explicitly, at $\sqrt{s} = 13 \text{ TeV}$, we have $\sigma_{tt}^{S,P}$, $\sigma_{bb}^{S,P}$, $\sigma_{tb}^{S,P}$, and $\sigma_{tc}^{S,P}$ in pb:

$$\begin{aligned} \sigma_{tt}^S & = 50.95, \quad \sigma_{bb}^S = 0.32, \quad \sigma_{tb}^S = -2.42, \quad \sigma_{tc}^S = -0.46; \\ \sigma_{tt}^P & = 108.52, \quad \sigma_{bb}^P = 0.34, \quad \sigma_{tb}^P = -4.67, \quad \sigma_{tc}^P = -0.85. \end{aligned} \quad (\text{A.7})$$

Then, one might obtain

$$\begin{aligned}
\widehat{\mu}(\text{ggF})|_{13 \text{ TeV}}^{tbc} &= \frac{\sigma_{\text{ggF}}}{\sigma_{\text{ggF}}^{\text{SM}}}\bigg|_{13 \text{ TeV}}^{tbc} = \frac{\sum_{X=S,P} [(g_{H\bar{t}t}^X)^2 \sigma_{tt}^X + (g_{H\bar{b}b}^X)^2 \sigma_{bb}^X + (g_{H\bar{t}t}^X g_{H\bar{b}b}^X) \sigma_{tb}^X + (g_{H\bar{t}t}^X g_{H\bar{c}c}^X) \sigma_{tc}^X]}{\sigma_{\text{ggF}}^S(1,1)}\bigg|_{13 \text{ TeV}} \\
&= 1.055 (g_{H\bar{t}t}^S)^2 + 0.007 (g_{H\bar{b}b}^S)^2 - 0.050 (g_{H\bar{t}t}^S g_{H\bar{b}b}^S) - 0.010 (g_{H\bar{t}t}^S g_{H\bar{c}c}^S) \\
&\quad + 2.248 (g_{H\bar{t}t}^P)^2 + 0.007 (g_{H\bar{b}b}^P)^2 - 0.097 (g_{H\bar{t}t}^P g_{H\bar{b}b}^P) - 0.018 (g_{H\bar{t}t}^P g_{H\bar{c}c}^P). \tag{A.8}
\end{aligned}$$

Similarly, using the cross sections at $\sqrt{s} = 7 \text{ TeV}$ and 8 TeV shown in Table XVIII, we also obtain

$$\begin{aligned}
\widehat{\mu}(\text{ggF})|_{7\oplus 8 \text{ TeV}}^{tbc} &= \frac{\sigma_{\text{ggF}}}{\sigma_{\text{ggF}}^{\text{SM}}}\bigg|_{7\oplus 8 \text{ TeV}}^{tbc} = \frac{\sum_{X=S,P} [(g_{H\bar{t}t}^X)^2 \sigma_{tt}^X + (g_{H\bar{b}b}^X)^2 \sigma_{bb}^X + (g_{H\bar{t}t}^X g_{H\bar{b}b}^X) \sigma_{tb}^X + (g_{H\bar{t}t}^X g_{H\bar{c}c}^X) \sigma_{tc}^X]}{\sigma_{\text{ggF}}^S(1,1)}\bigg|_{7\oplus 8 \text{ TeV}} \\
&= 1.061 (g_{H\bar{t}t}^S)^2 + 0.007 (g_{H\bar{b}b}^S)^2 - 0.055 (g_{H\bar{t}t}^S g_{H\bar{b}b}^S) - 0.011 (g_{H\bar{t}t}^S g_{H\bar{c}c}^S) \\
&\quad + 2.268 (g_{H\bar{t}t}^P)^2 + 0.007 (g_{H\bar{b}b}^P)^2 - 0.105 (g_{H\bar{t}t}^P g_{H\bar{b}b}^P) - 0.019 (g_{H\bar{t}t}^P g_{H\bar{c}c}^P), \tag{A.9}
\end{aligned}$$

where we use the luminosity-weighted cross sections for the Run 1 data at $\sqrt{s} = 7 \oplus 8 \text{ TeV}$:

$$\sigma_{qq^{(\prime)}}^{S,P}\big|_{7\oplus 8 \text{ TeV}} = \frac{5.1 \text{ fb}^{-1} \times \sigma_{qq^{(\prime)}}^{S,P}\big|_{7 \text{ TeV}} + 19.6 \text{ fb}^{-1} \times \sigma_{qq^{(\prime)}}^{S,P}\big|_{8 \text{ TeV}}}{5.1 \text{ fb}^{-1} + 19.6 \text{ fb}^{-1}}, \tag{A.10}$$

for $qq^{(\prime)} = tt, bb, tb, tc$ and similarly for $\sigma_{\text{ggF}}^S(1,1)|_{7\oplus 8 \text{ TeV}}$. We note that the decomposition coefficients are almost independent of \sqrt{s} .²⁷ On the other hand, comparing with the LO result Eq. (A.3), we observe that the coefficients proportional to $(g_{H\bar{t}t}^S)^2$ and $(g_{H\bar{t}t}^P)^2$ decrease by the factors of 0.92 and 0.85, respectively, while the other coefficients by factors of about 2 to 3.

Next, neglecting the interference terms proportional to the products of $g_{H\bar{b}b, H\bar{c}c}^S \times \Delta S^g$ and assuming H is CP even with $P^g = 0$, we address the case with $\Delta S^g \neq 0$. In this case, including the QCD corrections to the top-quark loops, the form factor S^g might be written as

$$S^g = (1 + \epsilon_{tt}^S) S_{tt}^g + \Delta S^g, \tag{A.11}$$

where ϵ_{tt}^S denotes the QCD corrections with $\epsilon_{tt}^S = 0$ at LO and $S_{tt}^g = 2/3 g_{H\bar{t}t}^S$ in the limit of $M_t \rightarrow \infty$. The cross section is proportional to $|S^g|^2$ and it might be given by

$$\sigma_{\text{ggF}}^S = \mathcal{A}^S |S^g|^2 = \mathcal{A}^S |(1 + \epsilon_{tt}^S) S_{tt}^g + \Delta S^g|^2 = \mathcal{A}^S \left\{ |1 + \epsilon_{tt}^S|^2 |S_{tt}^g|^2 + 2\Re [(1 + \epsilon_{tt}^S) S_{tt}^g (\Delta S^g)^*] + |\Delta S^g|^2 \right\}. \tag{A.12}$$

When ΔS^g is real, one may reorganize it as follow

$$\sigma_{\text{ggF}}^S = (g_{H\bar{t}t}^S)^2 \sigma_{tt}^S + (g_{H\bar{t}t}^S) (\Delta S^g) \sigma_{t\Delta}^S + (\Delta S^g)^2 \sigma_{\Delta\Delta}^S \tag{A.13}$$

by identifying

$$\begin{aligned}
\mathcal{A}^S |1 + \epsilon_{tt}^S|^2 |S_{tt}^g|^2 &= (g_{H\bar{t}t}^S)^2 \sigma_{tt}^S \equiv (g_{H\bar{t}t}^S)^2 (\sigma_{tt}^S)^{\text{LO}} |1 + \epsilon_{tt}^S|^2, \\
2\mathcal{A}^S \Re [(1 + \epsilon_{tt}^S) S_{tt}^g (\Delta S^g)^*] &= (g_{H\bar{t}t}^S) (\Delta S^g) \sigma_{t\Delta}^S, \\
\mathcal{A}^S |\Delta S^g|^2 &= (\Delta S^g)^2 \sigma_{\Delta\Delta}^S. \tag{A.14}
\end{aligned}$$

Regarding σ_{tt}^S and $(\sigma_{tt}^S)^{\text{LO}}$ as inputs and taking $S_{tt}^g = 2/3 g_{H\bar{t}t}^S$, we have

$$|1 + \epsilon_{tt}^S| = \sqrt{\sigma_{tt}^S / (\sigma_{tt}^S)^{\text{LO}}}, \quad \mathcal{A}^S = \frac{9}{4} (\sigma_{tt}^S)^{\text{LO}}, \tag{A.15}$$

²⁷ We have also checked that the variation of the coefficients due to the change of M_H in the range between 125 GeV and 125.5 GeV are also negligible.

TABLE XIX. $\sigma_{t\Delta}^S$, $\sigma_{\Delta\Delta}^S$, $\sigma_{t\Delta}^P$, and $\sigma_{\Delta\Delta}^P$ in pb at $\sqrt{s} = 7$ TeV, 8 TeV, and 13 TeV obtained by using the relations given by Eqs. (A.16) and (A.19) and the cross sections $\sigma_{tt}^{S,P}$ and $(\sigma_{tt}^{S,P})^{\text{LO}}$ given in Table XVIII for $(g_{H\bar{t}t}^S, g_{H\bar{b}b}^S, g_{H\bar{c}c}^S) = (1, 0, 0)$. The estimation has been done in the limit of $M_t \rightarrow \infty$ taking $\Re(1 + \epsilon_{tt}^{S,P}) \approx |1 + \epsilon_{tt}^{S,P}|$ under the assumption that ΔS^g and ΔP^g are real.

\sqrt{s} (TeV)	$\sigma_{t\Delta}^S$	$\sigma_{\Delta\Delta}^S$	$\sigma_{t\Delta}^P$	$\sigma_{\Delta\Delta}^P$
7	30.67	13.29	45.50	13.67
8	38.86	16.78	57.62	17.26
13	86.84	37.00	128.54	38.06

which lead to

$$\begin{aligned}\sigma_{t\Delta}^S &= \frac{4}{3} \mathcal{A}^S \Re(1 + \epsilon_{tt}^S) \leq 3 \sqrt{\sigma_{tt}^S (\sigma_{tt}^S)^{\text{LO}}}, \\ \sigma_{\Delta\Delta}^S &= \mathcal{A}^S = \frac{9}{4} (\sigma_{tt}^S)^{\text{LO}},\end{aligned}\tag{A.16}$$

by noting that $\Re(1 + \epsilon_{tt}^S) \leq |1 + \epsilon_{tt}^S|$. Similarly, starting from

$$P^g = (1 + \epsilon_{tt}^P) P_{tt}^g + \Delta P^g \quad \text{and} \quad \sigma_{\text{ggF}}^P = \mathcal{A}^P |P^g|^2,\tag{A.17}$$

one might have

$$\sigma_{\text{ggF}}^P = (g_{H\bar{t}t}^P)^2 \sigma_{tt}^P + (g_{H\bar{t}t}^P)(\Delta P^g) \sigma_{t\Delta}^P + (\Delta P^g)^2 \sigma_{\Delta\Delta}^P,\tag{A.18}$$

where

$$\begin{aligned}\sigma_{t\Delta}^P &= 2 \mathcal{A}^P \Re(1 + \epsilon_{tt}^P) \leq 2 \sqrt{\sigma_{tt}^P (\sigma_{tt}^P)^{\text{LO}}}, \\ \sigma_{\Delta\Delta}^P &= \mathcal{A}^P = (\sigma_{tt}^P)^{\text{LO}},\end{aligned}\tag{A.19}$$

assuming that ΔP^g is real, taking $P_{tt}^g = g_{H\bar{t}t}^P$ in the infinite M_t limit, and using $\Re(1 + \epsilon_{tt}^P) \leq |1 + \epsilon_{tt}^P| = \sqrt{\sigma_{tt}^P / (\sigma_{tt}^P)^{\text{LO}}}$.

In Table XIX, we show the cross sections $\sigma_{t\Delta}^{S,P}$ and $\sigma_{\Delta\Delta}^{S,P}$ in pb at $\sqrt{s} = 7$ TeV, 8 TeV, and 13 TeV assuming ΔS^g and ΔP^g are real. We use the values of the cross sections $\sigma_{tt}^{S,P} = \sigma_{\text{ggF}}^{S,P}(1, 0, 0)$ and $(\sigma_{tt}^{S,P})^{\text{LO}}$ in Table XVIII together with the relations given by Eqs. (A.16) and (A.19). For $\sigma_{t\Delta}^{S,P}$, we take the approximation $\Re(1 + \epsilon_{tt}^{S,P}) \approx |1 + \epsilon_{tt}^{S,P}|$ and, for the contributions from the triangle top-quark loops, we take the $M_t \rightarrow \infty$ limit. Then, with the cross sections $\sigma_{t\Delta}^{S,P}$ and $\sigma_{\Delta\Delta}^{S,P}$ given, we derive

$$\begin{aligned}\hat{\mu}(\text{ggF})|_{13 \text{ TeV}}^{t\Delta} &= \frac{\sigma_{\text{ggF}}}{\sigma_{\text{ggF}}^{\text{SM}}}\bigg|_{13 \text{ TeV}}^{t\Delta} = \frac{\sum_{X=S,P} [(g_{H\bar{t}t}^X)^2 \sigma_{tt}^X + (g_{H\bar{t}t}^X)(\Delta X^g) \sigma_{t\Delta}^X + (\Delta X^g)^2 \sigma_{\Delta\Delta}^X]}{\sigma_{\text{ggF}}^S(1, 1, 1)}\bigg|_{13 \text{ TeV}} \\ &= 1.055 (g_{H\bar{t}t}^S)^2 + 1.799 (g_{H\bar{t}t}^S)(\Delta S^g) + 0.766 (\Delta S^g)^2 \\ &\quad + 2.248 (g_{H\bar{t}t}^P)^2 + 2.662 (g_{H\bar{t}t}^P)(\Delta P^g) + 0.788 (\Delta P^g)^2,\end{aligned}\tag{A.20}$$

and, similarly as before,

$$\begin{aligned}\hat{\mu}(\text{ggF})|_{7\oplus 8 \text{ TeV}}^{t\Delta} &= 1.061 (g_{H\bar{t}t}^S)^2 + 1.834 (g_{H\bar{t}t}^S)(\Delta S^g) + 0.792 (\Delta S^g)^2 \\ &\quad + 2.268 (g_{H\bar{t}t}^P)^2 + 2.719 (g_{H\bar{t}t}^P)(\Delta P^g) + 0.815 (\Delta P^g)^2.\end{aligned}\tag{A.21}$$

We again note that the decomposition coefficients are almost independent of \sqrt{s} and, comparing with the LO result Eq. (A.3), we observe that the coefficients proportional to the products of $(g_{H\bar{t}t}^S)(\Delta S^g)$ and $(g_{H\bar{t}t}^P)(\Delta P^g)$ and the squares of $(\Delta S^g)^2$ and $(\Delta P^g)^2$ decrease by factors of about 2 to 3.

Finally, combining $\widehat{\mu}(\text{ggF})|^{tb}$ given by Eqs. (A.8) and (A.9) and $\widehat{\mu}(\text{ggF})|^{t\Delta}$ given by Eqs. (A.20) and (A.21), we have arrived at

$$\begin{aligned}
\widehat{\mu}(\text{ggF})|_{13 \text{ TeV}} &= 1.055 (g_{H\bar{t}t}^S)^2 + 0.007 (g_{H\bar{b}b}^S)^2 - 0.050 (g_{H\bar{t}t}^S g_{H\bar{b}b}^S) - 0.010 (g_{H\bar{t}t}^S g_{H\bar{c}c}^S) + 1.799 (g_{H\bar{t}t}^S \Delta S^g) + 0.766 (\Delta S^g)^2 \\
&+ 2.248 (g_{H\bar{t}t}^P)^2 + 0.007 (g_{H\bar{b}b}^P)^2 - 0.097 (g_{H\bar{t}t}^P g_{H\bar{b}b}^P) - 0.018 (g_{H\bar{t}t}^P g_{H\bar{c}c}^P) + 2.662 (g_{H\bar{t}t}^P \Delta P^g) + 0.788 (\Delta P^g)^2; \\
\widehat{\mu}(\text{ggF})|_{7\oplus 8 \text{ TeV}} &= 1.061 (g_{H\bar{t}t}^S)^2 + 0.007 (g_{H\bar{b}b}^S)^2 - 0.055 (g_{H\bar{t}t}^S g_{H\bar{b}b}^S) - 0.011 (g_{H\bar{t}t}^S g_{H\bar{c}c}^S) + 1.834 (g_{H\bar{t}t}^S \Delta S^g) + 0.792 (\Delta S^g)^2 \\
&+ 2.268 (g_{H\bar{t}t}^P)^2 + 0.007 (g_{H\bar{b}b}^P)^2 - 0.105 (g_{H\bar{t}t}^P g_{H\bar{b}b}^P) - 0.019 (g_{H\bar{t}t}^P g_{H\bar{c}c}^P) + 2.719 (g_{H\bar{t}t}^P \Delta P^g) + 0.815 (\Delta P^g)^2.
\end{aligned} \tag{A.22}$$

Appendix B: Single variable behavior

In each box of Table XX and Table XXI, we show the best-fitted value, goodness of fit, and p -value against the SM for compatibility with the SM hypothesis when only a single non-SM or SM parameter is varied while all the other ones are taking the SM value of either 0 or 1. Also shown is $\Delta\chi^2$ above the minimum versus the single parameter varied. Note that four of them are the same as in **CPC1** and, otherwise, this is to check and see the chi-square behavior rather than to address some physics cases.

TABLE XX. The best-fitted value, goodness of fit (gof), and p -value against the SM for compatibility with the SM hypothesis when only a single parameter is varied. Also shown is $\Delta\chi^2$ above the minimum versus the single parameter varied. For the SM, we obtain $\chi^2_{\text{SM}}/\text{dof} = 82.3480/76$ and $\text{gof} = 0.2895$.

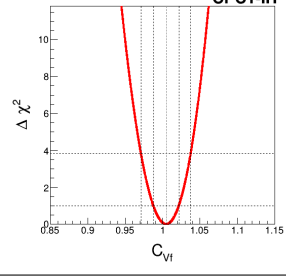
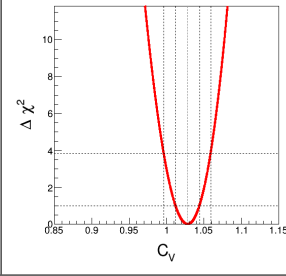
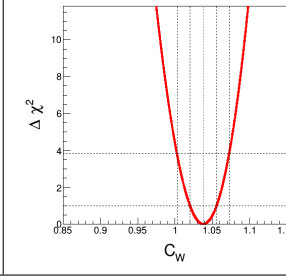
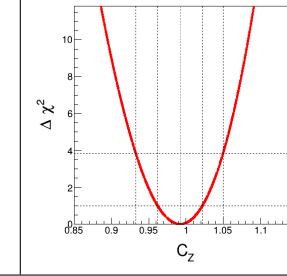
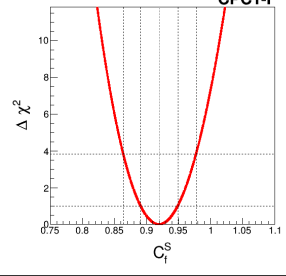
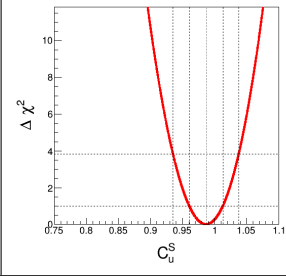
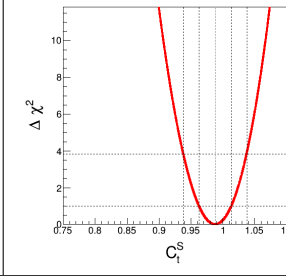
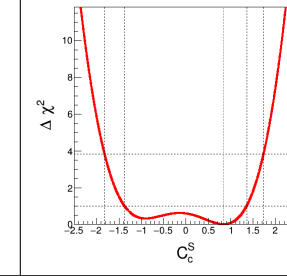
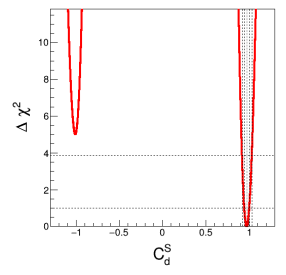
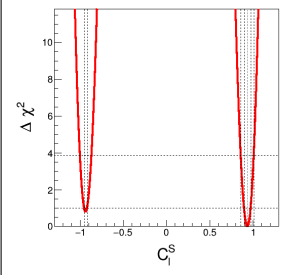
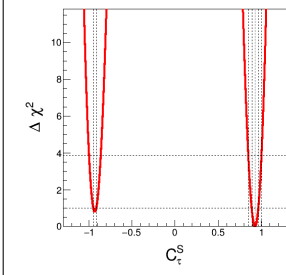
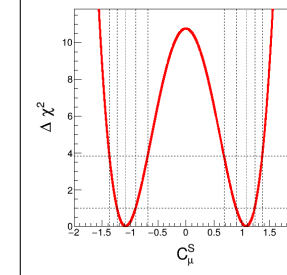
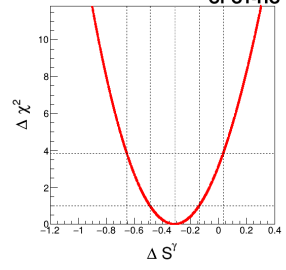
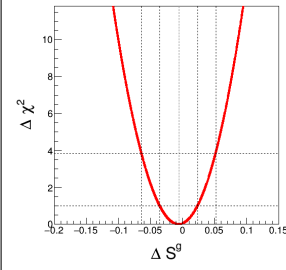
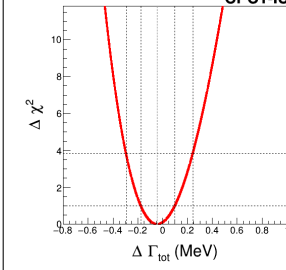
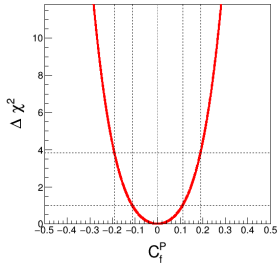
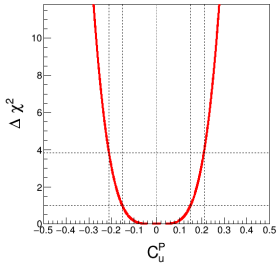
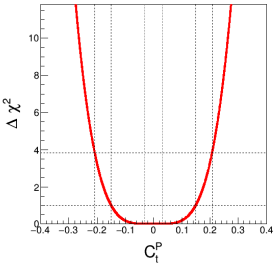
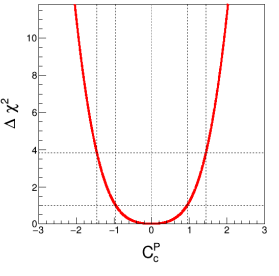
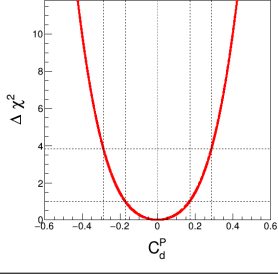
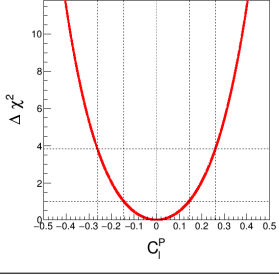
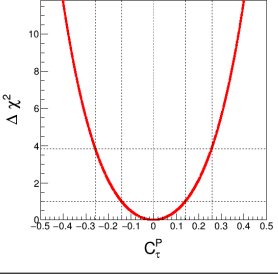
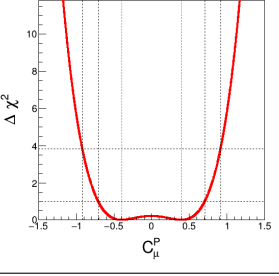
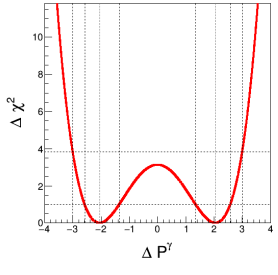
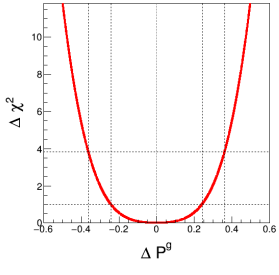
Varying Parameter	$C_{Vf} = 1.005^{+0.017}_{-0.017}$	$C_V = 1.028^{+0.016}_{-0.016}$	$C_W = 1.031^{+0.018}_{-0.018}$	$C_Z = 0.992^{+0.030}_{-0.030}$
gof	0.2649	0.3449	0.3867	0.2641
p -value	0.7590	0.0810	0.0349	0.8014
				
Varying Parameter	$C_f^S = 0.920^{+0.029}_{-0.029}$	$C_u^S = 0.987^{+0.026}_{-0.026}$	$C_t^S = 0.988^{+0.025}_{-0.025}$	$C_c^S = 0.847^{+0.513}_{-2.221}$
gof	0.4753	0.2687	0.2680	0.2643
p -value	0.0071	0.6209	0.6421	0.7948
				
Varying Parameter	$C_d^S = 0.978^{+0.029}_{-0.028}$	$C_\ell^S = 0.939^{+0.038}_{-0.039}$	$C_\tau^S = 0.933^{+0.038}_{-0.039}$	$C_\mu^S = +1.078^{+0.154}_{-0.180}, -1.078^{+0.180}_{-0.154}$
gof	0.2774	0.3330	0.3451	0.2678
p -value	0.4450	0.1048	0.0806	0.6473
				
Varying Parameter	$\Delta S^\gamma = -0.313^{+0.176}_{-0.176}$	$\Delta S^g = -0.006^{+0.029}_{-0.030}$	$\Delta\Gamma_{\text{tot}} = -0.042^{+0.142}_{-0.132} \text{ MeV}$	
gof	0.3474	0.2636	0.2649	
p -value	0.0769	0.8425	0.7590	
				

TABLE XXI. *Continued from Table XX.*

Varying Parameter	$C_f^P = 0.0_{-0.112}^{+0.112}$	$C_u^P = 0.0_{-0.152}^{+0.152}$	$C_t^P = +0.031_{-0.031}^{+0.119},$ $-0.031_{-0.119}^{+0.031}$	$C_c^P = 0.0_{-0.951}^{+0.951}$
gof	0.2626	0.2626	0.2626	0.2626
p -value	1.0	1.0	0.9635	1.0
				
Varying Parameter	$C_d^P = 0.0_{-0.172}^{+0.172}$	$C_l^P = 0.0_{-0.145}^{+0.145}$	$C_\tau^P = 0.0_{-0.141}^{+0.141}$	$C_\mu^P = +0.397_{-1.106}^{+0.312},$ $-0.397_{-0.312}^{+1.106}$
gof	0.2626	0.2626	0.2626	0.2678
p -value	1.0	1.0	1.0	0.6473
				
Varying Parameter	$\Delta P^\gamma = +2.053_{-0.703}^{+0.529},$ $-2.053_{-0.529}^{+0.703}$	$\Delta P^g = 0.0_{-0.242}^{+0.242}$		
gof	0.3473	0.2626		
p -value	0.0770	1.0		
				

Appendix C: Parametric dependence of $\hat{\mu}(\gamma\gamma)$ in CPC2-I

In **CPC2-I** in which C_V and C_f^S are varied, we have the following decay signal strength for $H \rightarrow \gamma\gamma$:

$$\hat{\mu}(\gamma\gamma)^{\text{CPC2-I}} = \frac{\Gamma_{\text{tot}}(H_{\text{SM}})}{\Gamma_{\text{tot}}(H)} \frac{|S^\gamma|^2}{|S_{\text{SM}}^\gamma|^2} \simeq 4 \frac{|1.27 C_V - 0.27 C_f^S|^2}{C_V^2 + 3(C_f^S)^2} \quad (\text{C.1})$$

where we use Eq. (17), Eq. (11) together with $\Delta S^\gamma = 0$ and $S_{\text{SM}}^\gamma = -6.542 + 0.046i$, and

$$\begin{aligned} \frac{\Gamma_{\text{tot}}(H)}{\Gamma_{\text{tot}}(H_{\text{SM}})} &\simeq [\Gamma(H \rightarrow bb) + \Gamma(H \rightarrow WW^*) + \Gamma(H \rightarrow gg) + \Gamma(H \rightarrow \tau\tau) + \Gamma(H \rightarrow cc) + \Gamma(H \rightarrow ZZ^*)] / \Gamma_{\text{tot}}(H_{\text{SM}}) \\ &= C_V^2 [B(H \rightarrow WW^*) + B(H \rightarrow ZZ^*)]_{\text{SM}} + (C_f^S)^2 [B(H \rightarrow bb) + B(H \rightarrow gg) + B(H \rightarrow \tau\tau) + B(H \rightarrow cc)]_{\text{SM}} \\ &\simeq [C_V^2 + 3(C_f^S)^2] / 4. \end{aligned}$$

Introducing $C_V \equiv 1 + \delta_V$ and $C_f^S \equiv 1 + \delta_f^S$, we have

$$\widehat{\mu}(\gamma\gamma) \simeq 1 + 2(\delta_V - \delta_f^S). \quad (\text{C.2})$$

Incorporating the six production processes of ggF, VBF, WH, ZH, ttH, and tH with

$$\widehat{\mu}(\text{ggF} + \text{bbH}) = \widehat{\mu}(\text{ttH}) = (C_f^S)^2; \quad \widehat{\mu}(\text{VBF}) = \widehat{\mu}(\text{WH}) = \widehat{\mu}(\text{ZH}) = C_V^2; \quad \widehat{\mu}(\text{tH}) = 3(C_f^S)^2 + 3.4C_V^2 - 5.4C_f^S C_V, \quad (\text{C.3})$$

we find that the global behavior of the theoretical $pp \rightarrow H \rightarrow \gamma\gamma$ signal strength around the SM point could be described by the following relation:

$$\mu(\sum \mathcal{P}, \gamma\gamma) \sim 1 + 3\delta_V - \delta_f^S \simeq 1.1 \pm 0.07, \quad (\text{C.4})$$

where we use $\mu(\sum \mathcal{P}, \gamma\gamma) = 1.10 \pm 0.07$, see Table VI. Note that the above relation is equivalent to $C_f^S \sim 3C_V - 2.1$ for the central value of 1.1 which is quoted below Eq. (41).

Appendix D: Correlations in CPC2, CPC3, and CPC4

In Table XXII, we present correlations among the fitting parameters in **CPC2**, **CPC3**, and **CPC4** obtained by fitting the CL contours in the x - y plane to the ellipses given by

$$\frac{(x - \widehat{x})^2}{\sigma_x^2} + \frac{(y - \widehat{y})^2}{\sigma_y^2} - 2\rho_{xy} \frac{(x - \widehat{x})(y - \widehat{y})}{\sigma_x \sigma_y} = R^2(1 - \rho_{xy}^2) \quad (\text{D.1})$$

with $R^2 = \Delta\chi^2 = 1$ (1 σ), 2.3 (68.27% CL), 5.99 (95% CL), and 11.83 (99.73% CL). Note that we consider the CL regions around the best-fit point of $(x, y) = (\widehat{x}, \widehat{y})$ and drop the HP scenarios in which the CL contours are not closed. The best-fitted values of \widehat{x} and \widehat{y} and the 1 σ errors of $\sigma_{x,y}$ are taken from Table XII and Table XIII and, when the upper and lower 1 σ errors are different from each other, we take the average of them. In Table XXII, the dependence of ρ on $\Delta\chi^2$ could be considered as deviations from Gaussianity and the correlations are to be understood as approximations especially when the values of ρ are fluctuating noticeably. For the fits with the higher number of fitting parameters with $n \geq 5$ and the more precise and detailed information even when $n \leq 4$, the grids for the boundaries of various CL regions are available upon request to the authors.

Appendix E: Fits including $H \rightarrow Z\gamma$ data with $\widehat{\mu}(Z\gamma) = 2.2 \pm 0.7$: CPC2-HC and CPC6-AHC

In this Appendix, we perform global fits of the Higgs boson couplings to the extended Higgs datasets by including the Higgs boson decay to a Z boson and a photon [14] which has been recently reported after the appearance of Refs. [3, 4]. Therefore, including the 76 experimental signal strengths shown in Tables I, II, III, and IV, we consider 77 signal strengths in total in this Appendix. More precisely, since the combined analysis in Ref. [14] is based on the measured branching ratio of $B(H \rightarrow Z\gamma) = (3.4 \pm 1.1) \times 10^{-3}$ assuming the SM Higgs boson production cross sections, we consider the following 77th experimental signal strength

$$\mu^{\text{EXP}}(\mathcal{Q}, Z\gamma) \simeq \widehat{\mu}(\mathcal{Q}) \widehat{\mu}(Z\gamma) = \sum_{\mathcal{P}_i \subset \mathcal{Q}} \widehat{\mu}(\mathcal{P}_i) \widehat{\mu}(Z\gamma) = \widehat{\mu}(Z\gamma) = 2.2 \pm 0.7. \quad (\text{E.1})$$

For the SM, we obtain $\chi_{\text{SM}}^2/\text{dof} = 85.2868/77$ and $\text{gof} = 0.2424$. Note that, compared to the case without including the $H \rightarrow Z\gamma$ data, χ_{SM}^2 increases by the amount of $(1 - 2.2)^2/0.7^2 = 2.9388$ while gof decreases by 0.0471.

²⁸ We recall that, without including the $H \rightarrow Z\gamma$ data, $\chi_{\text{SM}}^2/\text{dof} = 82.3480/76$ and $\text{gof} = 0.2895$.

TABLE XXII. Correlations $\rho_{xy} = \rho(x, y)$ between the two fitting parameters of x and y in **CPC2**, **CPC3**, and **CPC4**.

Fit	$\rho(x, y)$	1σ	68.27% CL	95% CL	99.73% CL
CPC2-IUHC	$\rho(\Delta S^\gamma, \Delta\Gamma_{\text{tot}})$	-0.493	-0.495	-0.503	-0.485
CPC2-HCC	$\rho(\Delta S^g, \Delta S^\gamma)$	0.424	0.420	0.428	0.414
CPC2-CSB	$\rho(C_W, C_Z)$	0.113	0.092	0.091	0.092
CPC2-I	$\rho(C_V, C_f^S)$	0.386	0.383	0.380	0.379
CPC2-II	$\rho(C_u^S, C_{d\ell}^S)$	0.632	0.630	0.630	0.630
CPC2-III	$\rho(C_{ud}^S, C_\ell^S)$	0.228	0.225	0.202	0.202
CPC2-IV	$\rho(C_{u\ell}^S, C_d^S)$	0.710	0.710	0.715	0.706
CPC3-IUHCC	$\rho(\Delta S^g, \Delta S^\gamma)$	0.122	0.123	0.114	0.116
	$\rho(\Delta S^g, \Delta\Gamma_{\text{tot}})$	0.641	0.638	0.639	0.665
	$\rho(\Delta S^\gamma, \Delta\Gamma_{\text{tot}})$	-0.309	-0.295	-0.303	-0.291
CPC3-II	$\rho(C_V, C_u^S)$	0.101	0.108	0.104	0.099
	$\rho(C_V, C_{d\ell}^S)$	0.742	0.741	0.740	0.737
	$\rho(C_u^S, C_{d\ell}^S)$	0.494	0.492	0.488	0.484
CPC3-III	$\rho(C_V, C_{ud}^S)$	0.404	0.389	0.397	0.391
	$\rho(C_V, C_\ell^S)$	0.211	0.212	0.210	0.210
	$\rho(C_{ud}^S, C_\ell^S)$	0.288	0.282	0.278	0.279
CPC3-IV	$\rho(C_V, C_{u\ell}^S)$	0.659	0.653	0.650	0.652
	$\rho(C_V, C_d^S)$	0.884	0.883	0.879	0.878
	$\rho(C_{u\ell}^S, C_d^S)$	0.830	0.826	0.827	0.825
CPC4-A	$\rho(C_V, C_u^S)$	0.515	0.508	0.481	0.499
	$\rho(C_V, C_d^S)$	0.884	0.873	0.861	0.855
	$\rho(C_{u\ell}^S, C_d^S)$	0.779	0.755	0.741	0.729
	$\rho(C_V, C_\ell^S)$	0.647	0.616	0.604	0.595
	$\rho(C_u^S, C_\ell^S)$	0.504	0.447	0.417	0.410
	$\rho(C_d^S, C_\ell^S)$	0.679	0.647	0.622	0.595

Since one might need nonvanishing $\Delta S^{Z\gamma}$ to resolve the tension in the measured $H \rightarrow Z\gamma$ signal strength as discussed in subsection IV C, we consider HC scenarios in which there exist heavy electrically charged non-SM particles leading to nonvanishing ΔS^γ and $\Delta S^{Z\gamma}$ simultaneously. To be specific, we consider the following two CPC fits:

- **CPC2-HC**: vary $\{\Delta S^\gamma, \Delta S^{Z\gamma}\}$ with the gauge-Higgs and Yukawa couplings the same as in the SM
- **CPC6-AHC**: vary $\{\Delta S^\gamma, \Delta S^{Z\gamma}, C_V, C_u^S, C_d^S, C_\ell^S\}$ with the gauge-Higgs and Yukawa couplings like as in A2HDM

Note that we have promoted **CPC1-HC** and **CPC5-AHC** by employing $\Delta S^{Z\gamma}$ as an additional varying parameter.

In **CPC2-HC**, we obtain the following best-fitted values and 1σ errors:²⁹

$$\Delta S^\gamma = -0.318_{-0.176}^{+0.176}; \quad \Delta S^{Z\gamma} = -5.698_{-2.571}^{+3.013}, +29.038_{-3.015}^{+2.568}, \quad (\text{E.2})$$

with $\chi_{\text{min}}^2/\text{dof} = 79.1649/75$, $\text{gof} = 0.3489$, and p -value against the SM = 0.0468. We observe that ΔS^γ is fitted similarly as in **CPC1-HC**, see Table XI, and there are two degenerate minima for the negative (< 0) and positive (> 0) values of

²⁹ We have obtained the same best-fitted value for ΔS^γ at the both degenerate minima for the positive and negative values of $\Delta S^{Z\gamma}$.

TABLE XXIII. **CPC6-AHC**: The best-fitted values at the four degenerate minima in **CPC6-AHC**. We have $\chi_{\min}^2/\text{dof} = 73.9864/71$, $\text{gof} = 0.3810$, and p -value against the SM = 0.0795. For the SM, in contrast, we obtain $\chi_{\text{SM}}^2/\text{dof} = 85.2868/77$ and $\text{gof} = 0.2424$.

Fitting parameter	Best-fitted values			
C_ℓ^S	$+0.921^{+0.047}_{-0.046}$	$+0.921^{+0.044}_{-0.045}$	$-0.921^{+0.044}_{-0.045}$	$-0.921^{+0.045}_{-0.046}$
$\Delta S^{Z\gamma}$	$-5.548^{+2.768}_{-2.367}$	$+28.956^{+2.742}_{-2.840}$	$-5.548^{+2.745}_{-2.429}$	$+28.956^{+2.679}_{-2.828}$
ΔS^γ	$-0.102^{+0.205}_{-0.211}$	$-0.102^{+0.217}_{-0.208}$	$-0.146^{+0.207}_{-0.203}$	$-0.146^{+0.204}_{-0.200}$
C_V	$0.999^{+0.033}_{-0.033}$	$0.999^{+0.035}_{-0.033}$	$0.999^{+0.032}_{-0.033}$	$0.999^{+0.034}_{-0.035}$
C_u^S	$0.930^{+0.039}_{-0.040}$	$0.930^{+0.041}_{-0.039}$	$0.930^{+0.039}_{-0.039}$	$0.930^{+0.040}_{-0.037}$
C_d^S	$0.908^{+0.078}_{-0.077}$	$0.908^{+0.082}_{-0.077}$	$0.908^{+0.078}_{-0.074}$	$0.908^{+0.078}_{-0.080}$

$\Delta S^{Z\gamma}$ as dictated by the relation $\left|S_{\text{SM}}^{Z\gamma} + \Delta S^{Z\gamma}\right|_{<0}^2 = \left|S_{\text{SM}}^{Z\gamma} + \Delta S^{Z\gamma}\right|_{>0}^2$ with $S_{\text{SM}}^{Z\gamma} = -11.6701 + 0.0114i$, see Eq. (54). Note that ΔS^γ shows a 1.8σ deviation from the SM while $\Delta S^{Z\gamma}|_{<0}$ deviates from the SM by 1.9σ .

In **CPC6-AHC**, there are four degenerate minima depending on the signs of C_ℓ^S and $\Delta S^{Z\gamma}$. See Table XXIII for the best-fitted values of the six fitting parameters at each minimum. We note that the best-fitted values of C_V and $C_{u,d}^S$ at the four degenerate minima are almost the same like as in **CPC5-AHC**. For the statistical measures, we have $\text{gof} = 0.3810$ and p -value against the SM = 0.0795 with $\chi_{\min}^2/\text{dof} = 73.9864/71$. Note that ΔS^γ is consistent with the SM while $\Delta S^{Z\gamma}|_{<0}$ deviates from the SM by 2.0σ . In Fig. 14, the CL regions of **CPC2-HC** (left) and **CPC6-AHC** (right) are shown in the $(\Delta S^{Z\gamma}, \Delta S^\gamma)$ plane. We observe that the SM points locate outside the 68% CL regions.

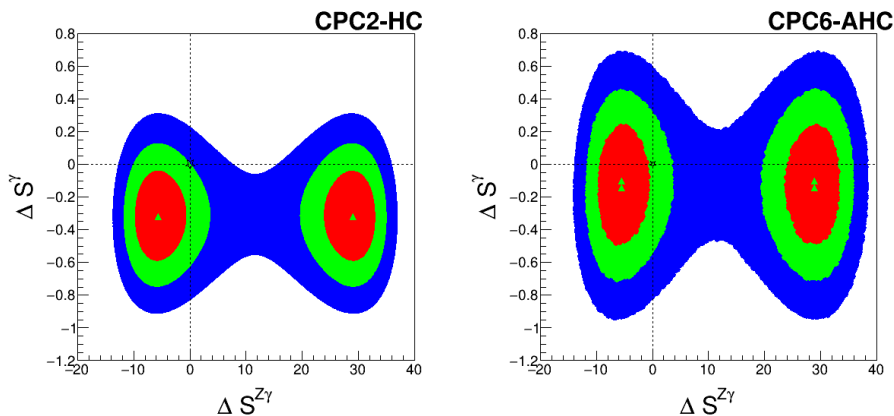


FIG. 14. The CL regions of **CPC2-HC** (left) and **CPC6-AHC** (right) in the $(\Delta S^{Z\gamma}, \Delta S^\gamma)$ plane. The contour regions shown are for $\Delta\chi^2 \leq 2.3$ (red), $\Delta\chi^2 \leq 5.99$ (green), $\Delta\chi^2 \leq 11.83$ (blue) above the minimum, which correspond to confidence levels of 68.27%, 95%, and 99.73%, respectively. In each frame, the vertical and horizontal lines locate the SM point denoted by a star and the best-fit points are denoted by triangles.

-
- [1] G. Aad *et al.* [ATLAS], “Observation of a new particle in the search for the Standard Model Higgs boson with the ATLAS detector at the LHC,” *Phys. Lett. B* **716**, 1-29 (2012) doi:10.1016/j.physletb.2012.08.020 [arXiv:1207.7214 [hep-ex]].
 - [2] S. Chatrchyan *et al.* [CMS], “Observation of a New Boson at a Mass of 125 GeV with the CMS Experiment at the LHC,” *Phys. Lett. B* **716**, 30-61 (2012) doi:10.1016/j.physletb.2012.08.021 [arXiv:1207.7235 [hep-ex]].
 - [3] [ATLAS], “A detailed map of Higgs boson interactions by the ATLAS experiment ten years after the discovery,” *Nature* **607** (2022) no.7917, 52-59 [erratum: *Nature* **612** (2022) no.7941, E24] doi:10.1038/s41586-022-04893-w [arXiv:2207.00092 [hep-ex]].
 - [4] A. Tumasyan *et al.* [CMS], “A portrait of the Higgs boson by the CMS experiment ten years after the discovery,” *Nature* **607** (2022) no.7917, 60-68 doi:10.1038/s41586-022-04892-x [arXiv:2207.00043 [hep-ex]].
 - [5] G. Aad *et al.* [ATLAS], “Combined measurement of the Higgs boson mass from the $H \rightarrow \gamma\gamma$ and $H \rightarrow ZZ^* \rightarrow 4\ell$ decay channels with the ATLAS detector using $\sqrt{s} = 7, 8$ and 13 TeV pp collision data,” [arXiv:2308.04775 [hep-ex]].
 - [6] See, for example, K. Cheung, J. S. Lee and P. Y. Tseng, “Higgs Precision (Higgcision) Era begins,” *JHEP* **05**, 134 (2013) doi:10.1007/JHEP05(2013)134 [arXiv:1302.3794 [hep-ph]].

- [7] See, for example, K. Cheung, J. S. Lee and P. Y. Tseng, “Higgs precision analysis updates 2014,” *Phys. Rev. D* **90**, 095009 (2014) doi:10.1103/PhysRevD.90.095009 [arXiv:1407.8236 [hep-ph]].
- [8] M. Aaboud *et al.* [ATLAS], “Evidence for the $H \rightarrow b\bar{b}$ decay with the ATLAS detector,” *JHEP* **12**, 024 (2017) doi:10.1007/JHEP12(2017)024 [arXiv:1708.03299 [hep-ex]].
- [9] A. M. Sirunyan *et al.* [CMS], “Observation of Higgs boson decay to bottom quarks,” *Phys. Rev. Lett.* **121**, no.12, 121801 (2018) doi:10.1103/PhysRevLett.121.121801 [arXiv:1808.08242 [hep-ex]].
- [10] [ATLAS], “Cross-section measurements of the Higgs boson decaying to a pair of tau leptons in proton–proton collisions at $\sqrt{s} = 13$ TeV with the ATLAS detector,” ATLAS-CONF-2018-021.
- [11] A. M. Sirunyan *et al.* [CMS], “Observation of the Higgs boson decay to a pair of τ leptons with the CMS detector,” *Phys. Lett. B* **779**, 283-316 (2018) doi:10.1016/j.physletb.2018.02.004 [arXiv:1708.00373 [hep-ex]].
- [12] K. Cheung, J. S. Lee and P. Y. Tseng, “New Emerging Results in Higgs Precision Analysis Updates 2018 after Establishment of Third-Generation Yukawa Couplings,” *JHEP* **09**, 098 (2019) doi:10.1007/JHEP09(2019)098 [arXiv:1810.02521 [hep-ph]].
- [13] G. Aad *et al.* [ATLAS and CMS], “Measurements of the Higgs boson production and decay rates and constraints on its couplings from a combined ATLAS and CMS analysis of the LHC pp collision data at $\sqrt{s} = 7$ and 8 TeV,” *JHEP* **08**, 045 (2016) doi:10.1007/JHEP08(2016)045 [arXiv:1606.02266 [hep-ex]].
- [14] G. Aad *et al.* [ATLAS and CMS], “Evidence for the Higgs Boson Decay to a Z Boson and a Photon at the LHC,” *Phys. Rev. Lett.* **132**, 021803 (2024) doi:10.1103/PhysRevLett.132.021803 [arXiv:2309.03501 [hep-ex]].
- [15] A. Juste, in Proceedings of HCP2012, 15 November 2012, Kyoto, Japan, <http://kds.kek.jp/conferenceDisplay.py?confId=9237>.
- [16] K. Herner [CDF and D0], “Higgs Boson Studies at the Tevatron,” *Nucl. Part. Phys. Proc.* **273-275**, 852-856 (2016) doi:10.1016/j.nuclphysbps.2015.09.131
- [17] G. Aad *et al.* [ATLAS], “Higgs boson production cross-section measurements and their EFT interpretation in the 4ℓ decay channel at $\sqrt{s} = 13$ TeV with the ATLAS detector,” *Eur. Phys. J. C* **80**, no.10, 957 (2020) [erratum: *Eur. Phys. J. C* **81**, no.1, 29 (2021); erratum: *Eur. Phys. J. C* **81**, no.5, 398 (2021)] doi:10.1140/epjc/s10052-020-8227-9 [arXiv:2004.03447 [hep-ex]].
- [18] [ATLAS], “Measurements of Higgs boson production by gluon–gluon fusion and vector-boson fusion using $H \rightarrow WW^* \rightarrow e\nu\mu\nu$ decays in pp collisions at $\sqrt{s} = 13$ TeV with the ATLAS detector,” [arXiv:2207.00338 [hep-ex]].
- [19] G. Aad *et al.* [ATLAS], “Measurement of the production cross section for a Higgs boson in association with a vector boson in the $H \rightarrow WW^* \rightarrow \ell\nu\ell\nu$ channel in pp collisions at $\sqrt{s} = 13$ TeV with the ATLAS detector,” *Phys. Lett. B* **798**, 134949 (2019) doi:10.1016/j.physletb.2019.134949 [arXiv:1903.10052 [hep-ex]].
- [20] G. Aad *et al.* [ATLAS], “Measurement of the properties of Higgs boson production at $\sqrt{s} = 13$ TeV in the $H \rightarrow \gamma\gamma$ channel using 139 fb^{-1} of pp collision data with the ATLAS experiment,” *JHEP* **07**, 088 (2023) doi:10.1007/JHEP07(2023)088 [arXiv:2207.00348 [hep-ex]].
- [21] G. Aad *et al.* [ATLAS], “A search for the $Z\gamma$ decay mode of the Higgs boson in pp collisions at $\sqrt{s} = 13$ TeV with the ATLAS detector,” *Phys. Lett. B* **809**, 135754 (2020) doi:10.1016/j.physletb.2020.135754 [arXiv:2005.05382 [hep-ex]].
- [22] G. Aad *et al.* [ATLAS], “Measurements of WH and ZH production in the $H \rightarrow b\bar{b}$ decay channel in pp collisions at 13 TeV with the ATLAS detector,” *Eur. Phys. J. C* **81**, no.2, 178 (2021) doi:10.1140/epjc/s10052-020-08677-2 [arXiv:2007.02873 [hep-ex]].
- [23] G. Aad *et al.* [ATLAS], “Measurement of the associated production of a Higgs boson decaying into b -quarks with a vector boson at high transverse momentum in pp collisions at $\sqrt{s} = 13$ TeV with the ATLAS detector,” *Phys. Lett. B* **816**, 136204 (2021) doi:10.1016/j.physletb.2021.136204 [arXiv:2008.02508 [hep-ex]].
- [24] G. Aad *et al.* [ATLAS], “Measurements of Higgs bosons decaying to bottom quarks from vector boson fusion production with the ATLAS experiment at $\sqrt{s} = 13$ TeV,” *Eur. Phys. J. C* **81**, no.6, 537 (2021) doi:10.1140/epjc/s10052-021-09192-8 [arXiv:2011.08280 [hep-ex]].
- [25] G. Aad *et al.* [ATLAS], “Measurement of Higgs boson decay into b -quarks in associated production with a top-quark pair in pp collisions at $\sqrt{s} = 13$ TeV with the ATLAS detector,” *JHEP* **06**, 097 (2022) doi:10.1007/JHEP06(2022)097 [arXiv:2111.06712 [hep-ex]].
- [26] G. Aad *et al.* [ATLAS], “Constraints on Higgs boson production with large transverse momentum using $H \rightarrow b\bar{b}$ decays in the ATLAS detector,” *Phys. Rev. D* **105**, no.9, 092003 (2022) doi:10.1103/PhysRevD.105.092003 [arXiv:2111.08340 [hep-ex]].
- [27] G. Aad *et al.* [ATLAS], “Measurements of Higgs boson production cross-sections in the $H \rightarrow \tau^+\tau^-$ decay channel in pp collisions at $\sqrt{s} = 13$ TeV with the ATLAS detector,” *JHEP* **08**, 175 (2022) doi:10.1007/JHEP08(2022)175 [arXiv:2201.08269 [hep-ex]].
- [28] M. Aaboud *et al.* [ATLAS], “Evidence for the associated production of the Higgs boson and a top quark pair with the ATLAS detector,” *Phys. Rev. D* **97**, no.7, 072003 (2018) doi:10.1103/PhysRevD.97.072003 [arXiv:1712.08891 [hep-ex]].
- [29] G. Aad *et al.* [ATLAS], “A search for the dimuon decay of the Standard Model Higgs boson with the ATLAS detector,” *Phys. Lett. B* **812**, 135980 (2021) doi:10.1016/j.physletb.2020.135980 [arXiv:2007.07830 [hep-ex]].
- [30] G. Aad *et al.* [ATLAS], “Direct constraint on the Higgs-charm coupling from a search for Higgs boson decays into charm quarks with the ATLAS detector,” *Eur. Phys. J. C* **82**, 717 (2022) doi:10.1140/epjc/s10052-022-10588-3 [arXiv:2201.11428 [hep-ex]].
- [31] G. Aad *et al.* [ATLAS], “Search for invisible Higgs-boson decays in events with vector-boson fusion signatures using 139 fb^{-1} of proton-proton data recorded by the ATLAS experiment,” *JHEP* **08**, 104 (2022) doi:10.1007/JHEP08(2022)104 [arXiv:2202.07953 [hep-ex]].
- [32] G. Aad *et al.* [ATLAS], “Search for associated production of a Z boson with an invisibly decaying Higgs boson or dark matter candidates at $s=13$ TeV with the ATLAS detector,” *Phys. Lett. B* **829**, 137066 (2022) doi:10.1016/j.physletb.2022.137066 [arXiv:2111.08372 [hep-ex]].
- [33] A. M. Sirunyan *et al.* [CMS], “Measurements of Higgs boson production cross sections and couplings in the diphoton decay channel at $\sqrt{s} = 13$ TeV,” *JHEP* **07**, 027 (2021) doi:10.1007/JHEP07(2021)027 [arXiv:2103.06956 [hep-ex]].
- [34] A. M. Sirunyan *et al.* [CMS], “Measurements of production cross sections of the Higgs boson in the four-lepton final state in proton–proton collisions at $\sqrt{s} = 13$ TeV,” *Eur. Phys. J. C* **81**, no.6, 488 (2021) doi:10.1140/epjc/s10052-021-09200-x [arXiv:2103.04956 [hep-ex]].

- [35] A. Tumasyan *et al.* [CMS], “Measurements of the Higgs boson production cross section and couplings in the W boson pair decay channel in proton-proton collisions at $\sqrt{s} = 13$ TeV,” *Eur. Phys. J. C* **83**, no.7, 667 (2023) doi:10.1140/epjc/s10052-023-11632-6 [arXiv:2206.09466 [hep-ex]].
- [36] A. Tumasyan *et al.* [CMS], “Search for Higgs boson decays to a Z boson and a photon in proton-proton collisions at $\sqrt{s} = 13$ TeV,” *JHEP* **05**, 233 (2023) doi:10.1007/JHEP05(2023)233 [arXiv:2204.12945 [hep-ex]].
- [37] A. Tumasyan *et al.* [CMS], “Measurements of Higgs boson production in the decay channel with a pair of τ leptons in proton-proton collisions at $\sqrt{s} = 13$ TeV,” *Eur. Phys. J. C* **83**, no.7, 562 (2023) doi:10.1140/epjc/s10052-023-11452-8 [arXiv:2204.12957 [hep-ex]].
- [38] A. M. Sirunyan *et al.* [CMS], “Evidence for the Higgs boson decay to a bottom quark-antiquark pair,” *Phys. Lett. B* **780**, 501-532 (2018) doi:10.1016/j.physletb.2018.02.050 [arXiv:1709.07497 [hep-ex]].
- [39] A. M. Sirunyan *et al.* [CMS], “Search for $t\bar{t}H$ production in the all-jet final state in proton-proton collisions at $\sqrt{s} = 13$ TeV,” *JHEP* **06**, 101 (2018) doi:10.1007/JHEP06(2018)101 [arXiv:1803.06986 [hep-ex]].
- [40] A. M. Sirunyan *et al.* [CMS], “Search for $t\bar{t}H$ production in the $H \rightarrow b\bar{b}$ decay channel with leptonic $t\bar{t}$ decays in proton-proton collisions at $\sqrt{s} = 13$ TeV,” *JHEP* **03**, 026 (2019) doi:10.1007/JHEP03(2019)026 [arXiv:1804.03682 [hep-ex]].
- [41] A. M. Sirunyan *et al.* [CMS], “Inclusive search for highly boosted Higgs bosons decaying to bottom quark-antiquark pairs in proton-proton collisions at $\sqrt{s} = 13$ TeV,” *JHEP* **12**, 085 (2020) doi:10.1007/JHEP12(2020)085 [arXiv:2006.13251 [hep-ex]].
- [42] A. M. Sirunyan *et al.* [CMS], “Evidence for Higgs boson decay to a pair of muons,” *JHEP* **01**, 148 (2021) doi:10.1007/JHEP01(2021)148 [arXiv:2009.04363 [hep-ex]].
- [43] A. M. Sirunyan *et al.* [CMS], “Measurement of the Higgs boson production rate in association with top quarks in final states with electrons, muons, and hadronically decaying tau leptons at $\sqrt{s} = 13$ TeV,” *Eur. Phys. J. C* **81**, no.4, 378 (2021) doi:10.1140/epjc/s10052-021-09014-x [arXiv:2011.03652 [hep-ex]].
- [44] A. Tumasyan *et al.* [CMS], “Search for invisible decays of the Higgs boson produced via vector boson fusion in proton-proton collisions at $s=13$ TeV,” *Phys. Rev. D* **105**, no.9, 092007 (2022) doi:10.1103/PhysRevD.105.092007 [arXiv:2201.11585 [hep-ex]].
- [45] A. Tumasyan *et al.* [CMS], “Search for new particles in events with energetic jets and large missing transverse momentum in proton-proton collisions at $\sqrt{s} = 13$ TeV,” *JHEP* **11**, 153 (2021) doi:10.1007/JHEP11(2021)153 [arXiv:2107.13021 [hep-ex]].
- [46] A. M. Sirunyan *et al.* [CMS], “Search for dark matter produced in association with a leptonically decaying Z boson in proton-proton collisions at $\sqrt{s} = 13$ TeV,” *Eur. Phys. J. C* **81**, no.1, 13 (2021) [erratum: *Eur. Phys. J. C* **81**, no.4, 333 (2021)] doi:10.1140/epjc/s10052-020-08739-5 [arXiv:2008.04735 [hep-ex]].
- [47] S. Y. Choi, J. S. Lee and J. Park, “Decays of Higgs bosons in the Standard Model and beyond,” *Prog. Part. Nucl. Phys.* **120** (2021), 103880 doi:10.1016/j.pnpnp.2021.103880 [arXiv:2101.12435 [hep-ph]].
- [48] J. Alwall, R. Frederix, S. Frixione, V. Hirschi, F. Maltoni, O. Mattelaer, H. S. Shao, T. Stelzer, P. Torrielli and M. Zaro, “The automated computation of tree-level and next-to-leading order differential cross sections, and their matching to parton shower simulations,” *JHEP* **07**, 079 (2014) doi:10.1007/JHEP07(2014)079 [arXiv:1405.0301 [hep-ph]].
- [49] R. D. Ball, V. Bertone, S. Carrazza, C. S. Deans, L. Del Debbio, S. Forte, A. Guffanti, N. P. Hartland, J. I. Latorre and J. Rojo, *et al.* “Parton distributions with LHC data,” *Nucl. Phys. B* **867**, 244-289 (2013) doi:10.1016/j.nuclphysb.2012.10.003 [arXiv:1207.1303 [hep-ph]].
- [50] R. Harlander, M. Mühlleitner, J. Rathsmann, M. Spira and O. Stål, “Interim recommendations for the evaluation of Higgs production cross sections and branching ratios at the LHC in the Two-Higgs-Doublet Model,” [arXiv:1312.5571 [hep-ph]].
- [51] J. Bernon and B. Dumont, “Lilith: a tool for constraining new physics from Higgs measurements,” *Eur. Phys. J. C* **75**, no.9, 440 (2015) doi:10.1140/epjc/s10052-015-3645-9 [arXiv:1502.04138 [hep-ph]].
- [52] S. Kraml, T. Q. Loc, D. T. Nhung and L. Ninh, “Constraining new physics from Higgs measurements with Lilith: update to LHC Run 2 results,” *SciPost Phys.* **7**, no.4, 052 (2019) doi:10.21468/SciPostPhys.7.4.052 [arXiv:1908.03952 [hep-ph]].
- [53] R. V. Harlander, S. Liebler and H. Mantler, “SusHi: A program for the calculation of Higgs production in gluon fusion and bottom-quark annihilation in the Standard Model and the MSSM,” *Comput. Phys. Commun.* **184** (2013), 1605-1617 doi:10.1016/j.cpc.2013.02.006 [arXiv:1212.3249 [hep-ph]].
- [54] R. V. Harlander, S. Liebler and H. Mantler, “SusHi Bento: Beyond NNLO and the heavy-top limit,” *Comput. Phys. Commun.* **212** (2017), 239-257 doi:10.1016/j.cpc.2016.10.015 [arXiv:1605.03190 [hep-ph]].
- [55] D. de Florian *et al.* [LHC Higgs Cross Section Working Group], “Handbook of LHC Higgs Cross Sections: 4. Deciphering the Nature of the Higgs Sector,” doi:10.23731/CYRM-2017-002 [arXiv:1610.07922 [hep-ph]].
- [56] F. Demartin, B. Maier, F. Maltoni, K. Mawatari and M. Zaro, “ tWH associated production at the LHC,” *Eur. Phys. J. C* **77**, no.1, 34 (2017) doi:10.1140/epjc/s10052-017-4601-7 [arXiv:1607.05862 [hep-ph]].
- [57] R. L. Workman *et al.* [Particle Data Group], “Review of Particle Physics,” *PTEP* **2022** (2022), 083C01 doi:10.1093/ptep/ptac097
- [58] S. L. Glashow and S. Weinberg, “Natural Conservation Laws for Neutral Currents,” *Phys. Rev. D* **15** (1977) 1958.
- [59] J. S. Lee and J. Park, “Yukawa alignment revisited in the Higgs basis,” *Phys. Rev. D* **106** (2022) no.1, 015023 doi:10.1103/PhysRevD.106.015023 [arXiv:2110.03908 [hep-ph]].
- [60] K. Cheung, P. Ko, J. S. Lee and P. Y. Tseng, “Bounds on Higgs-Portal models from the LHC Higgs data,” *JHEP* **10**, 057 (2015) doi:10.1007/JHEP10(2015)057 [arXiv:1507.06158 [hep-ph]].
- [61] A. Pich and P. Tuzon, “Yukawa Alignment in the Two-Higgs-Doublet Model,” *Phys. Rev. D* **80** (2009), 091702 doi:10.1103/PhysRevD.80.091702 [arXiv:0908.1554 [hep-ph]].
- [62] A. Tumasyan *et al.* [CMS], “Search for Higgs Boson Decay to a Charm Quark-Antiquark Pair in Proton-Proton Collisions at $s=13$ TeV,” *Phys. Rev. Lett.* **131**, no.6, 061801 (2023) doi:10.1103/PhysRevLett.131.061801 [arXiv:2205.05550 [hep-ex]].
- [63] T. Biekötter and M. Pierre, “Higgs-boson visible and invisible constraints on hidden sectors,” *Eur. Phys. J. C* **82**, no.11, 1026 (2022) doi:10.1140/epjc/s10052-022-10990-x [arXiv:2208.05505 [hep-ph]].
- [64] [ATLAS], “Combination of searches for invisible decays of the Higgs boson using 139 fb $^{-1}$ of proton-proton collision data at $s=13$ TeV collected with the ATLAS experiment,” *Phys. Lett. B* **842**, 137963 (2023) doi:10.1016/j.physletb.2023.137963

- [arXiv:2301.10731 [hep-ex]].
- [65] A. Tumasyan *et al.* [CMS], “A search for decays of the Higgs boson to invisible particles in events with a top-antitop quark pair or a vector boson in proton-proton collisions at $\sqrt{s} = 13$ TeV,” *Eur. Phys. J. C* **83**, no.10, 933 (2023) doi:10.1140/epjc/s10052-023-11952-7 [arXiv:2303.01214 [hep-ex]].
- [66] J. Butterworth, S. Carrazza, A. Cooper-Sarkar, A. De Roeck, J. Feltesse, S. Forte, J. Gao, S. Glazov, J. Huston and Z. Kassabov, *et al.* “PDF4LHC recommendations for LHC Run II,” *J. Phys. G* **43**, 023001 (2016) doi:10.1088/0954-3899/43/2/023001 [arXiv:1510.03865 [hep-ph]].